An Assessment of the Quasi-Biennial Oscillation (QBO) and Sudden Stratospheric Warmings (SSWs) with Idealized General Circulation Models

by

Weiye Yao

A dissertation submitted in partial fulfillment
of the requirements for the degree of
Doctor of Philosophy
(Atmospheric, Oceanic and Space Sciences and Scientific Computing)
in The University of Michigan
2015

Doctoral Committee:

Professor Christiane Jablonowski, Chair
Professor August Evrard
Jadwiga H. Richter, National Center for Atmospheric Research
Professor Richard B. Rood

To Mom and Dad

ACKNOWLEDGEMENTS

The completion of this dissertation is a result of a collaborative effort and the support of many people. First and foremost, many thanks to my thesis advisor and chair of my committee, Prof. Christiane Jablonowski. Christiane has led me into the scientific world and provided great guidance for my research and future career. She sets a great example for me as a scientist and her dedication in research will influence me for the rest of my life. Her patience for me and my work had been a great support along these years. I also would like to thank all other members go my of my committee, Jadwiga Richter, Richard Rood and August Evrard. I appreciate all of your advice and support.

In addition, many thanks to Jadwiga Richter, Julio Bacmeister and Peter Lauritzen who were my research advisors during my 3-month visit of the National Center for Atmospheric Research (NCAR) as part of my graduate fellowship from NCAR's Advanced Study Program. Jadwiga Richter, Julio Bacmeister and Peter Lauritzen have provided great research and career advises. I look forward to the many years of collaboration to come. Many thanks to Yi Deng at Georgia Institute of Technology for career advice. I thank Sean Santos at NCAR for his help with model setups and the debugging of the Community Earth System Model.

Thank you to my previous and current officemates, Paul Ulrich, Kevin Reed, Colin Zarzycki, Diana Thatcher, Jared Ferguson for your help with both English and research. You are my first friends in this country and I am truly thankful for all your help during my five years of stay. Life would have been much tougher without your

help. In addition, many thanks to James Kent who also helps me with my research. Many thanks to Diana Thatcher for her work in developing the moist Held Suarez package, I expect to see her work published soon.

Thank you to Ahmed Tawfik, Susan Cheng, Gina DiBraccio, Kristen Mihalka, Dan Gershman, Shannon Curry, Yuni Lee and many others from AOSS for your love and support. Special thanks to my AOSS Chinese friends, especially Chunpeng Wang and Meng Jin who entered their PhD programs at the same year as me. The memory of us working on homeworks, projects, preparing for qualifying exams and countless lunch-time discussions will always be with me through my life. I am really lucky to know you in Michigan. I thank my previous and current roommates Xing Meng and Youyang Hou, your friendship and companionship will always be in my mind. A special thank you to my best friend from high school, Yunru Han who is also a PhD student in Columbia University, and thanks to many other high school friends who went to Peking University and came to the states together with me, Ziyin Lin, Sinan Zhao, etc. I really appreciate the moral support from you for over a decade and many decades to come. I will always remember the night-long phone calls with you and those tears and laughters we have shared. Many thanks to my friends from Peking University, Zhaohan He, Hang Chi, Chao Shen, Langechuan Liu and Si Hui for all your help along the way. I also thank my friends from the University of Michigan Engineering School Yiting Zhang, Xuejing He, Yuntao Chen, Wei Tian and many others for all the great times we have had. Thank you Mom and Dad who have brought me to this world and accompanied me along all steps of my life. Your love and support has provided a great foundation for my future life and career.

This work is partially supported by the office of Science, U.S. Department of Energy, Award No. DE-SC0006684. Additional support came from Graduate Student Visitor Program from the Advanced Study Program in NCAR. Acknowledgement is also given to the high performance computing support provided by NCAR's Com-

putational and Information Systems Laboratory which is sponsored by the National Science Foundation. Without this support this dissertation would not be possible.

TABLE OF CONTENTS

LIST OF FIGURES

Figure

LIST OF TABLES

Table

LIST OF ABBREVIATIONS

AM Annular Mode

BDC Brewer-Dobson circulation

CAM Community Atmospheric Model

CF Convective Fraction

ECMWF European Centre for Medium Range Weather Forecasts

EIG Eastward Inertio-Gravity

ENSO El-Niño and Southern Oscillation

EOF Empirical Orthogonal Function

EP Eliassen-Palm

ER Equatorial Rossby

EUL Eulerian

FV Finite Volume

GCM General Circulation Model

GWD Gravity Wave Drag

HOMME High-Order Method Modeling Environment

HS Held-Suarez

HSW Held-Suarez-Williamson

IG Inertia-gravity

KH Kelvin-Helmholtz

MRG mixed Rossby-gravity

NAM Northern Annular Mode

NCAR National Center for Atmospheric Research

QBO Quasi-Biennial Oscillation

SAM Southern Annular Mode

SAO Semi-Annual Oscillation

SE Spectral Element

SST Sea Surface Temperature

SSW Sudden Stratospheric Warming

SLD semi-Lagrangian

TEM Transformed Eulerian Mean

WACCM Whole Atmospheric Community Climate Models

WIG Westward Inertio-Gravity

WMO World Meteorological Organization

ABSTRACT

An Assessment of the Quasi-Biennial Oscillation (QBO) and Sudden Stratospheric Warmings (SSWs) with Idealized General Circulation Models

by

Weiye Yao

Chair: Christiane Jablonowski

Advancing the predictive capabilities of atmospheric General Circulation Models (GCMs) necessitates a better understanding of the weather-climate interface and, in particular, the impact of the stratosphere on tropospheric predictability. However, the representation of stratospheric phenomena, including the tropical Quasi-Biennial Oscillation (QBO) and polar Sudden Stratospheric Warmings (SSWs), is still poor in current generation GCMs. This research advances the understanding of stratospheric simulations in GCMs and stratosphere-troposphere interactions.

Stratospheric QBO-like oscillations and SSW events are analyzed using different numerical methods which are provided in the four dynamical core of the National Center for Atmospheric Research's Community Atmosphere Model (CAM) version 5. The dynamical cores are driven by an idealized forcing named Held-Suarez forcing which consists of Rayleigh friction and a Newtonian temperature relaxation on a dry and flat earth. Three of the four models in CAM are able to generate QBO-like oscillations, but with different physical characteristics. The QBO-like oscillations

are mainly driven by tropical waves that are triggered despite the absence of typical wave generation mechanisms like moist convection. The differences thereby expose the effects of the CAM numerical schemes and their dissipation mechanisms on the QBO-like circulation. In addition, SSWs are simulated using similar idealized setups even without topographically generated planetary waves which are believed to be the most important SSW driving mechanisms. Wave and instability analyses are performed to examine the wave generation processes and the dynamics of the circulations in the four dynamical cores.

Furthermore, simulations with additional simple subgrid-scale processes such as gravity wave drag parameterizations and moist processes are introduced. These simulations enhance the complexity of the experimental setup and lead to an increase in wave activities and shortened QBO-like cycles. The thesis demonstrates that idealized dynamical core simulations expose fundamental characteristics of atmospheric circulations and thereby provide insight into the numerical designs of GCMs. It is suggested that idealized GCM configurations with increasing complexity serve as a paramount tool for model developments and tests.

CHAPTER I

Introduction

1.1 Stratospheric dynamics

The atmosphere is divided into different layers based on its vertical temperature profile. The tropospheric temperature decreases with height and the tropopause lies around 9 km at the poles and around 17 km at the equator. The stratosphere is the layer above the troposphere and extends to about 1 hPa and 50 km. Unlike the troposphere, the temperature profile in the stratosphere increases with height, from about 220 K at the tropopause and lower stratosphere to around 270 K at the stratopause. The observational data used for stratospheric research are mostly processed in the form of re-analysis data, which include upper air data from radiosonde, rockets, satellites and aircrafts.

The stratosphere greatly influences the troposphere. The distribution and transportation of tracer species highly rely on the stratospheric circulation and disturbances (*O'Sullivan and Chen*, 1996; *Shuckburgh et al.*, 2001). Some trace species in the atmosphere such as water vapor, carbon dioxide and ozone are radiatively active and very important to the Earth's radiative budget. Moreover, advancing our predictive capabilities to encompass e.g. seasonal time scales necessitates a better understanding of the weather-climate interface and, in particular, the impact of the stratosphere on tropospheric predictability. The latter is poorly understood. Strato-

spheric phenomena and especially extreme events greatly impact the tropospheric circulation over long time scales. The large-scale circulation in the stratosphere interacts with the troposphere and can influence the surface weather and climate (*Baldwin and Dunkerton*, 2001; *Gerber and Polvani*, 2009; *Garfinkel and Hartmann*, 2011a; *Garfinkel and Hartmann*, 2011b). The stratospheric circulation also serves as a wave filtering mechanism that greatly influences the mesosphere and other atmospheric layers above (*Holton*, 1984; *Dunkerton and Butchart*, 1984; *Dunkerton*, 1997; *Lieberman et al.*, 2013). The research on stratospheric circulation and stratospheric dynamics has been active for decades ever since the discovery of the Quasi-Biennial Oscillation (*Ebdon*, 1960; *Reed et al.*, 1961).

The stratosphere is generally dry and does not directly involve moist processes. The stratospheric circulation is driven by the solar insolation and upward momentum transport from the troposphere. The stratospheric/mesosphere circulation in the midlatitudes is dominated by westerlies in the winter hemisphere and easterlies in the summer hemisphere. Figure 1.1 (taken from *Andrews et al.* (1987)) shows a schematic depiction of the latitude-height distribution of the zonal wind. The figure highlights that the maximum/minimum wind speed for the polar jets are around 60 m s^{-1} (westerly jet) and - 50 m s^{-1} (easterly jet). Note that these maximum/minimum wind speeds lie around 0.1 hPa in the mesosphere. The stratospheric flow mostly follows the thermal wind balance, which relates the wind shear to the latitudinal temperature gradient. In the region between 30-60 km, the temperature increases rather uniformly from the winter pole to the summer pole, therefore a strong westerly jet dominates the mid-latitude winter hemisphere in the stratosphere, which is also called polar vortex (*Andrews et al.*, 1987).

Besides the variations of the upper atmospheric flow conditions related to the annual cycle, there are two phenomena in the stratosphere that are responsible for most of the stratospheric variability, the Quasi-Biennial Oscillation (QBO) in the

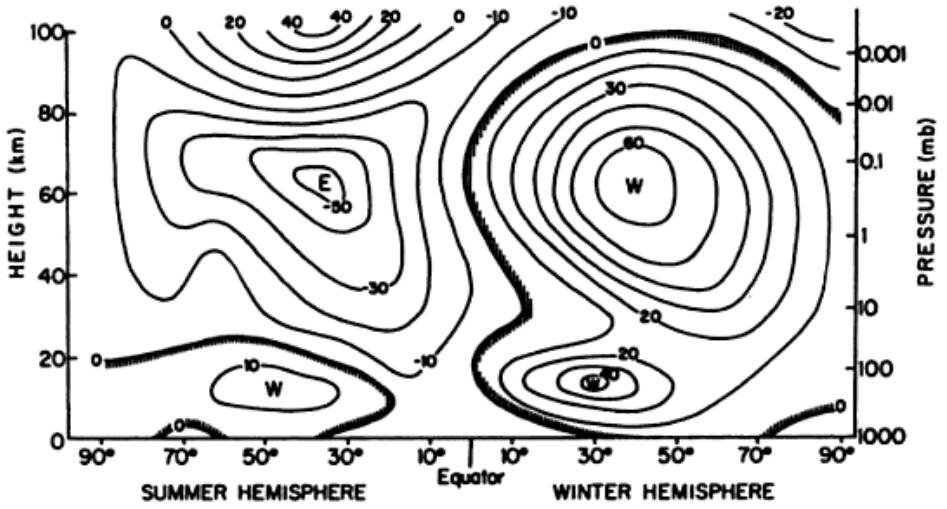

Fig. 1.4. Schematic latitude–height section of zonal mean zonal wind (m s^{-1}) for solstice conditions; W and E designate centers of westerly (from the west) and easterly (from the east) winds, respectively. (Courtesy of R. J. Reed.)

Figure 1.1: Latitude-height cross-section of the zonal-mean zonal wind (m s^{-1}) for solstice conditions. From *Andrews et al.* (1987), Chapter 1, Fig. 1.4.

tropics and the Sudden Stratospheric Warming (SSW)s in the winter hemisphere. Research on stratospheric dynamics is often focused on these two phenomena, that are both related to wave activities. Understanding of the QBO and SSWs is very important in stratospheric dynamics. The next two subsections briefly introduce these circulations.

1.2 Quasi-Biennial Oscillation (QBO)

In the equatorial middle atmosphere, the main flow variations are characterized by the Semi-Annual Oscillation (SAO) (peaked near 50 km (*Garcia et al.*, 1997)) and the Quasi-Biennial Oscillation (between 16 - 50 km) (*Andrews et al.*, 1987). The QBO is characterized by equatorial zonal wind changes from westerlies to easterlies with a period between 22 to 34 months, on average 28 months (*Baldwin et al.*, 2001). The QBO occupies the lower stratosphere from 100 - 1 hPa. Its amplitude has a Gaussian shape in the latitudinal direction and a half width of $\sim 12^{\circ}$ about the

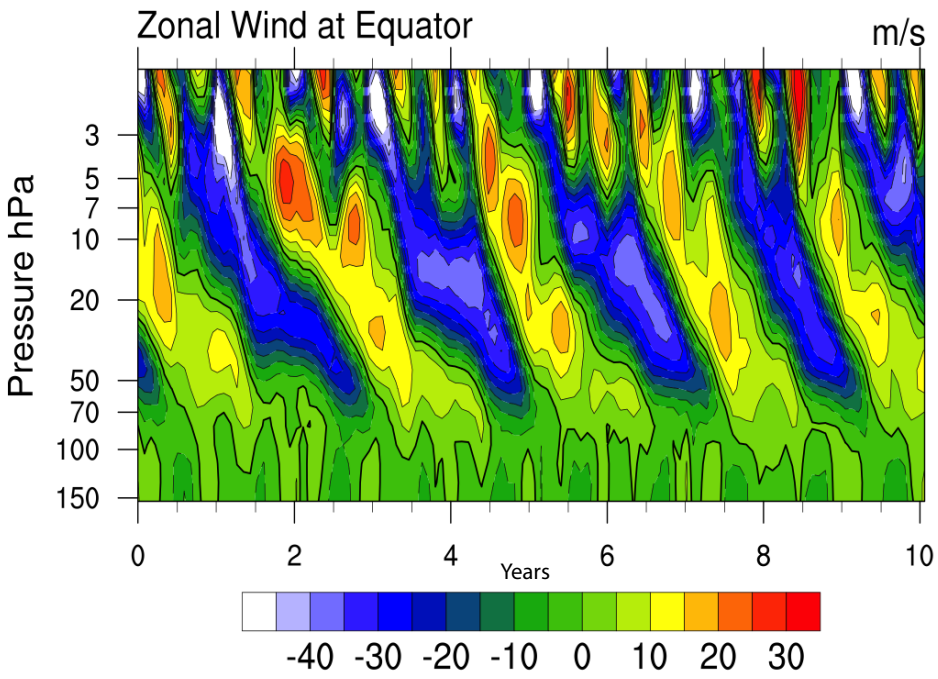

Figure 1.2: Data-assimilated observations from ECMWF Re-analysis (ERA40). 10-year time series (x-axis) of the monthly-mean zonal mean zonal wind at the equator. The average period is around 28 month.

equator. The minimum/maximum wind speed in the QBO region is about -35 m/s to 20 m/s (*Pawson and Fiorino*, 1998). Figure 1.2 from the European Centre for Medium Range Weather Forecasts (ECMWF) re-analysis dataset ERA-40 shows a 10 year time series of the equatorial monthly-mean zonal-mean zonal wind. The period is around 28 months. The QBO signal travels downward at about 1 km/month (*Baldwin et al.*, 2001). The temperature shows a very similar pattern as figure 1.2, and oscillates accordingly in the QBO regime. It satisfies the thermal wind relationship shown in Eq. 1.1 (*Andrews et al.*, 1987)

$$\frac{\partial u}{\partial z} = \frac{-R}{H\beta}\frac{\partial^2 T}{\partial y^2} \tag{1.1}$$

where u is the zonal wind, T is the temperature, z is the log-pressure height, y is latitudinal distance to the equator, R is the gas constant for dry air, $H = 7$ km is the scale height, and β is the latitudinal derivative of the Coriolis parameter at the

equator. The temperature anomalies in the QBO regime are about ± 4 K (*Baldwin et al.*, 2001).

The QBO is mostly generated and influenced by equatorial waves. The equatorial-trapped Kelvin waves provide a westerly force and mixed Rossby-gravity (MRG) waves provide an easterly force (*Lindzen and Holton*, 1968; *Holton and Lindzen*, 1972). However, the forcing provided by Kelvin waves and MRG waves is not enough to explain the QBO. Inertia-gravity waves and small-scale gravity waves are also important in the QBO forcing budget (*Dunkerton*, 1997).

In linear wave theory, a wave dissipates when its phase speed is close or equal to the background wind speed (*Holton*, 2004). The wave then deposits momentum to the background wind field, thereby accelerating/decelerating the mean flow. In the tropical stratosphere, this wave-mean flow interaction causes the jet oscillations. *Plumb and Bell* (1982) showed a model that explains the QBO mechanism. Initially the mean zonal wind is weak and westerly, the eastward propagating waves are dissipated at a low altitude and provide a westerly acceleration, which moves downward in time. The westward propagating waves penetrate to high altitudes and are dissipated there, thereby providing a westward acceleration to the mean wind at a high altitude. This wind shear propagates downward and eventually the westerlies are damped out as they approach the tropopause. The easterly waves then start to dissipate and slowly deposit momentum to the background flow. The background wind becomes weak and easterly, opposite to the start of the cycle. These westerly wind and easterly winds alternate in time and thereby oscillate.

The equatorial region is characterized by very active convective processes that are believed to be the major triggering mechanisms for the equatorial-trapped waves. The equatorial waves have different dispersion relationships and propagation properties depending on their direction. *Kiladis et al.* (2009) reviewed the basic theory of these waves. Their dispersion curves are shown in figure 1.3, which are derived from shallow

water theory. The dispersion relationship for trapped equatorial waves follows

$$\frac{\sqrt{gh_e}}{\beta}(\frac{\omega^2}{gh_e} - k^2 - \frac{k}{\omega}\beta) = 2n + 1 \quad n = 0, 1, 2... \tag{1.2}$$

where ω and k are wave frequency and wave number, respectively, h_e is the equivalent depth and n corresponds to the meridional mode number (except for Kelvin wave), with n = 0 corresponding to the MRG wave and n = -1 corresponding to a Kelvin wave. If we substitute the solutions back to the shallow water equations (not shown, Eqs (1) (2) and (3) from *Kiladis et al.* (2009)) with different mode numbers, we yield the full horizontal structures of the wave solutions, n=1 Equatorial Rossby (ER) wave, MRG wave, n=0 Eastward Inertio-Gravity (EIG) wave and n=1 and n=2 Westward Inertio-Gravity (WIG) wave. The wave frequency and wave number plotted in figure 1.3 are nondimensionalized ω^* and k^*, where $\omega^* = \omega/(\beta\sqrt{gh_e})^{1/2}$, and $k^* = k(\sqrt{gh_e}/\beta)^{1/2}$. These curves are widely used in wavenumber-frequency plots to identify different type of waves (*Wheeler and Kiladis*, 1999).

The meridional velocity perturbation vanishes for equatorial Kelvin waves, and follows the dispersion relation of $c = \sqrt{gh_e}$. The Kelvin wave travels eastward and its amplitude decays in the latitudinal direction from the equator. The MRG waves have peaks that lie around $\pm$ 10° N/S of the equator. For Kelvin waves the Eliassen-Palm (EP) flux is downward at each latitude, while the Rossby-gravity wave has an upward EP-flux (*Andrews et al.*, 1987). Moreover, for both wave modes the exponential decay of the EP flux with height is proportional to the radiative damping rate divided by the vertical component of the group velocity. The vertical group velocity for Kelvin waves is proportional to the phase speed c squared and for Rossby-gravity wave is proportional to the phase speed cubed. The Rossby-gravity wave amplitude has a damping rate that increases faster with $(\bar{u} - c) - > 0$ than that of the Kelvin wave (*Andrews et al.*, 1987).

These dispersion curves in figure 1.3 are normally noted as $\omega_0 = ck$, where ω_0 is

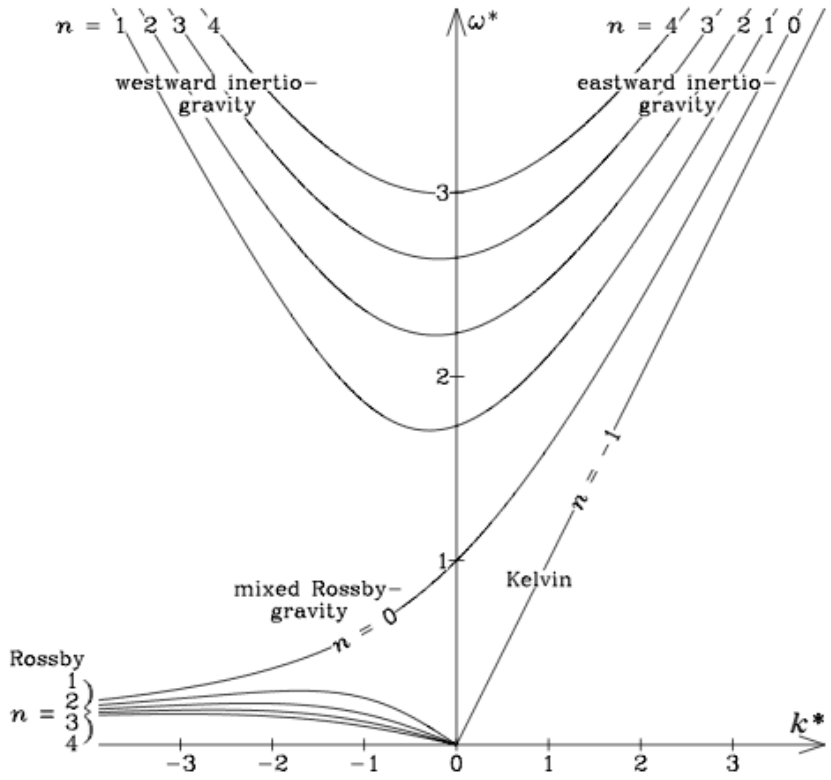

Figure 2. Dispersion curves for equatorial waves (up to $n = 4$) as a function of the nondimensional frequency, ω^*, and nondimensional zonal wave number, k^*, where $\omega^* \equiv \omega/(\beta\sqrt{gh_e})^{1/2}$, and $k^* \equiv k(\sqrt{gh_e}/\beta)^{1/2}$. For all but the Kelvin wave, these dispersion curves are solutions of equation (6). Westward propagating waves (relative to the zero basic state) appear on the left, and eastward propagating waves appear on the right. For consistency with equation (6), the Kelvin wave solution is labeled as $n = -1$.

Figure 1.3: Dispersion curves for equatorial waves (up to meridional mode number n=4), from *Kiladis et al.* (2009)

the wave frequency, c is the phase speed and k is the zonal wave number. When the wave is traveling in a mean flow with background speed $\bar{u}$, the wave speed about the surface becomes $\bar{u}+c$ according to the Doppler effect, and the dispersion relationship becomes $\omega = (\bar{u}+c)k = \omega_0 + \bar{u}k$. In the QBO region with steady background wind (the time scale of the mean flow change is much longer than the wave period), the effect of the Doppler shift is quite obvious (*Yang et al.*, 2011; *Yao and Jablonowski*, 2013). Therefore we have to take the background mean flow into account when analyzing the waves in the QBO region.

The QBO induces secondary circulations that are very important in tracer transport (*Plumb and Bell*, 1982; *Andrews et al.*, 1987; *Baldwin et al.*, 2001; *Choi et al.*, 2002; *Flury et al.*, 2013). In the equatorial stratosphere, the westerly and easterly winds are vertically stacked, and therefore appear as westerly shear zones ($\partial u/\partial z > 0$) and easterly shear zones ($\partial u/\partial z < 0$) alternatively. The thermal wind relationship requires a warm anomaly in the westerly shear zone and cold anomaly in the easterly shear zone. In order to maintain these temperature anomalies, there needs to be sinking motion in the warm anomaly region and rising motion in the cold anomaly domain; corresponding to sinking motions ($\bar{\omega} > 0$) in westerly shear zones ($\partial u/\partial z > 0$), and rising motions ($\bar{\omega} < 0$) in easterly shear zones ($\partial u/\partial z < 0$). These sinking and rising motions induce horizontal convergence near the maximum westerly jet zone and divergence in the maximum easterly jet zone, thereby inducing a secondary circulation.

This secondary circulation is often observed in tracer transport assessments for e.g. water vapor and ozone (*O'Sullivan and Chen*, 1996; *Shuckburgh et al.*, 2001; *Choi et al.*, 2002). The secondary circulation induced by the QBO also modifies the Brewer-Dobson circulation (BDC) (*Flury et al.*, 2013). Since the BDC has a seasonal cycle and the QBO period is also slightly affected by seasons and some other factors, e.g. the El-Niño and Southern Oscillation (ENSO), this interaction can be

very complicated (*Peña-Ortiz et al.*, 2008; *Flury et al.*, 2013).

The QBO also influences the troposphere. The influence is mostly through the influence of the QBO on the polar vortex, through a mechanism called Holton-Tan effect (*Holton and Tan*, 1980). During the easterly QBO, mid-latitude waves are not able to propagate into the tropical region, and are therefore mostly confined to the mid-latitudes. This induces stronger wave-mean flow interactions and more frequent polar-vortex break downs. Therefore, Sudden Stratospheric Warmings happen more frequently during easterly QBO phases. *Garfinkel and Hartmann* (2011a) show subtropical jet shifts between QBO phases which have a zonally asymmetric feature, e.g. a poleward shift of the subtropical jet and a weakening of the jet is observed in the Pacific region. In addition, the QBO influences the troposphere mainly by modifying the tropospheric eddies, and there is a QBO-ENSO teleconnection that impacts the tropospheric climate (*Yuan et al.*, 2013).

1.3 Sudden Stratospheric Warming

SSWs are responsible for most of the stratospheric variability in the mid and high latitudes. The winter stratosphere is dominated by a westerly jet (shown in figure 1.1) and the zonal-mean temperature decreases towards the winter pole. Every one or two years, this structure is dramatically disrupted when a reversal of the zonal wind direction and latitudinal temperature gradient occurs for a brief period. The stratospheric polar temperature then increases by 40-60 K within a week at about 10 mb. This phenomenon is called a Sudden Stratospheric Warming (*Andrews et al.*, 1987). Figure 1.4 shows the evolution of the temperature field at 10 hPa for one SSW event in the northern hemisphere from an idealized simulation which will be discussed later in this dissertation. It is defined as a "major warming" event if it coincides with a reversal of the zonal wind direction at 60° latitude, and a "minor warming" if only the temperature increases at the pole. In nature, SSWs mostly

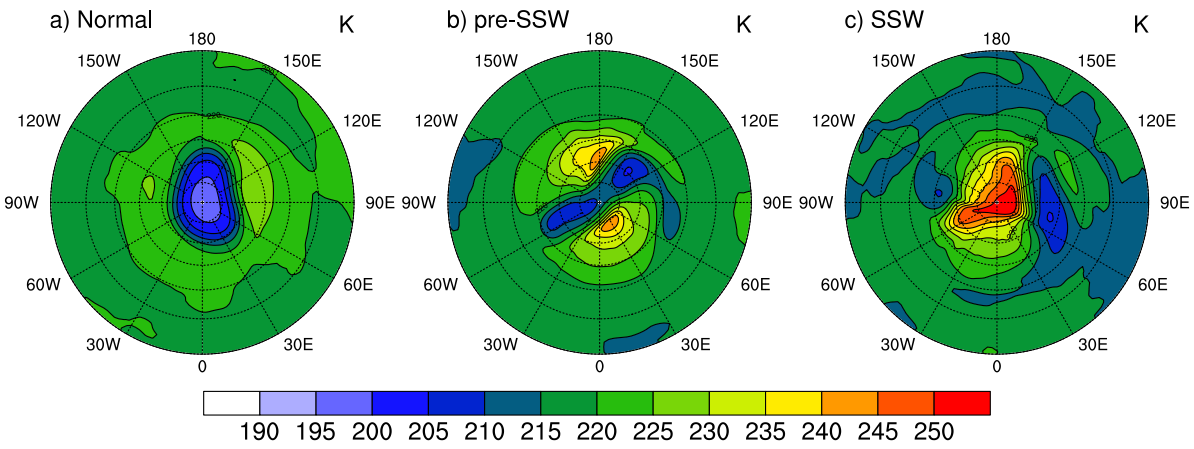

Figure 1.4: North-polar stratospheric projection of the temperature (K) before, at the onset and during an SSW event at 10 hPa. Dashed circle lines shows latitude levels at 15° grid spacing. Idealized simulation with Community Atmospheric Model 5

happen in the Northern Hemisphere. The occurrence of SSWs can be modulated by many natural factors, including the 11-year solar-cycle, ENSO, QBO and so on.

SSWs are mostly generated and influenced by tropospheric planetary (Rossby) waves (*Matsuno*, 1971). SSWs tend to occur with tropospheric blocking events, which involve strong, long-lasting and quasi-stationary distortions and easterly planetary waves (*Naujokat et al.*, 2002; *Wang and Alexander*, 2009). Zonal wavenumbers 1 and 2 are essential for the development of SSWs since they are able to propagate upwards into the stratosphere (*Matsuno*, 1971; *Holton*, 1976; *Holton*, 2004). The SSW mechanism, similarly to the QBO, also happens through wave-mean flow interactions. A northward shift of the polar jets and eastward traveling wavenumber 1 and 2 are believed to be very important for the SSW initiation (*Andrews et al.*, 1987).

In mid-latitudes, the planetary or Rossby waves are the result of the meridional potential vorticity gradient. We classify them into two categories distinguished by their excitation mechanisms: free waves and forced waves. The most important mode of the free traveling planetary waves is the 5-day wave which travels westward with

zonal wavenumber 1. However, the forced planetary waves are more important and stronger compared to the free planetary waves (*Holton*, 2004). The forcing of such waves is mainly via diabatic heating and flow over topography.

Other than the wave-mean flow interaction, the wave-wave interaction and instability conditions are also important in the SSW mechanism. *Hsu* (1981) stated that wave-wave interactions tend to result in increased wave activity and stronger polar warmings in SSW simulations. Shear instability also plays a role in the development of sudden warmings (*Andrews et al.*, 1987).

Despite the fact that the influence of the tropospheric activity on the stratospheric circulation has been known for decades, the influence of the stratosphere on the troposphere has only been assessed very recently. *Baldwin and Dunkerton* (2001) showed that the SSWs can be detected as a negative phase Annular Mode (AM) signal, which is characterized by north-south shifts of atmospheric mass between the polar regions and the mid-latitudes, including a Northern Annular Mode (NAM) and a Southern Annular Mode (SAM) in the different hemispheres, respectively. The SSW induced pressure anomaly travels downward into the troposphere at a time scale of 30-60 days. The annular modes are known to modulate the surface weather systems, including the positions of mid-latitude troughs and ridges, tropical storm tracks, etc. Therefore, the processes in the stratosphere can influence extreme events at the surface (*Thompson and Solomon*, 2002; *Thompson et al.*, 2002). However, the mechanism of this troposphere-stratosphere coupling is still unclear.

1.4 QBO and SSW simulations

General Circulation Model (GCM) are widely used in weather and climate research. GCMs simulate the atmospheric circulation by solving the fluid dynamics equations (dynamical cores) and subgrid-scale physical parameterizations. If all of the key physical processes were captured in a GCM, then it should provide a rather

realistic circulation, meaning the important features of the atmosphere need to be resembled in the simulations. The features of the tropospheric flow are generally simulated quite well. In contrast the stratospheric simulations are often of poorer quality, partly due to a historic lack of resolution and partly due to the lack of understanding of stratospheric phenomena. One of the primary roles of the GCM in the middle atmosphere is to test the adequacy of our understanding of physical processes and how they impact the circulation. For example, a deficiency in representing equatorial gravity waves in a GCM can result in the absence of the QBO circulation. Correct simulations of the stratospheric circulation are also very important for tracer transport assessments. For example, the transport of water vapor, carbon dioxide and ozone which are the main solar energy absorbers, are crucial for atmospheric chemistry and the radiative balance. Improving the representation of the QBO and SSW in GCMs can enhance the surface weather and climate predictability, especially over time scales of 1-2 months.

The first successful QBO simulation in a GCM was conducted by *Takahashi and Boville* (1992) with forced Kelvin waves and Rossby-gravity waves. However, those waves are supposed to be spontaneous in GCMs. *Takahashi* (1996), *Takahashi* (1999), *Scaife et al.* (2000), *Scaife et al.* (2002), *Hamilton et al.* (2001) and *Giorgetta et al.* (2002, 2006) were among the first that simulated QBOs or QBO-like simulations without prescribed wave forcings. More recently, *Kawatani et al.* (2010), *Orr et al.* (2010), *Xue et al.* (2012), *Yao and Jablonowski* (2013) and *Richter et al.* (2014a) also reported on successful QBO or QBO-like simulations. A precondition for successful QBO-like simulations is high vertical resolution with grid spacings around $\Delta z = 1$ km or finer to resolve vertically propagating waves and proper wave generation mechanisms (mostly convective parameterization). In addition, Gravity Wave Drag (GWD) parameterizations are often employed to mimic the effects of unresolved subgrid-scale gravity waves (*Kim et al.*, 2003). Moreover, the choice of the numerical scheme in

solving the fluid flow equations and the numerical diffusion mechanisms in GCMs may also affect the QBO behavior.

SSW simulations and predictions have a much longer history than QBO simulations. *O'Neill* (1980) and *Grose and Haggard* (1981) are among the first that successfully simulated spontaneous SSWs with coarse vertical and horizontal resolutions (vertical spacings larger than Δ z = 3 km and horizontal scales larger than 300 km in the tropics). In addition, *Simmons and Strüfing* (1983) used a modified version of the European Centre for Medium Range Weather Forecasts (ECMWF) model to simulate an SSW forecast. Later SSW studies with GCMs include the work by *Erlebach et al.* (1996), *Manzini and Bengtsson* (1996), *Polvani and Kushner* (2002), *Charlton et al.* (2007), *Gerber and Polvani* (2009), *Sun et al.* (2012), *Jucker et al.* (2014) and *Hitchcock and Simpson* (2014).

Although SSWs have been successfully simulated for decades, the factors that determine their initiation, evolution and frequency are still not fully understood. Therefore, idealized SSW simulations are often utilized to unveil the dynamical processes of this phenomenon (*Polvani and Kushner*, 2002; *Kushner and Polvani*, 2004; *Gerber and Polvani*, 2009; *Sun et al.*, 2012; *Jucker et al.*, 2013, 2014). Most of these idealized simulations used temperature relaxation and Rayleigh friction to mimic the physics forcing in the atmosphere including radiative forcing and boundary layer friction, inspired by the idea in *Held and Suarez* (1994). Most often idealized topography is needed in these simulations. The downward influence of the SSW events can also be simulated in such idealized simulations, e.g. see *Gerber and Polvani* (2009), which mimic the SSW events in nature (*Baldwin and Dunkerton*, 2001). Generally speaking, SSW simulations are not as demanding as QBO simulations, but it is still a challenge to model SSW events and their climatology accurately.

1.5 Gravity Wave Drag (GWD) parameterizations

As mentioned in section 1.2, gravity waves are crucial in QBO simulations. However, the spatial scale of the gravity waves varies from a few kilomiters to thousands of kilometers, and wave-lengths that are shorter than 500 km cannot be captured by current resolutions of GCMs (often 100-200 km grid spacing) (*Kim et al.*, 2003). Those subgrid-scale gravity waves must be parameterized, not only for the purpose of a QBO simulation, but for improving the simulation of the atmospheric circulations, e.g. the reduction of the westerly bias and cold-pole problem in the stratosphere (*Boville*, 1995). The basic idea behind GWD parameterizations is to launch waves artificially and let the waves travel upward until they become unstable. The waves will then break and deposit momentum to the background mean flow (*Lindzen*, 1981). This process is inspired by the wave breaking process in nature. However, the gravity wave generation processes in GCMs vary widely. Some GCMs use prescribed wave spectra, others relate the launch of the gravity waves to the flow characteristics like frontal zones or convection as further explained below.

There are two types of gravity waves depending on the wave generation mechanism: orographic and non-orographic. Orographic GWD refers waves which are generated by a flow over topography (*McFarlane*, 1987). Waves generated from non-orographic sources are less well understood (*Kim et al.*, 2003). In tropical regions, the gravity waves are mostly generated by deep convection. Other sources like jet streams and fronts are also important in non-orographic GWD (*Plougonven et al.*, 2003). In older GWD schemes, non-orographic gravity waves are parameterized by launching a wave spectrum that is a prescribed function of location and season (*Garcia et al.*, 2007). In more recent GWD schemes, gravity waves are launched according to trigger functions that depend on the atmospheric state (*Beres et al.*, 2005; *Richter et al.*, 2010; *Schirber et al.*, 2014). For example, the GWD scheme by *Beres et al.* (2005) connects the convective heating from the deep convection parameterization by

Zhang and McFarlane (1995) to the gravity wave activity. However, there are still unsolved questions and uncertainties with current convection parameterizations. This flow-dependent non-orographic GWD scheme has greatly improved QBO simulations as well as the GCM behavior (*Richter et al.*, 2014a,b)

The 'critical layer' is one of the most important concepts in wave breaking. The critical layer is the "altitude where the wind speed component along the wave's horizontal wave vector equals its phase speed c, $c = \bar{U}(z_C)$", where z_C is the critical level (*Kim et al.*, 2003; *Lindzen*, 1981). The waves are fully dissipated when they reach the critical layer.

Gravity waves conserve their horizontal wave momentum flux density under the assumption of no dissipation. For east-west gravity waves, the momentum flux is given by $\rho\overline{u'w'}$, where u' and w' are the zonal and vertical velocity perturbations of the wave. The GWD parameterization then computes the vertical gradients of the momentum flux that are produced by saturated waves. 'Saturated' denotes the state when waves become unstable as their amplitudes increase when traveling upward. If saturation occurs, wave energy is dissipated to bring the wave back to marginal stability (*Fritts*, 1984; *Dunkerton*, 1989; *McFarlane*, 1987). Parameterized gravity waves can go through several saturation states before reaching the critical layer which fully dissipates them (*Xue et al.*, 2012).

1.6 Idealized GCM simulations

The QBO and SSWs have been simulated by GCMs in many previous studies, most of them used rather realistic setups which utilize a GCM package with full physical parameterizations. However the role of the dynamical cores, more specifically the numerical scheme used to solve the fluid dynamic equations of the GCMs, has never been addressed. This is not straightforward, since the components of GCMs, such as the dynamical core, the physics package, diffusion, etc., interact with each

other and it is therefore hard to isolate the role of each individual component. In this thesis, we test the role of the dynamical cores in QBO and SSW simulations using the Community Atmospheric Model (CAM) which has been developed by the National Center for Atmospheric Research (NCAR) and various U.S. Department of Energy (DOE) Laboratories.

CAM has four dynamical cores, which are the spectral transform semi-Lagrangian (SLD), Finite Volume (FV), Eulerian (EUL) and Spectral Element (SE) dynamical cores. The latter one is CAM's current default in CAM 5.3 (*Neale et al.*, 2010). A detailed model description is provided in Chapter III. SLD and EUL are spectral transform schemes which were developed in the 90s (*Williamson and Olson*, 1994). These models are computationally cheap and accurate, but suffer from Gibbs ringing (*Lauritzen et al.*, 2011). The spectral transform methods are still used for weather and climate simulations. The FV dynamical core (*Lin* (2004)), is mass-conserving which is very important for tracer transport. Therefore it was chosen for the Whole Atmospheric Community Climate Models (WACCM) which contains an atmospheric chemistry component (*Neale et al.*, 2010). Like FV, the SE dynamical core is mass-conserving and also suitable for the atmospheric chemistry modeling purpose. SE uses a cubed-sphere grid which avoids the polar singularity of traditional latitude-longitude grids.

In order to test the sensitivity of numerical schemes, we use the idealized physics forcing by *Held and Suarez* (1994) which additional Rayleigh friction near the model top. This forcing replaces CAM's physical parameterization package and simplifies the physics interactions with the dynamical core. The idealized simulation has no topography or moisture. The Held-Suarez (HS) forcing consists of Rayleigh friction of the low-level winds, which mimics boundary layer friction and a Newtonian relaxation of the temperature field towards a prescribed equilibrium temperature which is isothermal above 100 hPa. The pressure-latitude cross-section of the equilibrium

temperature field is showen in figure 1.5a. Horizontally, the equilibrium temperature is warm in the tropics and decreases with latitude towards the poles. The equilibrium temperature decreases with height and remains isothermal when it reaches 200 K at about 200 hPa in the tropics. A modified version of the Held-Suarez forcing by *Williamson et al.* (1998) (Held-Suarez-Williamson (HSW)) is used for the SSW simulations, shown in figure 1.5b with a logarithmic pressure scale. This temperature profile is warm in the tropics and cold at the poles. In the stratosphere, temperature increases with height in the tropical and mid-latitude regions, but decreases with height in polar regions. This modified forcing keeps the same prescribed temperature in the troposphere as in figure 1.5a, with an additional latitudinal temperature gradient in the stratosphere above 100 hPa, thereby triggering polar vortices. The temperature field in figure 1.5b is slightly modified from *Williamson et al.* (1998) to fit our high model setup as explained in Chapter IV.

1.7 Overview of the thesis

The thesis is structured as follows. In Chapter II we show that spontaneous QBO-like oscillations can be simulated in the dry SLD dynamical core when driven by the simple *Held and Suarez* (1994) forcing. The QBO-like oscillations are generated despite the absence of typical wave triggering mechanisms like moist convection. The QBO-like signal has a long period between 42-45 months and occurs in the upper stratosphere, slightly higher than observations. However, the amplitudes, asymmetries and meridional extent closely resemble the observed QBO. We analyze the tropical waves and their wave-mean flow interaction. The research shows that the numerical diffusion of the SLD dynamical core plays a decisive role as a wave dissipation mechanism (*Yao and Jablonowski*, 2013).

Chapter III analyzes QBO-like oscillations in all four Community Atmospheric Model (CAM) dynamical cores to understand the impact of the numerical schemes

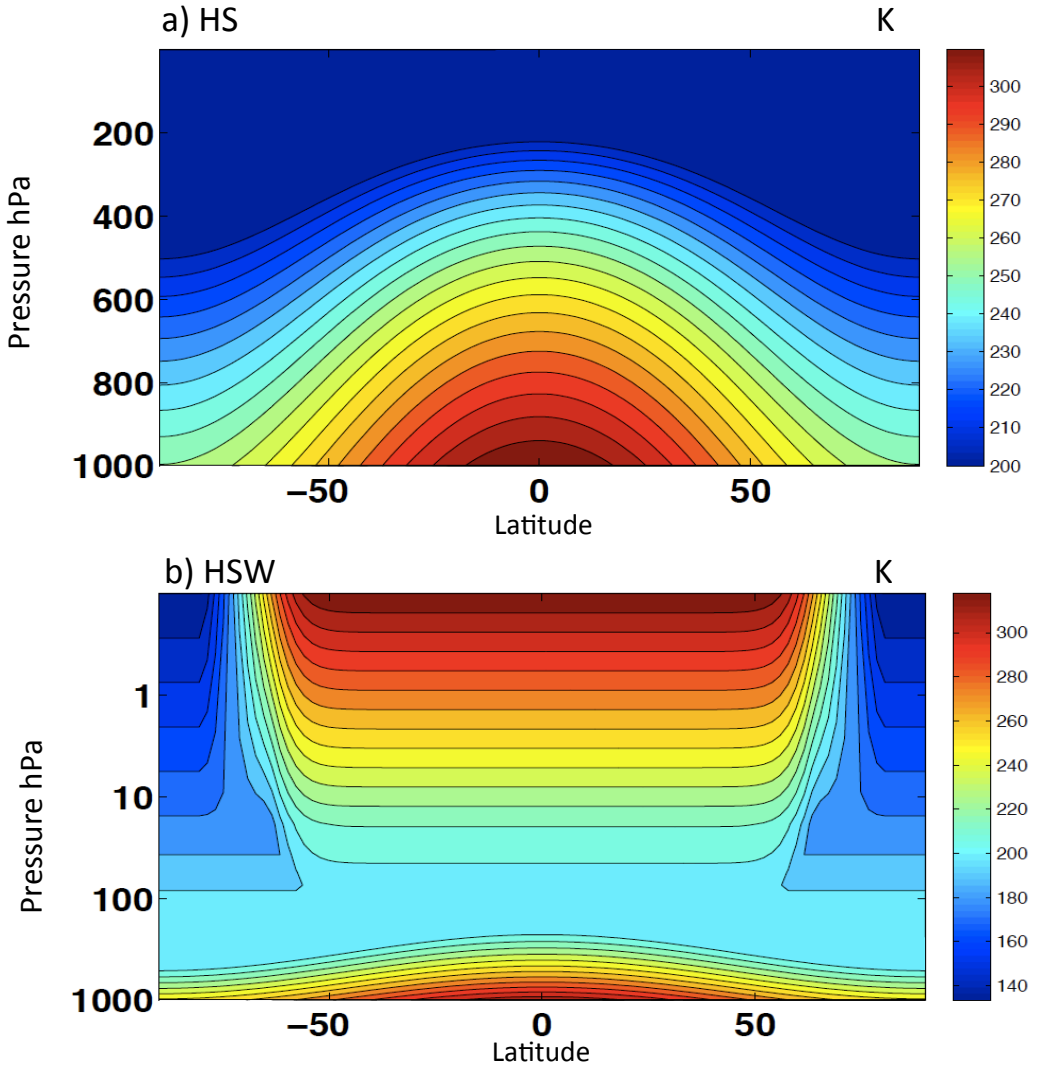

Figure 1.5: Pressure-latitude cross-section of equilibrium temperature for the a) HS forcing (linear pressure scale for better troposphere view) and b) HSW forcing (logarithmic pressure scale)

on tropical waves and wave-mean flow interactions. The research sheds light on the occurrences of dynamic instabilities that have the potential to act as wave triggering mechanisms. The FV dynamical core exhibits very infrequent regions of instability and generates the fewest waves in comparison to others (*Yao and Jablonowski*, 2014). This gives guidance concerning the adequate choice of GCM numerical schemes for wave-dominated phenomena.

The stratospheric circulation is most variable during SSWs, when the polar vortex is disturbed by planetary-scale Rossby waves. The coupling between the stratosphere and troposphere is strongest before and after SSW events. SSWs are mainly caused by vertically propagating planetary-scale waves from the troposphere and their interaction with the zonal flow. In particular, orographically generated waves are believed to play a major role. In Chapter IV we demonstrate that SSWs can also be simulated in dynamical cores that are driven by the Held-Suarez forcing with the stratospheric variation by *Williamson et al.* (1998). The SSWs appear in both hemispheres, even in the absence of convectively or orographically forced waves. SSWs travel downward, reach the surface after 30-60 days and thereby have an impact on the lower atmosphere. In nature, this often causes colder and stormier conditions during the winter. Our research exposes the characteristics of planetary waves in the different dynamical cores and explains the impact of the numerical schemes.

The main difficulty in simulating the QBO with GCMs is the representations of subgrid-scale processes, like moist convection, that act as wave triggers and thereby impact the wave-mean flow interactions. We add a simplified moist physics package with large-scale condensation (*Reed and Jablonowski*, 2012) to the idealized Held-Suarez experiments and evaluate the impact of two very different subgrid-scale gravity wave drag (GWD) parameterizations. Their wave source spectra are either prescribed or depend on the heating due to moist processes (*Beres et al.*, 2005; *Lindzen*, 1981). We shed light on the impact of the subgrid-scale forcings on tropical waves and

investigate how they modulate and improve the QBO in GCMs.

The thesis ends with a summary and discussion of future work in Chapter VI.

CHAPTER II

Spontaneous QBO-like Oscillations in an Atmospheric Model Dynamical Core

2.1 Introduction

The Quasi-Biennial Oscillation (QBO) is a phenomenon in the equatorial stratosphere that occupies the region between 100-3 hPa. This region is characterized by a downward propagating zonal wind regime that periodically changes from westerlies to easterlies. The observed QBO period from reanalysis data is about 22 to 34 months, with an average of approximately 28 months. The oscillation is primarily driven by upward propagating waves and their interaction with the mean flow (*Holton and Lindzen*, 1972). In particular, trapped equatorial Kelvin and mixed-Rossby gravity (MRG) waves provide large portions of the westerly and easterly momentum forcing, respectively. In addition, inertia-gravity (Inertia-gravity (IG)) waves and small-scale gravity waves are other main contributors to the forcing (*Baldwin et al.*, 2001).

Although the QBO is a tropical oscillation, its impact is felt throughout the global stratosphere, and even in the troposphere and mesosphere. Therefore, the ability of an atmospheric General Circulation Model (GCM) to simulate the QBO is considered an important model characteristic. Progress has been made in simulating spontaneously-generated QBOs in GCMs since 1996. However, the mix of waves

and their wave mean-flow interaction mechanisms are rather different in each GCM. Some models exclusively drive the QBO by resolved waves, which are triggered by the moist convection parameterization (*Hamilton et al.*, 2001). Such simulations need to be viewed with care since overreactive convective schemes can lead to unrealistic precipitation (*Takahashi*, 1999). Other models employ an additional gravity wave drag (GWD) parameterization to provide an extra momentum source that mimics the effects of unresolved small-scale gravity waves (*Giorgetta et al.*, 2006; *Xue et al.*, 2012). But since various GWD schemes are prevalent in GCMs, their net momentum forcing varies widely and necessitates the empirical tuning of the GWD strength to obtain a realistic oscillation (*Giorgetta et al.*, 2006). It is thereby possible that GCMs exhibit QBO-like oscillations for very different, possibly wrong or error-compensating, reasons in comparison to nature. *Giorgetta et al.* (2006) also reported on the sensitivity of the QBO simulation to the vertical grid spacing. They found that stratospheric grid spacings of around 1 km or finer were required which has been reaffirmed by most studies. Such fine grid spacings ensure that upward traveling waves and their wave-mean flow interactions are captured.

All aforementioned 3D GCM simulations of the QBO were driven by comprehensive physical parameterization packages. Such setups incorporate highly nonlinear interactions between, for example, the dynamical core and moist convection or the GWD parameterization. This makes it difficult to distinguish the causes and effects of waves and their wave damping mechanisms. This chapter aims at disentangling these interactions. It focuses on the role of a dry GCM dynamical core in QBO-like simulations that omit the typical wave triggers like moist convection or GWD which are generally believed to be paramount for the QBO wave forcing. In particular, we discuss the curious finding that spontaneous QBO-like oscillation are supported in the semi-Lagrangian (SLD) dynamical core of the Community Atmosphere Model (CAM) (*Neale et al.*, 2010) that has been developed at the National Center for Atmospheric

Research (NCAR). The dynamical core is isolated from the physical parameterizations via the *Held and Suarez* (1994) forcing. The study thereby allows an in-depth look at the wave characteristics of the dry dynamics in the QBO region, assesses the wave-mean flow interactions through Transform Eulerian Mean (Transformed Eulerian Mean (TEM)) analysis, and sheds light on the role of diffusion as a contributing, mostly counteracting, switching mechanism.

The chapter provides a description of the experimental design in Chapter 2.2. Chapter 2.3 presents the physical characteristics of the QBO-like simulation, followed by wavenumber-frequency and TEM analyses in Chapter 2.4. Conclusions are given in Chapter 2.5.

2.2 Experimental design

Our study is based on an idealized 20-year long simulation with the spectral SLD dynamical core in the CAM version 5.0 (CAM5) framework. The SLD dynamical core is a two-time-level, semi-implicit, semi-Lagrangian spectral-transform model that utilizes a quadratic Gaussian transform grid. We run the model with 55 vertical levels and a model top at 0.1 hPa. The maximum vertical grid spacing is about 1.25 km in the stratosphere. The horizontal resolution is a triangular truncation of T63, which corresponds to about 2° (220 km) grid spacing near the equator. The time step is $\Delta t = 2700$ s. Neither a total energy fixer, nor explicitly-applied diffusion is used. However, the cubic interpolations in the semi-Lagrangian scheme introduce implicit numerical diffusion which resembles fourth-order hyper-diffusion as argued by *McCalpin* (1988). The model is initialized with a snapshot of a spin-up SLD run after the QBO-like oscillations have become regular.

The QBO-like simulation is driven by the idealized *Held and Suarez* (1994) (HS) physics forcing that replaces CAM's physical parameterization package. Neither topography nor moisture are present. The Held-Suarez forcing consists of Rayleigh

friction (RF) of the low-level winds and a Newtonian relaxation of the temperature field towards a prescribed equilibrium temperature which is isothermal above 100 hPa. These forcings thereby mimic the effects the boundary-layer friction and radiation. The Newtonian damping rate in the stratosphere is 1/40 day^{-1}. Additionally, we apply RF ($-K_r u$) to the zonal wind field u from 1hPa upwards to dissipate upward traveling waves and minimize wave reflections at the model top. In essence, the additional RF acts like a sponge layer. Following *Boville* (1986) the expression for the pressure-dependent RF coefficient is given by $K_r = k_0 * (1 + tanh((z - z_0)/H_0))$. The damping coefficient k_0 is set to 1/3 day^{-1}, the log-pressure height is $z = h_0 \ln(p_0/p)$, p symbolizes pressure, the reference pressure p_0 is set to 1000 hPa, and h_0 stands for a scale height of 7 km. In addition, the parameter for the model top z_0 is set to 61 km and the scale factor H_0 is 7.7 km. This leads to the damping time scales $1/K_r$ of about 41 days at 1 hPa and 2 days at the model top with 0.1 hPa.

2.3 Characteristics of the QBO-like oscillation

The SLD dynamical core spontaneously generates a QBO-like oscillation in the tropical stratosphere with periods between 42-45 months (43.5 months on average). This is shown in Fig. 2.1a that displays the time-pressure cross section of the monthly-mean zonal-mean zonal wind averaged between $\pm 2^\circ$ N/S. The vertical domain of the oscillation extends from 1 hPa to about 30 hPa in the westerly phase, and to about 50 hPa in the easterly phase before the easterly branch transitions into the steady easterly jet between 100-50 hPa. The vertical position of the oscillation is too high in comparison to observations (100-3 hPa) which is a common issue in many QBO simulations (*Giorgetta et al.*, 2006; *Xue et al.*, 2012). The period is longer than the observed QBO period due to a weaker wave forcing in the SLD simulation, since moist convective processes or GWD are absent. The onset of the QBO-like oscillation in SLD at 1 hPa coincides with the bottom position of the RF sponge layer, which

damps the oscillation effectively between 1-0.1 hPa.

The SLD simulation exhibits many realistic features. The westerly phases descend faster than the easterly phases and have lower amplitudes, in agreement with observations. The minimum/maximum velocity range between -35 m s^{-1} and 10 m s^{-1} is also met rather well. The asymmetry of the oscillating wind regime is connected to the differing strengths of the driving waves. In addition, the westerly phases which last 28-32 months at 10 hPa, are longer-lived in the lower QBO domain and the time between maximum easterlies and maximum westerlies is generally shorter than the other way around.

Figure 2.1b shows the time-latitude cross-section of the mean zonal wind at 4.9 hPa which is close to the region of maximum amplitude. The figure confirms that the oscillating wind regime is a tropical phenomenon. It is confined to the tropical region between $\pm 30^{\circ}$ with a halfwidth of about $10 - 12^{\circ}$. Note though that the westerly winds have a narrower meridional width than the observed QBO westerlies (see *Pawson and Fiorino* (1998)).

2.4 Analysis

In order to examine the resolved wave activity, an equatorial wavenumber-frequency analysis is utilized following the method in *Wheeler and Kiladis* (1999). The analysis (Fig. 2.2) is based on six-hourly instantaneous temperature data that were collected for a 50-month time period from approximately year 7 onwards. The corresponding equatorial monthly-mean zonal-mean zonal wind field is displayed in Fig. 2.3a by the overlaid white contours. This 50-month period is a few months longer than one complete QBO cycle. For the Wheeler-Kiladis diagrams we choose a model level close to 22 hPa which lies in the lower domain of the QBO-like oscillation. Such a level guarantees that most of the upward traveling equatorial waves can be detected before they get filtered further upwards by the ambient flow (*Yang et al.*, 2011). In addition,

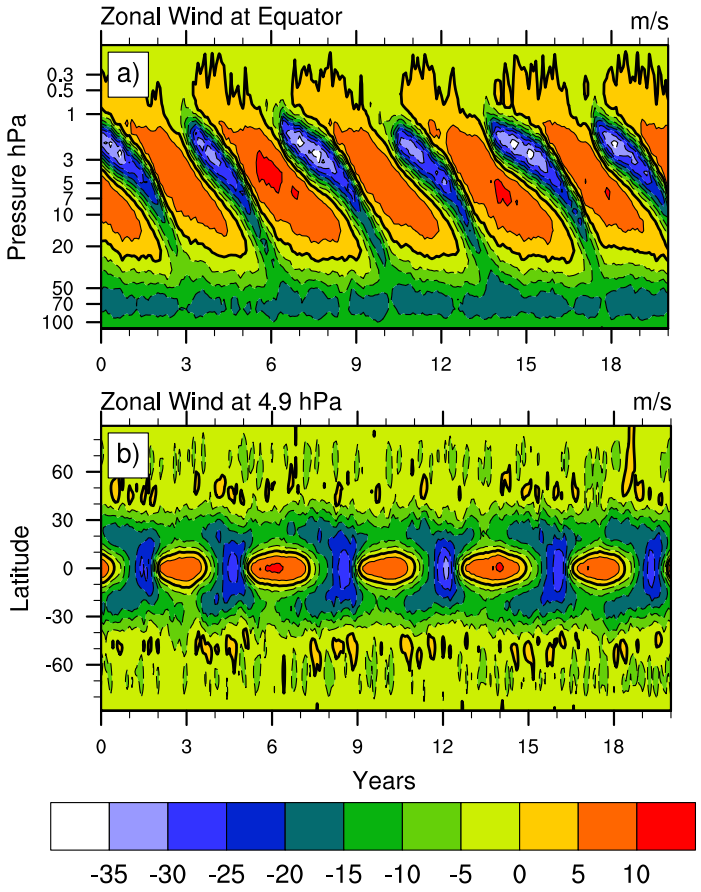

Figure 2.1: Monthly-mean zonal-mean zonal wind: a) time-pressure cross section averaged between 2° N/S, b) time-latitude cross section at 4.9 hPa.

Yang et al. (2011) showed how the wavenumber-frequency spectra are impacted by the Doppler shift in the presence of different zonal background velocities. From linear shallow water theory, the background wind modifies the dispersion curves according to $\omega = \omega_0 + \bar{u}k$ where ω and ω_0 are the wave frequencies with and without the Doppler shift, $\bar{u}$ denotes the zonal background wind and k stands for the zonal wavenumber. Figure 2.1a displays that most of the region below 22 hPa is dominated by easterlies. We therefore select $\bar{u} = -8$ m s^{-1}.

In Fig. 2.2 we overlay the Doppler-shifted dispersion curves for the equivalent depths h of 12, 50, and 200 m. These equivalent depths correspond to the zonal wave speeds of about 11, 22 and 44 m s^{-1} and approximate vertical wavelengths L_z of 2.8, 6.2 and 12.6 km, assessed with the squared stratospheric Brunt-Väisälä frequency $N^2 \approx 5 \times 10^{-4}$ s^{-2}. This range of phase speeds and vertical wavenumbers encapsulates the typical range of observed equatorially trapped waves in the stratosphere like Kevin and MRG waves. Thereby, our analysis sheds light on their presence in idealized simulations that omit important wave generation mechanisms. Figure 2.2 displays the anti-symmetric and symmetric wavenumber-frequency spectra which are averaged between 15° N/S. The estimated background spectrum has been removed (see *Wheeler and Kiladis* (1999)). The anti-symmetric plot (a) shows a spectral peak for MRG waves with periods around 3-4 days and negative wavenumbers -4– -6. Such negative wave numbers denote a westward propagation. The wavenumber-frequency range between -3– -5 with frequencies ≤ 0.3 cycles per day (cpd) is also indicative of free Rossby waves. Moreover, spectral peaks are detected for eastward traveling Equatorial Inertia-Gravity (EIG) waves with meridional mode number $n = 0$. These EIG waves have shorter periods of around 2-3 days within the wavenumber range 2-7. At higher wavenumbers, a mix of EIG and IG waves is detected. The symmetric plot (Fig. 2.2b) displays the Doppler-shifted dispersion curves for Kelvin, Equatorial Rossby (ER) and $n = 1$ IG waves. Spectral peaks for ER waves between wavenumbers

-2 and -4 and periods between 5-20 days are apparent, as well as Kelvin waves with wavenumbers 1-6 and periods between 5-30 days. The most dominant peaks in the Kelvin wave regime lie around wavenumbers 1-2 with 15–30-day periods. They are dominant features in the lower stratosphere and provide a significant portion of the westerly momentum forcing for the QBO. This shows that equatorial stratospheric waves are abundant in the idealized simulation, even without simulating the latent heat release due to tropical cumulus convection or parameterized GWD. Therefore, the waves in SLD must have been triggered by dynamic and static instabilities or represent freely propagating normal modes.

A TEM analysis is performed to investigate the wave-mean flow interaction. It is applied along constant pressure levels in the stratosphere following the pressure-based TEM formulation in *Andrews et al.* (1983). TEM identifies four drivers for the zonal-mean zonal wind acceleration; the mean meridional advection, mean vertical advection, the divergence of the Eliassen-Palm (E-P) flux which denotes the wave-mean flow interaction, and the residual. The latter incorporates diffusion and other damping mechanisms like the effects of the radiative damping. Figure 2.3 shows the 50-month time series of the monthly-mean zonal-mean (a) zonal wind acceleration, (b-d) TEM partitioning and (e) an assessment of diffusion in a time-height cross section averaged between 2° N/S. The mean meridional advection is not shown because of its very small magnitudes that range between ± 0.03 m s^{-1} day^{-1}. The mean vertical advection (Fig. 2.3b) mostly provides a westerly acceleration during the easterly phase. This forcing contributes to the descent of the upper (easterly-to-westerly) zero wind line where the wind acceleration (Fig. 2.3a) is positive, but slows the descent of the lower (westerly-to-easterly) zero wind line where the acceleration is negative. The vertical advection mostly counteracts the effects of the E-P flux divergence (the resolved wave forcing) which was also found by *Hamilton et al.* (2001), *Giorgetta et al.* (2006) and *Xue et al.* (2012). The E-P flux divergence (Fig. 2.3c) is the most

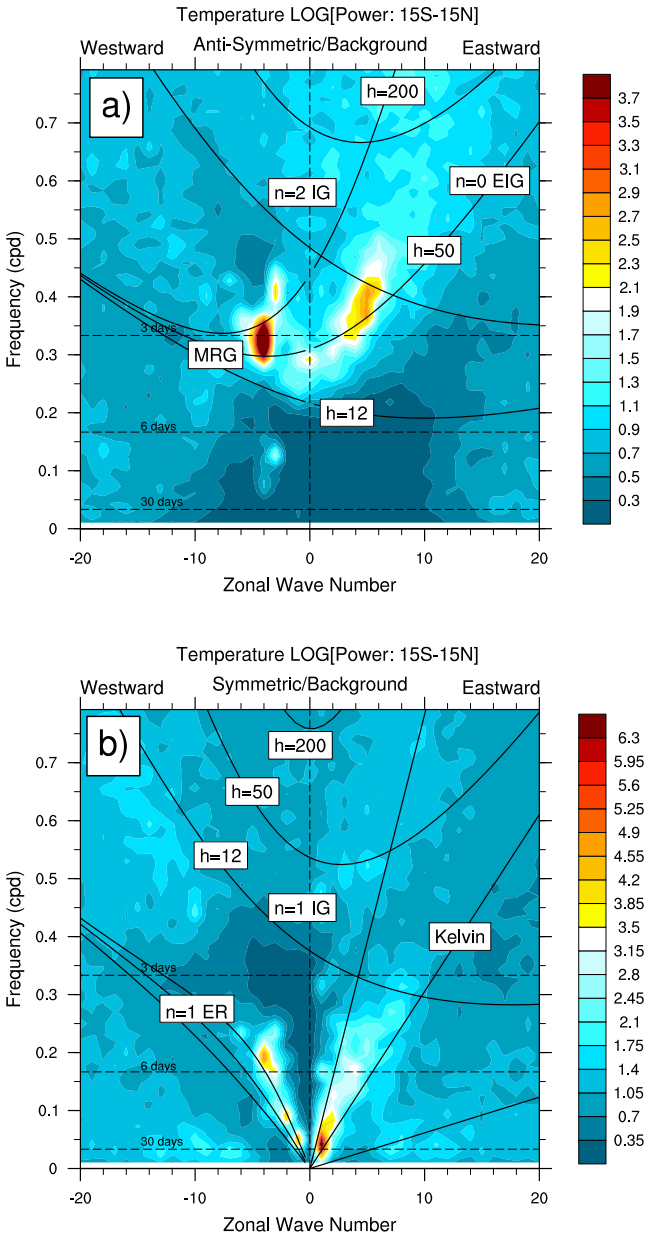

Figure 2.2: a) Anti-symmetric and b) symmetric components of the wavenumber-frequency spectra for the 22 hPa temperature, averaged between 15° N/S. The Doppler-shifted dispersion curves from shallow water theory are overlaid (with $\bar{u} = -8$ m s^{-1}).

important driver of the QBO-like oscillation which provides most of the easterly acceleration during the easterly phase and most of the westerly force during westerly phase. However, its vertical position in comparison to the wind acceleration (Fig. 2.3a) is shifted upward as it was also displayed in *Hamilton et al.* (2001). The momentum budget in the idealized simulation can thereby only be closed in the presence of a large residual (Fig. 2.3d) that mostly plays a counteracting role in comparison to the E-P flux divergence.

Figure 2.3e compares the residual to the shape of fourth-order horizontal hyper-diffusion ($-K_4\nabla^4\mathbf{v}$) at the equator with the horizontal velocity vector $\mathbf{v}$ and the hypothetical diffusion coefficient $K_4 = 5 \times 10^{15}$ m^4 s^{-1}. This coefficient corresponds to a damping time scale of 5.6 h for the maximum wavenumber which is a reasonable choice at the T63 resolution (*Jablonowski and Williamson*, 2011). The figure suggests that the implicit numerical diffusion in SLD, which mimics fourth-order hyper-diffusion, seems to capture most of the gross tendencies of the residual. A perfect match is not expected since the nonlinear aspects of the implicit diffusion are not represented, and neither the effects of the radiative HS damping (indirectly via the thermal wind relationship) nor vertical diffusion are accounted for in this linear assessment of the diffusive tendencies. The diffusion mostly counteracts the resolved wave forcing and thereby plays a considerable role in this simulation. In general, QBO simulations in GCMs have been found to be very sensitive to their diffusive properties. *Takahashi* (1999) and *Hamilton et al.* (2001) reported that they needed to lower the coefficients of the explicitly-applied fourth-order horizontal hyper-diffusion. This raises the question what the relative roles of mechanical (diffusive) versus thermal damping are in both the observed and modeled QBO, and whether the idealized SLD simulation reveals a physical or numerical effect.

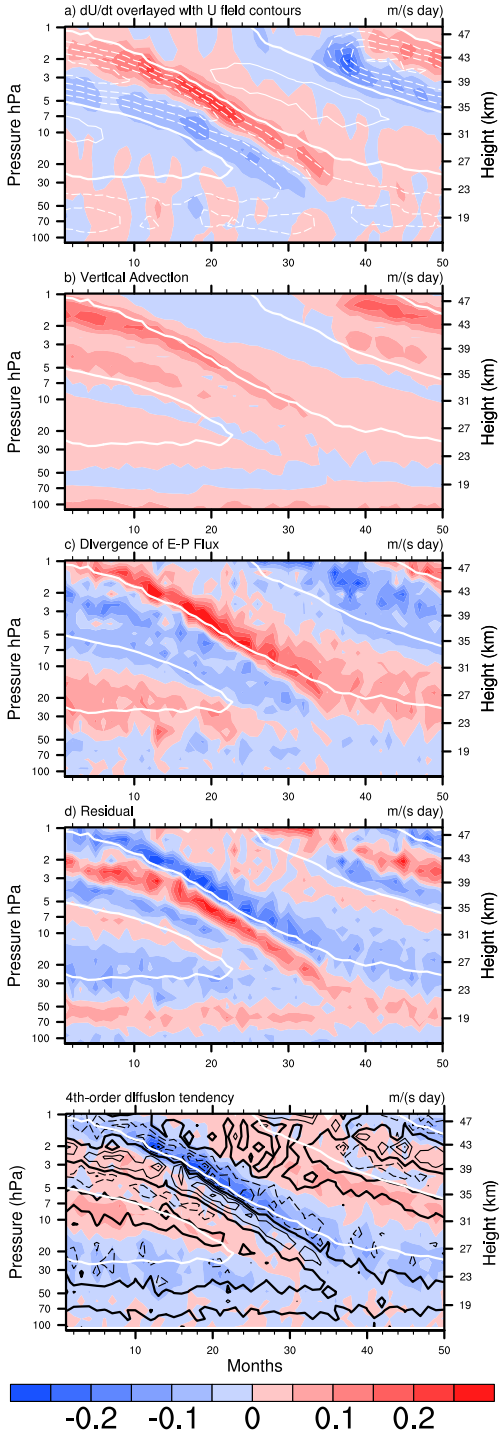

Figure 2.3: Zonal-mean monthly-mean time-height cross sections averaged between 2° N/S a) Zonal wind acceleration, b) TEM vertical advection, c) divergence of the E-P flux, d) TEM residual (continued caption next page)

Figure 2.3: e) acceleration effects of 4th-order horizontal diffusion with $K_4 = 5 \times 10^{15}$ m^4 s^{-1}. In e) the contours of the residual are overlaid in black with contour spacing 0.1 m s^{-1} day^{-1}. Overlaid white contours show the zonal-mean monthly-mean zonal wind with contour interval 8 m s^{-1} in a), only the enhanced zero wind line is shown in b)-e). All negative contours are dashed.

2.5 Conclusions

A QBO-like oscillation has been simulated in the dry CAM SLD dynamical core that was driven by the Held-Suarez forcing with additional Rayleigh friction near the model top. The QBO-like signal has an average period of 43.5 months, and occupies the equatorial domain between 50 and 1 hPa. The overall shape of the oscillation resembles observations, although the QBO-like signal is located higher up in the stratosphere and its period is longer than observed.

The wave-number frequency analysis showed that the Doppler-shifted resolved equatorially-trapped Kelvin, MRG, ER and EIG waves are abundant in the idealized simulation despite the absence of the typical wave triggering mechanisms like cumulus convection. These waves are known to be important wave drivers for the QBO. In addition, no GWD parameterization was applied. The TEM analysis showed that the divergence of the E-P flux and vertical advection are the most important drivers of the QBO-like oscillation. However, the residual is of the same order of magnitude and mostly counteracts the resolved wave forcing. It contains the effects of dissipative processes. We found that the shape of the residual closely resembles the effects of momentum diffusion in the form of a fourth-order horizontal hyper-diffusion. This suggests that the implicit numerical diffusion from the semi-Lagrangian scheme contributes considerably to the QBO-like oscillation in the idealized simulation which might shed new light on the role of diffusion in the QBO forcing.

CHAPTER III

Idealized Quasi-Biennial Oscillations in an Ensemble of Dry GCM Dynamical Cores

3.1 Introduction

Modeling the Quasi-Biennial Oscillation (QBO) in atmospheric General Circulation Models (GCMs) and understanding the QBO forcing mechanisms have been a challenge for decades. The QBO is a phenomenon in the equatorial stratosphere that occupies the region between 100-1 hPa. This region is characterized by a downward propagating zonal wind regime that periodically changes from westerlies to easterlies. On average, the observed QBO period is 28 months, but can vary substantially between 22 to 34 months. A thorough review of the QBO is provided in *Baldwin et al.* (2001).

The QBO is an important feature since it not only dominates the circulation in the tropical stratosphere but also impacts the stratosphere at high latitudes, the meridional circulation in the stratosphere (Brewer-Dobson circulation), as well as the tropospheric and mesospheric flow. For example, *Holton and Tan* (1980) showed that the 50 hPa geopotential height at high latitudes is lower in the westerly phase of the QBO as compared to the easterly phase. *Baldwin et al.* (2001) reviewed how the interaction between the QBO and the Brewer-Dobson circulation influences the mass

transportation in the stratosphere and thereby impacts the distributions of chemical constituents, like ozone, and water vapor. *Garfinkel and Hartmann* (2011a) used idealized dry model experiments with a forced QBO to discuss the impact of the QBO-induced meridional circulation on the tropospheric flow. Furthermore, it is well documented that the QBO acts a filtering mechanism for upward traveling waves (e.g. see *Yang et al.* (2011, 2012), *Krismer and Giorgetta* (2014)) and thereby modulates the wave composition in the mesosphere. Therefore, the ability of a GCM to simulate the QBO is an important model characteristic.

Takahashi (1996, 1999), *Scaife et al.* (2000, 2002), *Hamilton et al.* (2001) and *Giorgetta et al.* (2002, 2006) were among the first that simulated QBOs or QBO-like oscillations with GCMs. More recently, *Kawatani et al.* (2010), *Orr et al.* (2010), *Xue et al.* (2012), *Richter et al.* (2014a) and Chapter II also reported on successful QBO and QBO-like simulations. However, many aspects of the QBO drivers in GCMs still need to be understood since models generate QBOs for very different reasons. As e. g. pointed out by *Scinocca et al.* (2008) a spontaneously generated QBO in any two models can result from significantly different combinations of resolved equatorial waves and parameterized gravity waves. Our paper sheds light on the resolved wave forcing. In particular, it isolates the impact of the numerical discretizations and diffusion mechanisms of GCM dynamical cores on equatorial waves, and highlights their wave-mean flow interactions in the QBO region. This is accomplished via idealized dry dynamical core experiments that can expose causes and effects of the model design choices more clearly than full GCMs with physical parameterizations. Note that the phrase "dynamical core" refers to the resolved fluid flow component of GCMs as defined in *Williamson* (2007). The dynamical core most often also includes explicitly-applied dissipation or filtering processes needed for numerical stability (*Jablonowski and Williamson*, 2011).

As explained by *Lindzen and Holton* (1968) and *Holton and Lindzen* (1972) the

QBO is mainly generated and influenced by equatorial waves, with trapped-equatorial Kelvin waves providing a westerly force and mixed-Rossby gravity (MRG) waves providing an easterly force. However, the forcing provided by Kelvin waves and MRG waves is not enough to explain the QBO. Inertia-gravity waves and small-scale gravity waves also contribute to the QBO forcing (*Dunkerton*, 1997). These small-scale waves have horizontal scales of about 5-500 km and are thereby too short to be fully captured by GCMs at typical climate resolutions with grid spacings between 100-250 km (*Kim et al.*, 2003). However, these waves produce synoptic-scale body forces on the atmospheric flow when they dissipate. These processes have to be resolved or parameterized in GCMs in both the vertical and horizontal directions. High vertical resolutions with vertical grid spacings of about 600-1000 m in the stratosphere are therefore often required to simulate the QBO.

With the advancement of computing resources, small-scale gravity waves can now be modeled directly, e.g. via high horizontal and vertical resolutions in the stratosphere as in *Kawatani et al.* (2010) with $\Delta x = 60$ km and $\Delta z = 300$ m, respectively, or in the tropical-channel study by *Evan et al.* (2012) with $\Delta x = 37$ km and $\Delta z = 500$ m. Alternatively and more typical of today's GCMs, a gravity wave drag (GWD) parameterization scheme can be included as e.g. demonstrated in the middle atmosphere and QBO studies by *Scaife et al.* (2000, 2002), *Giorgetta et al.* (2002, 2006), *Naoe and Shibata* (2010), *Orr et al.* (2010), *Xue et al.* (2012), *Krismer and Giorgetta* (2014) or *Richter et al.* (2014a). These modeling studies show that small-scale gravity and intermediate-scale inertia gravity waves are important QBO drivers in GCMs, as also observed in nature (*Ern and Preusse*, 2009; *Ern et al.*, 2014; *Alexander et al.*, 2010). As a caveat though, the choice of the gravity wave drag scheme as well as the strength and launch level of the gravity wave source spectrum are highly model dependent. They significantly impact the characteristics of a QBO simulation as e.g. documented in *Giorgetta et al.* (2006), *Scinocca et al.* (2008), *Xue et al.* (2012), *Lott and Guez*

(2013), *Kim et al.* (2013) and *Schirber et al.* (2014), and can be used to empirically tune the QBO period, magnitude and vertical extent. In our paper, we avoid such complications and reveal that QBO-like oscillations are also possible in GCM dynamical cores without resolved or parameterized small-scale gravity waves at rather coarse horizontal and vertical grid spacings of $\Delta x \approx 210$ km and $\Delta z = 1.25$ km in the stratosphere.

All of the aforementioned GCM studies except Chapter II used model setups with realistic topography and comprehensive physical parameterization packages that include processes like moist convective parameterizations. In fact, it is widely believed that the primary source of tropical waves is latent heat release by either resolved-scale precipitation or parameterized deep cumulus convection. In general, it is difficult to isolate the main wave drivers in such GCM experiments, since all components of the model, such as the dynamical core and the individual physics processes, interact with each other. In Chapter II we have presented a QBO-like simulation with a dry dynamical core that was driven by a Newtonian temperature relaxation and Rayleigh friction on a flat Earth following *Held and Suarez* (1994). The current chapter extends this analysis and systematically assesses the wave generation, propagation, dissipation and forcing characteristics of stratospheric circulations in a variety of dynamical cores that are options in the Community Atmosphere Model (CAM) version 5 (*Neale et al.*, 2010). CAM5 has been jointly developed by the National Center of Atmospheric Research (NCAR) and various U.S. Department of Energy Laboratories. The purpose of this paper is to examine the intrinsic ability of CAM's four dynamical cores to simulate QBO-like oscillations when driven by the *Held and Suarez* (1994) forcing. As mentioned above, such an investigation sheds light on the role of the numerical schemes, their dissipation mechanisms and resolved wave dynamics in the simulations. Of course, we do not expect to fully capture the observed wave spectrum in such idealized model experiments as convectively generated waves are certainly an

important characteristic of the atmosphere (*Kiladis et al.*, 2009). Rather the investigation is a process study that reveals the sensitive link between QBO-like oscillations and the dissipation in dynamical cores that has not been documented before.

The chapter is structured as follows. Chapter 3.2 provides brief descriptions of the CAM5 dynamical cores and describes the simulation setup. Chapter 3.3 documents the circulation results and characteristics of the stratospheric flows. Chapter 3.4 evaluates the wave forcing using the Transformed Eulerian Mean (TEM) analysis and furthermore sheds light on the Brewer-Dobson circulations and diffusion properties of the dynamical cores. Chapter 3.5 examines potential wave generation mechanisms and instability indicators, while Chapter 3.6 uses wavenumber-frequency analysis to analyze resolved equatorial waves. Chapter 3.7 presents a brief sensitivity analysis. The summary and outlook are provided in Chapter 3.8.

3.2 Model descriptions and experimental design

3.2.1 The CAM5 dynamical cores

We utilize the four CAM5.0 dynamical cores which are the spectral transform semi-Lagrangian (SLD), Finite-Volume (FV), spectral transform Eulerian (EUL) and Spectral Element (SE) model. The latter dynamical core has become CAM's new default in version 5.3. The numerical design choices are documented in *Neale et al.* (2010). Here, we only characterize them very briefly. All models are run with identical 55 vertical levels with a model top at 0.1 hPa using a hybrid $\sigma - p$ (called η) vertical coordinate with variable vertical grid spacing (further explained in Appendix). It ranges from $\Delta z \approx 0.2$ km near the surface and increases with height in the troposphere. We select a constant $\Delta z = 1.25$ km in the stratosphere between 100-3 hPa, and slowly stretch (5% per level) the spacing above 3 hPa to reach ≈ 2 km at the model top. All model levels above 112 hPa are pure pressure levels which

Table 3.1: Horizontal resolutions, approximate equatorial grid spacings Δx (in km), dynamics time steps Δt (in s) and diffusion mechanisms with coefficients for each dynamical core. T stands for triangular truncation, ne16np4 denotes that each cubed-sphere face is divided into 16×16 elements with np=4 collocation points in each horizontal direction.

Dycore	Resol.	Δx	Δt	Diffusion	Diffusion coefficient
SLD	T63	208	2700	Implicit	–
EUL	T63	208	720	4th-order hyper-diffusion	5×10^{15} m^4 s^{-1}
FV	2°×2°	222	360	Implicit	
				2nd-order divergence damping	*Whitehead et al.* (2011)
SE	ne16np4	208	540	4th-order hyper-diffusion	5×10^{15} m^4 s^{-1}

avoids vertical interpolations in the TEM analysis along isobars. The horizontal grid spacing for all dynamical cores is about 2°×2° or 210–220 km in equatorial regions. The model configurations, including their dynamics time steps and dominant diffusion mechanisms, are documented in Table 3.1. The associated physics time steps are 2700 s (SLD), 3600 s (FV) and 720 s (EUL) and 2700 s (SE). All dynamical cores are built upon a hydrostatic and shallow-atmosphere equation set (the "primitive equations").

The SLD dynamical core (dycore) is a two-time-level, semi-implicit semi-Lagrangian spectral transform model, and utilizes a quadratic Gaussian transform grid with 192×96 grid points. The triangular truncation is T63 corresponding a 208 km grid spacing around the equator. The SLD dycore is used without explicitly-applied horizontal diffusion. Its implicit numerical diffusion due to the semi-Lagrangian interpolations provides enough dissipation to avoid a buildup of kinetic energy near the grid scale. The damping effect of the cubic SLD interpolations mimics 4th-order horizontal hyper-diffusion (*McCalpin*, 1988).

The FV dycore uses a grid-point-based finite-volume discretization with an explicit time-stepping scheme and utilizes a regular 2°×2° latitude-longitude grid. It is built upon a 2D shallow water approach in the horizontal (*Lin and Rood*, 1996)

and applies a vertical remapping approach to represent the vertical transport (*Lin*, 2004). FV's primary diffusion mechanisms are implicit numerical diffusion via limiters and explicitly-applied 2nd-order horizontal divergence damping that is explained in *Whitehead et al.* (2011) and *Jablonowski and Williamson* (2011).

The EUL dycore is a three-time-level, semi-implicit Eulerian spectral transform model in vorticity-divergence form and, as SLD, utilizes a T63 quadratic Gaussian transform grid. The EUL dycore is run with explicitly-applied, linear, 4th-order horizontal hyper-diffusion (see also Table 3.1) which is needed for numerical stability.

The SE dycore, also known as High-Order Method Modeling Environment (High-Order Method Modeling Environment (HOMME)), is based on a continuous Galerkin spectral finite element method and has been designed for fully unstructured quadrilateral meshes (*Taylor and Fournier*, 2010; *Dennis et al.*, 2012). In particular, the cubed-sphere grid is used here. SE employs an explicit Runge-Kutta time-stepping scheme. It is run at an ne16np4 resolution which is approximately equivalent to a $1.875^\circ \times 1.875^\circ$ grid. As EUL, the SE dycore uses a linear 4th-order horizontal hyper-diffusion mechanism with the identical diffusion coefficient. This diffusion coefficient is used for both the vorticity and divergence in SE dynamical core. None of the four dynamical cores applies a total energy fixer. Concerning the vertical discretization, EUL SLD and SE use a finite-difference type of discretization method, whereas FV is built upon the floating Lagrangian approach, with periodic remaps. A more detailed description of the dynamical cores and their dissipation mechanisms is provided in Appendix A.

3.2.2 Experimental setup

The idealized CAM5 simulations utilize the Held and Suarez (HS) forcing that replaces the whole CAM5 physics package. No moisture, topography or seasonal cycles are included. The HS forcing (*Held and Suarez*, 1994) consists of a Newto-

nian relaxation of the temperature field throughout the whole atmosphere towards an analytically-prescribed equilibrium state with isothermal stratosphere, and Rayleigh damping of low-level winds. These processes mimic the effects of radiation and boundary layer friction. Additionally, we apply Rayleigh friction ($-K_r u$) to the zonal wind field in a sponge layer above 1 hPa up to the model top at 0.1 hPa to dissipate upward traveling waves in this region. Eight model levels lie in this sponge zone. Following *Boville* (1986) the expression for the pressure-dependent Rayleigh friction coefficient is given by $K_r = k_0 * (1 + tanh((z - z_0)/H_0))$. The damping coefficient k_0 is set to 1/3 day^{-1}, the log-pressure height is $z = h_0 \ln(p_0/p)$, p symbolizes pressure, the reference pressure p_0 is set to 1000 hPa, and h_0 stands for a scale height of 7 km. In addition, the parameter for the model top z_0 is set to 61 km and the scale factor H_0 is 7.7 km. This leads to the damping time scales $1/K_r$ of about 41 days at 1 hPa and 2 days at the model top. The HS damping time scale of the Newtonian temperature relaxation is 40 days above $\approx$ 700 hPa. The same experimental setup was also used in Chapter II who already highlighted some characteristics of the QBO-like oscillations in the SLD model.

All experiments provide 30-day mean data (called monthly-mean hereafter) for 20-40 model years. One simulation year corresponds to 360 model days. In addition, 6-hourly instantaneous data are collected for at least 30 months. This high-frequency output is utilized to perform TEM, instability and wavenumber-frequency analyses. We either use an observed (data-assimilated) initial state that has been interpolated to zero topography, or spun-up initial states from an earlier Held-Suarez SLD model simulation with an established QBO-like stratospheric oscillation. Such initial states already contain a QBO wind shear pattern. However, we also found that the SLD model spins up a QBO-like oscillation from a slightly perturbed initial state at rest with isothermal temperature. It suggests that the initial state might be of secondary importance for our simulations once a spin-up period has passed.

3.3 Intercomparison of the statospheric circulations

We now compare the flow fields of the four CAM5 dynamical cores with special focus on the stratosphere. Figure 3.1 shows the 20-40 year time series of their monthly-mean zonal-mean zonal winds which are averaged between $\pm 2^{\circ}$. The stratospheric circulations have very different characteristics, despite the identical experimental setups. The SLD dycore in Fig. 3.1a shows spontaneously generated QBO-like oscillations with an average period of about 3.6 years, as already shown in Chapter II. The oscillation occupies the region between 1-50 hPa.

The FV dycore (Fig. 3.1b) cannot maintain the QBO oscillation that was present in the initial data file. The initial wind shear is diffused, and from year 6 onwards the vertical domain is occupied by two steady jets. A westerly jet lies between 3-30 hPa with a maximum zonal wind velocity of $\sim$ 10 m s^{-1}. An easterly jet is located below 30 hPa with a zonal wind peak of approximately -15 to -20 m s^{-1}.

The EUL dycore (Fig. 3.1c) shows zonal wind oscillations with a very long period which seems to be greater than 13 years. The downward propagation speed of the westerly wind regime is not as regular as the descent in the SLD simulation. The westerly wind regime slowly travels downward between 0.3 hPa to 7 hPa, and then "quickly" descends to around 20 hPa. The newly formed easterly regimes near the model top start descending relatively quickly between 0.5-7 hPa before their descents slow considerably. This easterly branch propagates down to 10 hPa. It is unable to fully break through the westerly regime located between 10-20 hPa and cannot connect to the easterly jet below 20 hPa. Most likely, the easterly wave forcing is insufficient. As a consequence, the magnitude of the westerly wind oscillates in this "lower" QBO domain (10-20 hPa), but never turns easterly.

The SE dycore (Fig. 3.1d) has very similar characteristics as EUL, with a fast descending westerly regime between 7 to 20 hPa. The figure implies that SE might have a comparable or even longer QBO period than EUL. However, the 40-year

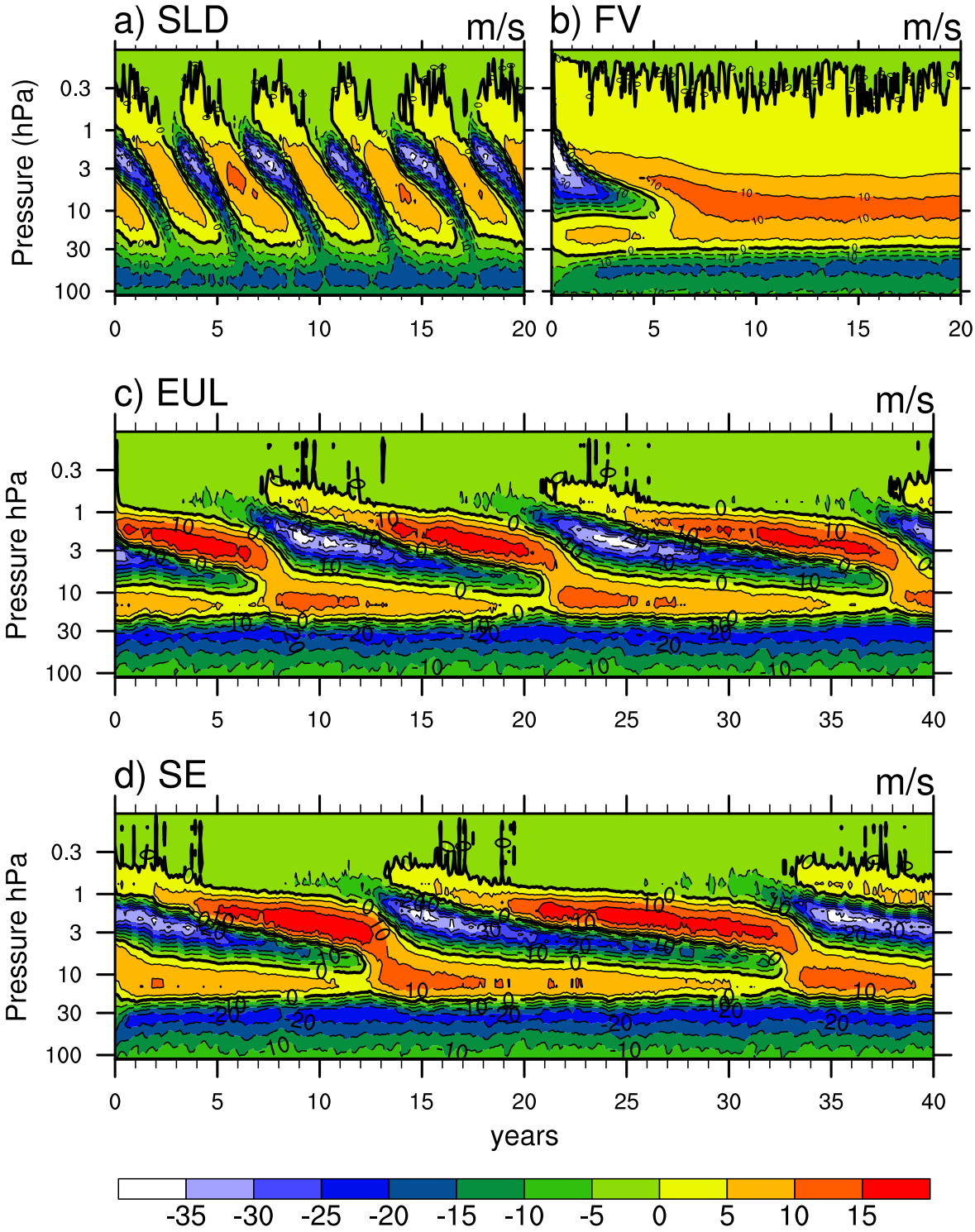

Figure 3.1: Time-pressure cross sections of the monthly-mean zonal-mean zonal wind averaged between ±2° for a) SLD, b) FV, c) EUL and d) SE. The zero wind line is enhanced.

EUL and SE simulations are too short to determine the period with certainty. The resemblance between EUL and SE is striking and suggests that they might have comparable wave generation, propagation and absorption mechanisms. The EUL and SE QBO-like patterns also resemble the QBO simulations by *Horinouchi and Yoden* (1998), *Scaife et al.* (2000) (their Fig. 1, middle panel) and *Scinocca et al.* (2008) (their Fig. 6f). These groups similarly observed that their easterly jets could not break through the westerly regimes in the lower QBO domain. In contrast to their studies though, the QBO patterns in EUL and SE already stall higher up at around 30 hPa and fail to descend to the lower stratosphere (70-100 hPa). *Scaife et al.* (2002) (their Fig. 13) showed that enhanced horizontal diffusion can cause the descending westerlies to stall early. In addition, *Giorgetta et al.* (2006) found that their QBO stalled at higher altitudes as soon as their vertical grid spacing was increased from 700 m to 1 km and 1.4 km. The fact that the QBO, and especially its westerly branch, does not propagate deep enough into the lower stratosphere is a common problem in GCM simulations, and was also shown in e.g. *Kawatani et al.* (2011), *Xue et al.* (2012) and *Evan et al.* (2012). It suggests that the wave forcing is insufficient to bring the QBO down to the tropical tropopause (100 hPa) where the largest atmospheric densities occur in the QBO region. Other aspects, like the strength of the updrafts in the Brewer-Dobson circulation, that oppose the QBO descent, also play a role and are discussed further in Chapters 3.4 and 3.4.2.

We note that the positions of the low-lying equatorial easterly jets in Fig. 3.1 are very different in EUL, SE and FV in comparison to SLD, despite the identical HS forcing. The easterly jets in EUL, SE and FV reach their peak magnitude at around 40-50 hPa, whereas the SLD jet lies lower at around 70-80 hPa. Since easterly waves get filtered in easterly jets, this difference is likely to contribute to the differences in the QBO-like oscillations higher up. In general, equatorial shear zones are a consequence of vertical wave propagation as explained in *Dunkerton* (2000). Once formed, the

shear zones concentrate the breaking or absorption of a broad spectrum of waves into a shallow layer, which strengthens the shear and accelerates the flow field.

Overall all QBO-like patterns in the HS experiments (SLD, EUL, SE) lie too high in the stratosphere in comparison to observations (1-100 hPa, e.g. see *Naujokat* (1986)) or reanalysis data (*Pawson and Fiorino*, 1998; *Pascoe et al.*, 2005). In addition, all QBO periods are too long which is not surprising given the idealized HS setup without moist convection as a typical wave trigger. However, the minimum/maximum zonal wind peaks are rather realistic and range between -35 m s^{-1} and 10-15 m s^{-1}. This phase asymmetry arises internally. It indicates that the dynamical cores generate waves that are asymmetric between the westerly and easterly phase speeds, as in observations. However, we are not expecting a full match with the observations, since the model set-up is purely idealistic. There are also internal variations in the length and magnitude of each QBO cycle, as it is typical for the QBO. For simplicity, we refer to the QBO-like oscillations in the HS experiments as "QBOs" from here on.

Figure 3.2 shows the 4.9 hPa time-latitude cross sections of the monthly-mean zonal-mean zonal wind for all dynamical cores. This model level is closest to the maximum wind amplitude in the HS simulations and lies higher than the observed peak ($\sim$ 20 hPa). The QBO in SLD, EUL and SE is confined to the tropical region between $\pm 35^{\circ}$ with a slightly too narrow latitudinal width of the westerly phase ($\pm 10^{\circ}$) when compared to observations (*Pawson and Fiorino*, 1998; *Giorgetta et al.*, 2006). The onset of the westerly phase occurs first at the equator whereas the onset of the easterly phase is spread out more evenly over the equatorial region, as in observations. The strong easterlies ($u < -15$ m s^{-1}) in the EUL and SE simulations are narrower than the strong easterlies in the SLD simulation. We also observe that the approximate duration of the westerlies only varies by a factor of two between SLD (2 years) and EUL/SE (3.5-4 years), whereas the duration of the easterlies is very different (1.5-2 years versus 13-16 years). In the FV simulation, a westerly jet

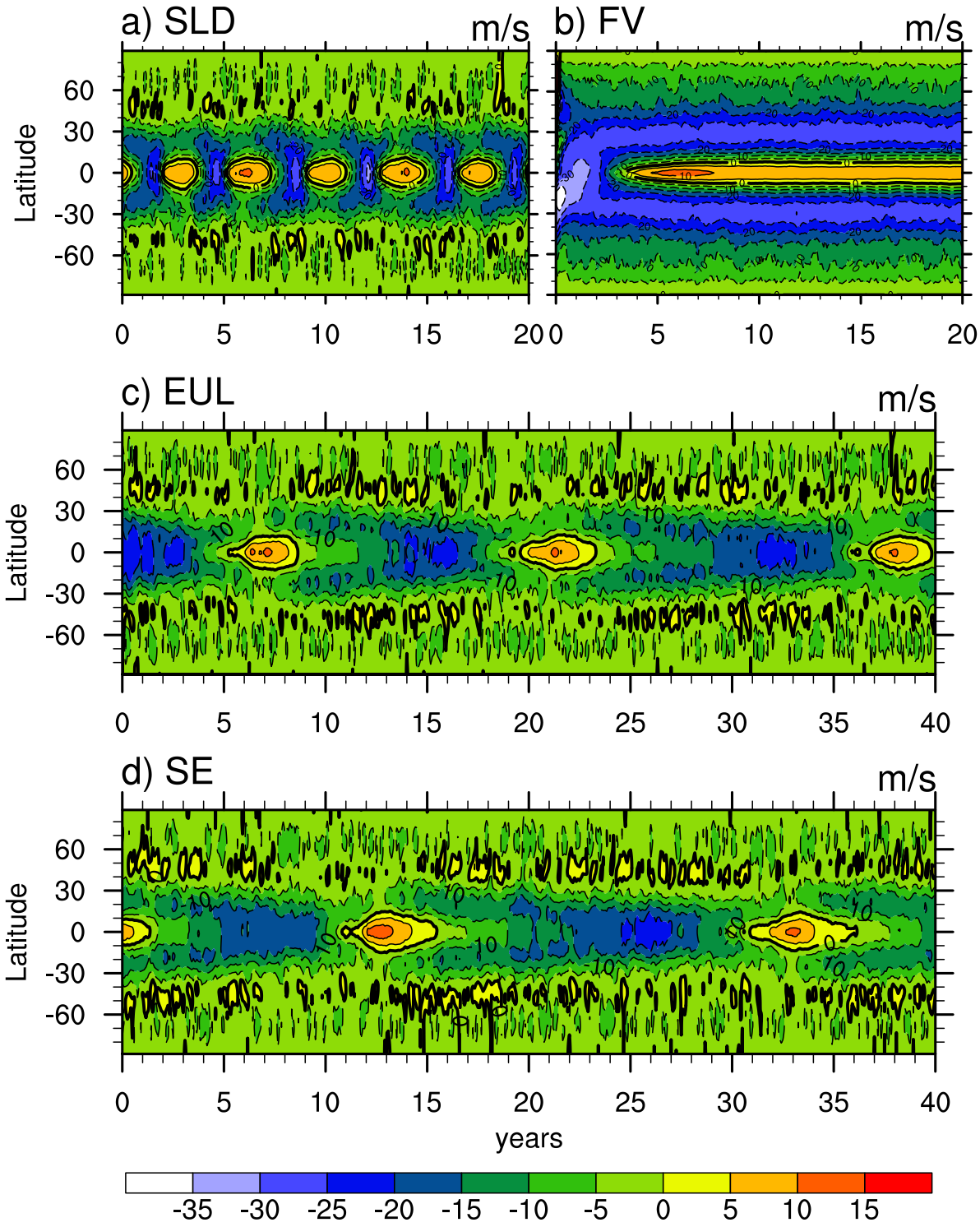

Figure 3.2: Time-latitude cross sections of the monthly-mean zonal-mean zonal wind at 4.9 hPa for a) SLD, b) FV, c) EUL and d) SE. The zero wind line is enhanced.

occupies the tropical region between ±10°, and two easterly jets are located in the subtropical/midlatitudinal region centered around ±30° (Fig. 3.2b).

Figure 3.3 shows the pressure-latitude cross sections of the monthly-mean zonal-mean zonal wind field for a single month. In the troposphere, two westerly jets of identical strengths appear in the midlatitudes in all four dynamical cores, as it is typical for the HS test. The positions of the tropopause, as indicated by the overlaid blue contours, are also very similar. It suggests that the mean tropospheric circulations are comparable in all four models. In the equatorial stratosphere, we observe vertically stacked westerlies and easterlies in the QBO simulations with SLD, EUL and SE , surrounded by weak easterlies at higher latitudes. The stratospheric flow in FV (Fig. 3.3b) is very different and dominated by two strong easterly jets in midlatitudes. These jets are closely connected to warmer polar temperatures in the region between 100-3 hPa (not shown) when compared to the other dycores. The consequently enhanced temperature gradients between the relatively warm polar and cold equatorial stratosphere in the FV dycore cut off the westerly tropospheric jets at a low location in the stratosphere at around 50 hPa, and cause the strong easterlies via the thermal wind relationship. This again exemplifies that the general circulation in the stratosphere reacts very differently to the identical HS forcing, which has not been documented for the stratosphere before. Note that the presence of the easterlies at higher latitudes greatly hinders upward-traveling midlatitudinal Rossby waves from entering the equatorial stratosphere, so that their contributions to the QBOs in SLD, EUL and SE are presumably small. However, Rossby waves are capable of propagating through weak easterlies. This opens up the possibility that laterally-propagating midlatitudinal Rossby waves might impact the QBO region above 30 hPa, where the easterlies are generally weak in these three models and lie around -5 and -7 m s^{-1}.

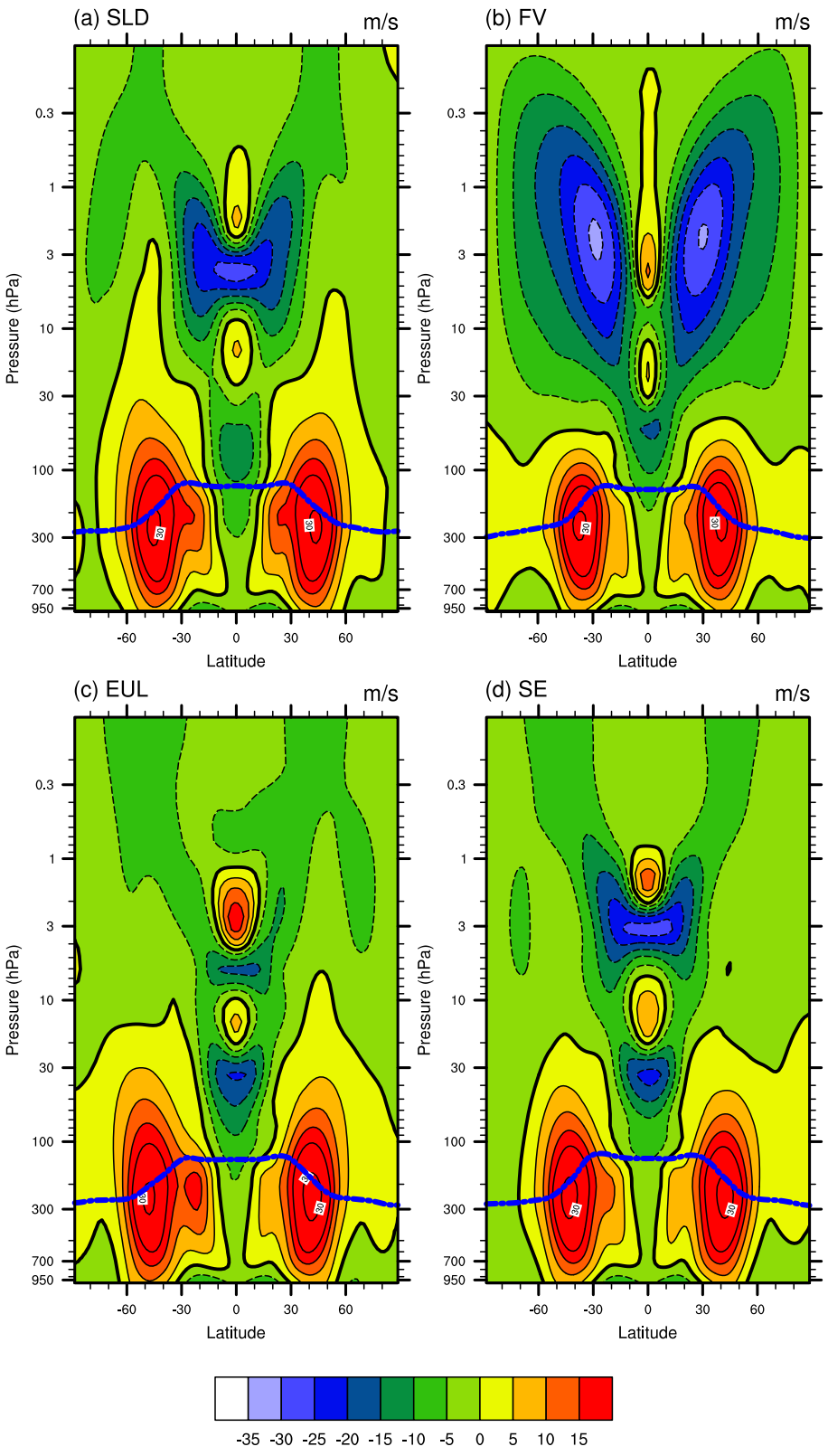

Figure 3.3: Pressure-latitude cross sections of the monthly-mean zonal-mean zonal wind for a) SLD, b) FV, c) EUL and d) SE. A single month is depicted. The blue line indicates the position of the tropopause, the zero wind line is enhanced.

3.4 The forcing of the QBO

3.4.1 Transformed Eulerian Mean (TEM) analysis

In order to understand the zonal wind forcing mechanisms in the dynamical cores we utilize 6-hourly instantaneous data and apply a Transformed Eulerian Mean analysis. The TEM analysis decomposes the zonal wind acceleration into four components shown in Eq. (3.1). These are the mean meridional advection and mean vertical advection by the residual circulation, the resolved wave-mean flow interaction expressed by the divergence of the Eliassen-Palm (E-P) flux vector, and the residual X. The latter captures the forcing by numerical and explicitly-added diffusion, as well as the impact of the HS temperature relaxation on the zonal wind. The TEM analysis is applied along constant pressure levels upwards of 112 hPa following *Andrews et al.* (1983). The zonally-averaged zonal momentum equation is given by

$$\frac{\partial \overline{u}}{\partial t} = \overline{v}^* \left[f - \frac{1}{a\,\cos\phi} \frac{\partial}{\partial \phi} (\overline{u}\,\cos\phi) \right] - \overline{\omega}^* \frac{\partial \overline{u}}{\partial p} + \frac{1}{a\,\cos\phi} \left[\frac{1}{a\,\cos\phi} \frac{\partial}{\partial \phi} (F_\phi \cos\phi) + \frac{\partial}{\partial p} F_p \right] + X. \tag{3.1}$$

The overbar symbolizes the zonal-mean, u indicates the zonal wind, t is time, p denotes pressure, f stands for the Coriolis parameter, a indicates the Earth's radius, ϕ is the latitude, and (F_ϕ, F_p) expresses the components of the Eliassen-Palm flux vector in pressure coordinates. They are defined by

$$F_\phi = a\,\cos\phi \left(\frac{\overline{v'\Theta'}}{\partial\overline{\Theta}/\partial p} \frac{\partial \overline{u}}{\partial p} - \overline{u'v'} \right) \tag{3.2}$$

$$F_p = a\,\cos\phi \left[\frac{\overline{v'\Theta'}}{\partial\overline{\Theta}/\partial p} \Big(f - \frac{1}{a\,\cos\phi} \frac{\partial}{\partial \phi} (\overline{u}\cos\phi) \Big) - \overline{u'\omega'} \right] \tag{3.3}$$

where Θ is the potential temperature, v and ω denote the meridional and vertical pressure velocities, respectively, and the prime stands for the perturbation from a zonal-mean. (v^*, ω^*) are the mean meridional and vertical pressure velocities of the

residual circulation, defined by

$$\overline{v}^* = \overline{v} - \frac{\partial}{\partial p}\left(\frac{\overline{v'\Theta'}}{\partial\overline{\Theta}/\partial p}\right) \tag{3.4}$$

$$\overline{\omega}^* = \overline{\omega} + \frac{1}{a\,\cos\phi}\frac{\partial}{\partial\phi}\left(\cos\phi\,\frac{(\overline{v'\Theta'})}{\partial\overline{\Theta}/\partial p}\right). \tag{3.5}$$

Analogous to the 50-month TEM-SLD analysis in Chapter II Fig. 2.3. Fig.3.4 shows the time-pressure cross sections of the TEM analysis for the EUL simulation. The analysis is based on 100 months of 6-hourly data from year 20 onwards. This time period captures the "fast" descent of the westerly QBO branch in the region 7-20 hPa and the initial descent of the easterly jet near 1 hPa, as seen in Fig. 3.1. It approximately covers more than half of the EUL-QBO cycle and is representative of the forcing signatures during a full period. Figure 3.4 shows the time series of the monthly-mean zonal-mean (a) zonal wind acceleration, (b) mean vertical advection, (c) E-P flux divergence which depicts the resolved wave forcing, and (d) residual X (see Eq. (3.1)). The mean meridional advection by the residual circulation is not shown because of its small magnitudes between ± 0.03 m s^{-1} day^{-1}. All of these panels are overlaid by contours of the monthly-mean zonal-mean zonal wind (in white). During the easterly phase (upper QBO branch between $\approx 1-7$ hPa), the mean vertical advection (Fig. 3.4b) almost exclusively provides a westerly acceleration, whereas the E-P flux divergence (Fig. 3.4c) provides most of the easterly acceleration. In addition, the E-P flux divergence supplies a westerly forcing in the two westerly shear zones ($\partial u/\partial z > 0$), especially around the zero wind lines where easterlies transition to westerlies. The E-P flux divergence is clearly the main driver of the QBO. The mean vertical advection mostly counteracts the E-P flux divergence except near the zero wind lines in the westerly shear zones, which was also shown in the QBO-TEM analyses by *Hamilton et al.* (2001), *Giorgetta et al.* (2006), *Kawatani et al.* (2011) or *Xue et al.* (2012). In order to close the zonal momentum budget in EUL, a strong

residual term remains (Fig. 3.4d). It opposes most of the forcing by the resolved waves (Fig. 3.4c) with similar magnitudes. This residual is of special interest and therefore further analyzed in Chapters 3.4 and 3.4.3.

Overall, the TEM analysis for EUL shows similar results as the TEM-SLD analysis in Chapter II (Fig. 2.3). An interesting observation is that the peak values of the monthly-mean zonal-mean E-P flux divergence, vertical advection and the residual term are about 50% higher in EUL than in SLD, suggesting stronger wave activities in EUL. However, the resulting zonal wind acceleration in EUL (Fig. 3.4a) is much weaker than the acceleration in SLD (Fig. 2.3a in Chapter II), due to the very strong cancellation effect between the TEM components. The TEM analysis for SE shares very similar characteristics with the EUL simulation and is therefore not shown. As mentioned above, it implies that EUL and SE have almost identical wave generation, propagation and dissipation properties despite their very different numerical designs and computational grids.

The TEM analysis for the FV simulation (applied during the steady-state period) exhibits much weaker accelerations when compared to the EUL simulation, and is therefore only briefly described here. The monthly-mean zonal-mean E-P flux divergence in FV has a maximum value of ≈ 0.15 m s^{-1} day^{-1} around the level where the background wind speed is 0 m s^{-1} (at about 30 hPa, see Fig. 3.1b). This position coincides with the position of the peak values of the monthly-mean zonal-mean residual terms (around -0.15 m s^{-1} day^{-1}). The mean vertical advection term has a range around ± 0.05 m s^{-1} day^{-1}, and the mean meridional advection by the residual circulation is even lower. The resulting monthly-mean zonal-mean zonal wind acceleration in FV is very weak and just big enough to maintain the steady stratospheric jets. The TEM analyses suggest that the resolved wave activity in FV is significantly lower in comparison to SLD, EUL and SE, which is a possible, but not necessarily the only, cause for the absence of the QBO oscillation in the idealized FV simulation

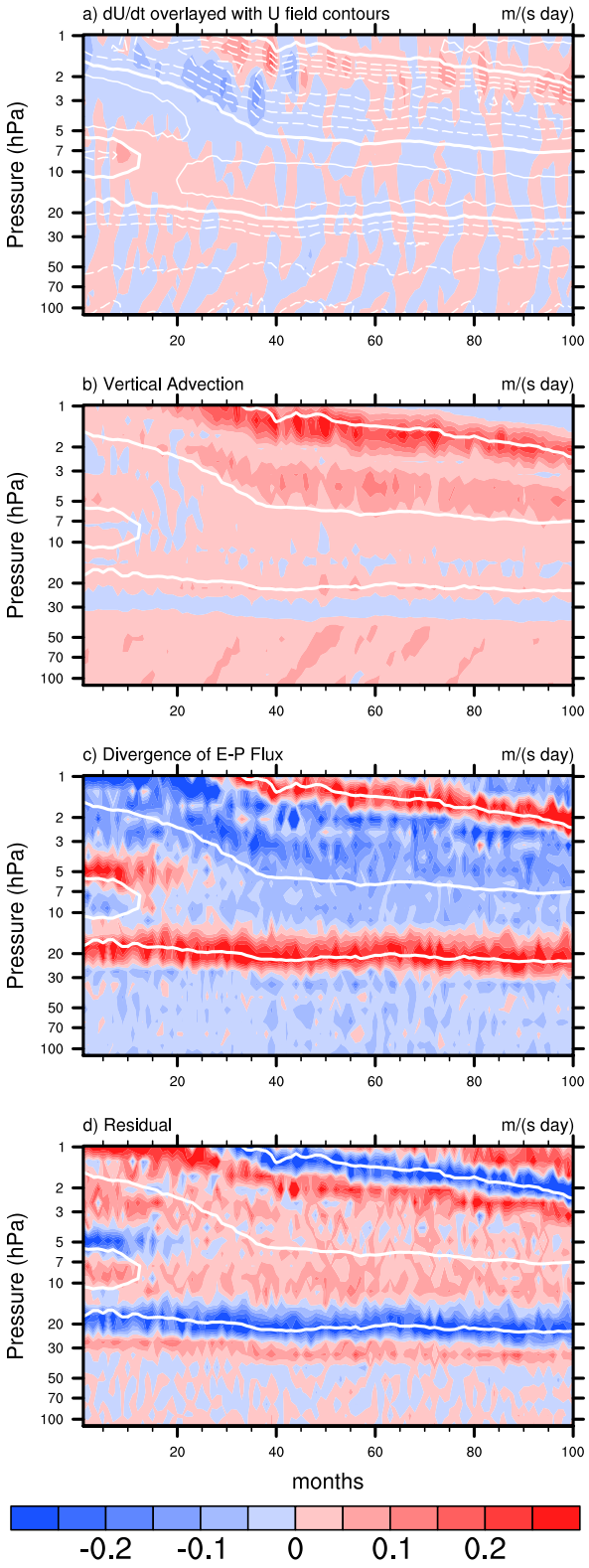

Figure 3.4: Monthly-mean zonal-mean time-pressure cross sections of the TEM components in EUL, averaged between $\pm 2^\circ$ a) Zonal wind acceleration, b) mean vertical advection, c) E-P flux divergence and d) residual X. (caption continued next page)

Figure 3.4: The plots are overlaid by the monthly-mean zonal-mean zonal wind (white contour) with contour spacing 8 m s^{-1}, solid lines are positive, dashed lines are negative. In b)-d) only the enhanced zero wind contour is shown.

shown here. The wave activity in all models is analyzed in-depth in Chapter 3.6.

3.4.2 Residual circulation

As briefly mentioned in Chapter 3.3, the descent of the QBO phases is opposed by the mean ascent in the equatorial stratosphere that is due to the Brewer-Dobson Circulation (BDC). This was e.g. discussed by *Dunkerton* (1997) who argued that the vertical momentum fluxes of the observed upward traveling Kelvin and MRG waves are insufficient to drive the observed QBO cycle, and that small-scale gravity waves must contribute to the QBO forcing to sustain the speed of the QBO descent against the mean equatorial upwelling. The impact of the mean upwelling on the QBO period and its vertical extent was also clearly demonstrated by *Kawatani et al.* (2011, 2012). They showed that increased equatorial upwelling in climate-change simulations contributes to a slowdown of the QBO descent and the stalling of the westerlies higher up in the QBO domain.

The ascent due to the Brewer-Dobson circulation can be assessed via the mean residual vertical pressure velocity $\overline{\omega}^*$ (Eq. 3.5). In particular, $\overline{\omega}^*$ just above the tropical tropopause ($\approx$ 100 hPa) can be used to assess the mass flux entering the stratosphere. In or near the QBO domain, the mean BDC ascent is furthermore modulated by the locally induced secondary meridional circulation (*Choi et al.*, 2002; *Flury et al.*, 2013). The latter is responsible for maintaining the thermal wind balance between the QBO signals in the temperature and zonal wind fields. In easterly shear zones ($\partial u/\partial z < 0$) the secondary meridional circulation triggers equatorial upwelling ($\overline{\omega} < 0$) and therefore opposes the descent of the QBO. In westerly shear zones ($\partial u/\partial z > 0$) the secondary meridional circulation triggers equatorial downdrafts

($\overline{\omega} > 0$), thereby reducing the BDC opposition to the descending QBO.

As an example, Fig. 3.5 shows the close correspondence between the equatorial zonal wind (in blue, left axis) and the vertical pressure velocity (in red, right axis) in the lower QBO domain at 27 hPa in SLD. This location lies slightly below or near SLD's stalling westerly QBO branches. Therefore, the monthly-mean zonal-mean zonal wind oscillates between $\approx$ 0 m s^{-1} to about -16 m s^{-1} over the depicted 20-year time series. The corresponding vertical wind shear is mostly westerly as seen in Fig. 3.1a, except during the periods when the easterly QBO branches break through and connect to the steady easterly jet below 50 hPa. These periods exhibit brief and relatively weak easterly vertical wind shears. Figure 3.5 demonstrates that the vertical pressure velocity exactly follows the zonal wind and its vertical wind shear pattern as also shown in *Flury et al.* (2013). The westerly wind shear phases (before the zonal wind dips down to its minimum) are characterized by strong downdrafts ($\overline{\omega} > 0$), whereas the weak easterly wind shear phases let the vertical velocity tend towards zero or mild updrafts. However, the vertical velocity reversal from downdrafts to updrafts is not present in all QBO cycles at 27 hPa. Locations higher up show the reversal more clearly, but we picked 27 hPa in order to re-use this location for the BDC intercomparison in Fig. 3.6.

Figure 3.6 depicts the area-weighted zonal-mean residual velocities $\overline{\omega}^* \times \cos\phi$ of all four dynamical cores, which can be interpreted as proxies for the strength of the overturning meridional mass circulation. The figure shows the latitudinal profiles of 30-month-means near the equatorial tropopause at 94 hPa and in (or slightly below) the QBO domains at 27 hPa. Since negative $\overline{\omega}^*$ indicates upward motion, the y-axis is reversed to allow for an easier interpretation. The 30-month averaging periods cover the years 7.1-9.6 (SLD), 10-12.5 (FV), 19.75-22.25 (EUL) and 12.25-14.75 (SE). At 94 hPa below the QBO domains, the effect of the secondary meridional circulation is negligible, and all models show the mean ascent of the BDC at the equator. The

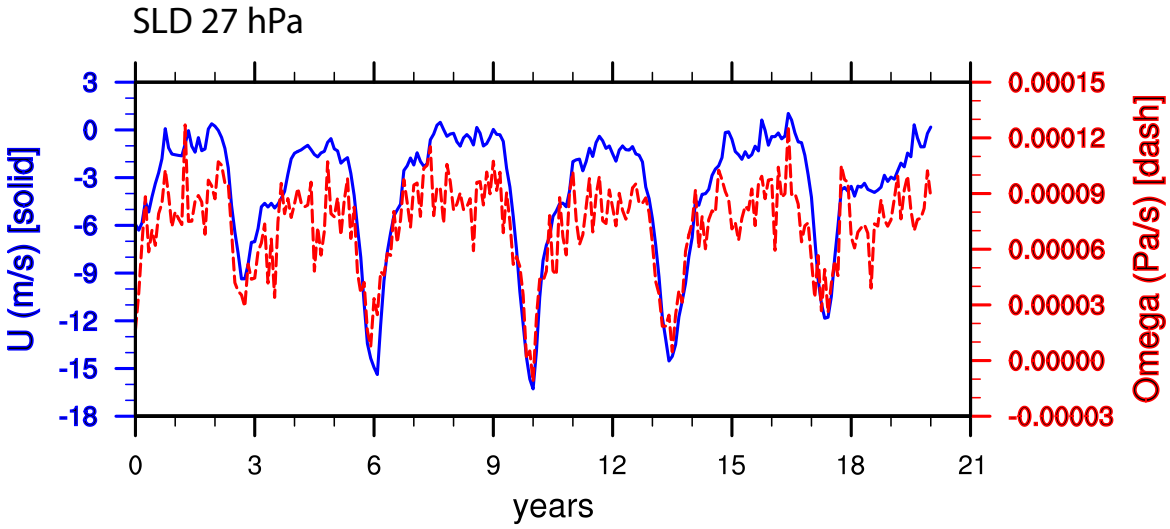

Figure 3.5: Time series of the monthly-mean zonal-mean zonal wind $\overline{u}$ (solid blue, left axis) and vertical pressure velocity $\overline{\omega}$ (dashed red, right axis) averaged between $\pm 2^\circ$ for the SLD dynamical core at 27 hPa.

magnitudes of $\overline{\omega}^* \times \cos\phi$ in SLD, EUL and SE are very similar. However, at 27 hPa the averaging periods are dominated by westerly shear zones that are related to the QBO (Fig. 3.1). This triggers downdrafts which overlay the mean ascent of the BDC at the equator. In SLD the strong descent of the secondary meridional circulation even reverses the direction of the equatorial BDC, whereas it only creates local minima of the tropical BDC ascent in EUL and SE (Fig. 3.6b). In summary, the downward propagation of the QBO in EUL and SE is hindered by the mean upwelling of the BDC, whereas SLD's downward propagating QBO is sped up since the BDC reverses its sign at the equator. This is a contributing factor to the very long QBO periods in EUL and SE in comparison to SLD.

We note that the peak equatorial amplitudes of the mean residual vertical pressure velocity $\overline{\omega}^*$ at 94 and 27 hPa in Fig. 3.6 translate to equatorial velocities of about $\overline{w}^* \approx 0.27$ mm s^{-1} and ± 0.08 mm s^{-1}, respectively. These estimates utilize the approximate relationship $\overline{w}^* \approx -H\overline{\omega}^* p^{-1}$ with an assumed stratospheric scale height of $H = 5.85$ km that corresponds to the HS equilibrium temperature of 200 K.

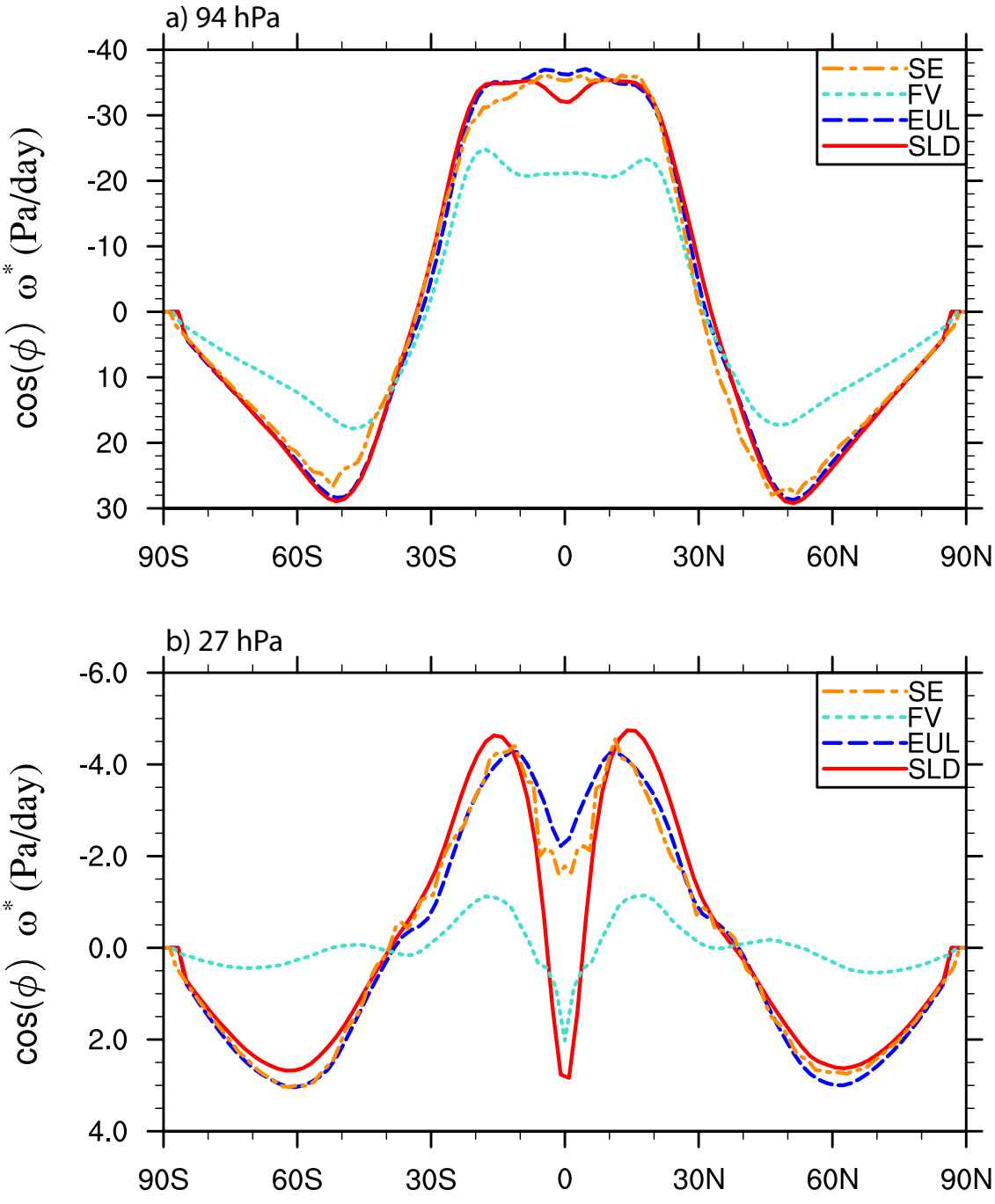

Figure 3.6: Latitudinal profiles of 30-month-mean, zonal-mean, area-weighted vertical pressure velocities $\overline{\omega}^* \times \cos\phi$ of the residual circulation for all dycores at (a) 94 hPa and (b) 27 hPa.

Estimates of the equatorial $\overline{w}^*$ near 70 hPa range from 0.1-0.4 mm s^{-1} in observations and ERA-Interim reanalyses (*Rosenlof*, 1995; *Schoeberl et al.*, 2008; *Seviour et al.*, 2012; *Osprey et al.*, 2013). *Evan et al.* (2012) showed vertical profiles of the tropical (10°S–10°N) annual-mean ERA-Interim $\overline{w}^*$ analyses that are 1.3 mm s^{-1} at 100 hPa (16 km), 0.2-0.3 mm s^{-1} at 70 hPa (18.5 km) and 0.2 mm s^{-1} at 30 hPa (24 km). The QBO simulations by *Giorgetta et al.* (2006) gave tropical (5°S–5°N) annual-mean $\overline{w}^*$ values around 0.8 and 0.2 mm s^{-1} at 100 and 30 hPa, respectively. A recent version of their model showed 0.6 and $0.3-0.35$ mm s^{-1} at these two locations (*Krismer and Giorgetta*, 2014). Furthermore, *Kawatani et al.* (2010) reported on simulated tropical (10°S–10°N) annual-mean w^* values of 0.55 mm s^{-1} (100 hPa) and 0.18 mm s^{-1} (30 hPa), and judged that they were on the low side. Despite the observational uncertainties it seems that the residual vertical velocities in our idealized QBO experiments are weaker than observed, and are thereby not the primary reason for the longer than observed QBO periods in SLD, EUL and SE.

3.4.3 Diffusion and the TEM residual term

All dynamical cores employ dissipation mechanisms, either implicitly in the numerical schemes or explicitly via e.g. horizontal hyper-diffusion. The diffusion is needed to avoid numerical noise, like Gibbs ringing in spectral models, and to keep the model computationally stable. The choice of the diffusion coefficient is often empirical, and can even be considered a model tuning parameter in order to yield a reasonably straight tail in the kinetic energy (KE) spectra in the upper troposphere. In spectral transform models, like EUL with linear 4th-order horizontal hyper-diffusion, the e-folding damping time scale τ of the diffusion is connected to the K_4 diffusion coefficient and the maximum resolved wavenumber n_0 (smallest wavelength) via

$$\tau = \frac{1}{K_4}\left(\frac{a^2}{n_0(n_0+1)}\right)^2. \tag{3.6}$$

In grid-point models like SE with quasi-uniform horizontal grid spacings $\Delta x \approx \Delta y$ this relationship is given by

$$\tau = \frac{(\Delta x)^4}{32\, K_4} \tag{3.7}$$

as documented in *Jablonowski and Williamson* (2011) (their chapter 13.3.4). The selected EUL and SE coefficient of $K_4 = 5 \times 10^{15}$ m^4 s^{-1} at the given resolutions $n_0 = 63$ (EUL) and $\Delta x = 208$ km (SE) leads to damping time scales for the smallest waves of 5.6 h and 2.8 h, respectively. A similar damping time scale of about 7 h for the spectral T63 resolution was also chosen by *Boville* (1991) and *Krismer* (2014).

The strength of the diffusion and thereby the diffusion coefficient greatly influences the steepness of the kinetic energy decay as demonstrated in Fig. 3.7. The figure intercompares the 6-month-mean 250 hPa KE spectra of the four dycores. The analysis is based on 6-hourly instantaneous data. The EUL, SE and FV kinetic energy spectra decay considerably faster with increasing spherical wavenumber n than the SLD spectrum. More specifically, the EUL and SE kinetic energy levels drop off faster from wavenumber $\approx$ 20-25 onwards, and SE damps the smallest scales the greatest which is connected to its short damping time scale. The results suggest that SLD is less diffusive for intermediate- and small-scale waves with wave lengths below 2000 km ($n = 20$) in comparison to EUL and SE. It is interesting that FV shows reduced tropospheric KE levels at even larger scales, e.g. in the presumably resolved wavenumber range 2-20. This finding could be connected to the relatively low, resolved wave activity in FV's equatorial stratosphere, which is discussed later in Chapter 3.6.

As mentioned in Chapter 3.4.1 the TEM residual X captures the zonal wind forcing by nonlinear implicit and linear explicit diffusion as well as the effects of the thermal HS damping, and plays an important role in the zonal momentum balance. It is computed via Eq. (3.1) after all terms except X are assessed based on 6-hourly data sets. In Chapter II we compared the residual X with SLD's implicit numerical

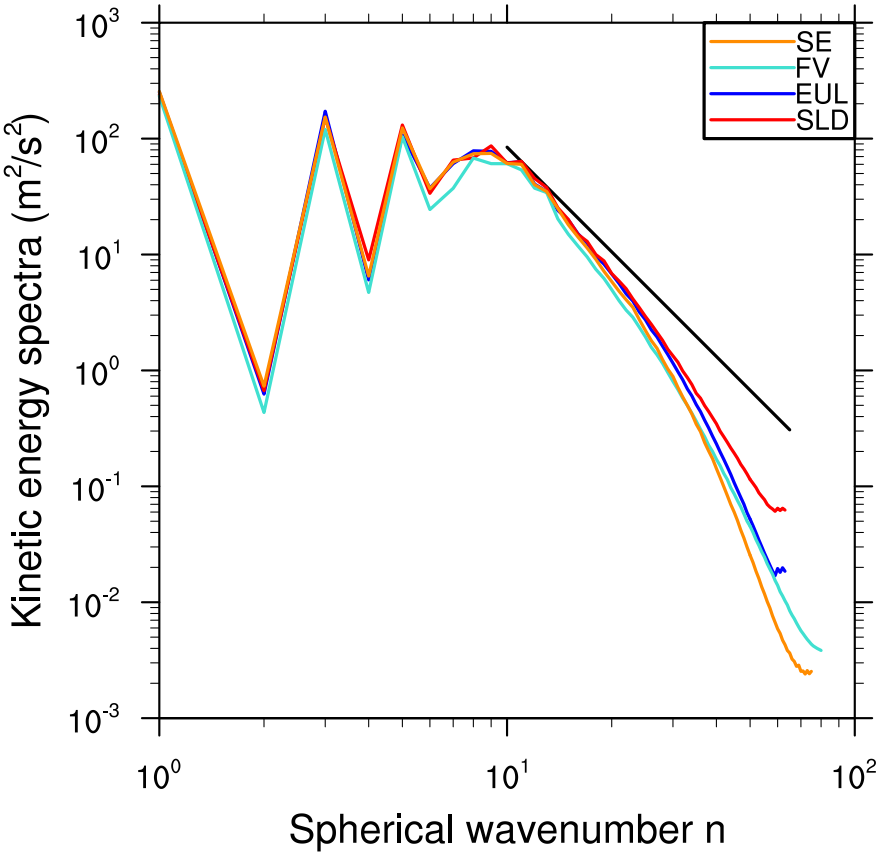

Figure 3.7: 6-month-mean kinetic energy (KE) spectra for the four dycores at 250 hPa. The black line shows the theoretically expected n^{-3} KE decay rate.

diffusion. The latter was approximated via linear 4th-order horizontal hyper-diffusion (*McCalpin*, 1988) and an estimated diffusion coefficient of $K_4 = 5 \times 10^{15}$ m^4 s^{-1}. This coefficient is the same as used in EUL and SE. Figure 3.8 overlays the forcing by the 4th-order horizontal hyper-diffusion (colored) and the TEM residual X (contoured) for (a) a 50-month SLD period from year 7 onwards (reproduced from Chapter II) and (b) a 100-month EUL period from year 20 onwards. In both plots the hyper-diffusion tendencies have very similar patterns than the TEM residual. In addition, even the forcing magnitudes match rather well, so that the damping via the thermal relaxation and other, e.g. nonlinear, effects might be of secondary importance. The analogous analysis for SE resembles the EUL results very closely (not shown). The diffusion mostly explains the residual X and counteracts the resolved wave forcing.

The results do not imply that diffusion must be avoided in QBO simulations. While it is acknowledged that too much explicitly-added diffusion degrades QBO simulations (*Takahashi*, 1996; *Scaife et al.*, 2002), some dissipation is needed to diffuse the strong QBO shear zones, enable their descent and provide a switching mechanism for the alternating QBO phases. The dissipation might be comprised of horizontal or vertical diffusion, or even both. Furthermore, thermal damping can help degrade the QBO shear zones and might mimic the effects of vertical diffusion as stated in *Haynes* (1998). The role of diffusion for the QBO was also discussed in the mechanistic studies by *Plumb* (1977) and *Plumb and Bell* (1982), and will be further analyzed in a companion paper. As *Plumb and Bell* (1982) states "the effects of viscosity are clearly of paramount importance at the equator in counteracting the wave driving and thus limiting the jet magnitudes".

In our experiments, diffusion serves as a crucial QBO forcing mechanism. In fact, it is the delicate balance between the wave forcing and diffusion that determines the faith of the QBO in the HS experiments. As an aside, the role of explicit diffusion in GCM simulations was also analyzed in *Hamilton et al.* (2001) who showed that

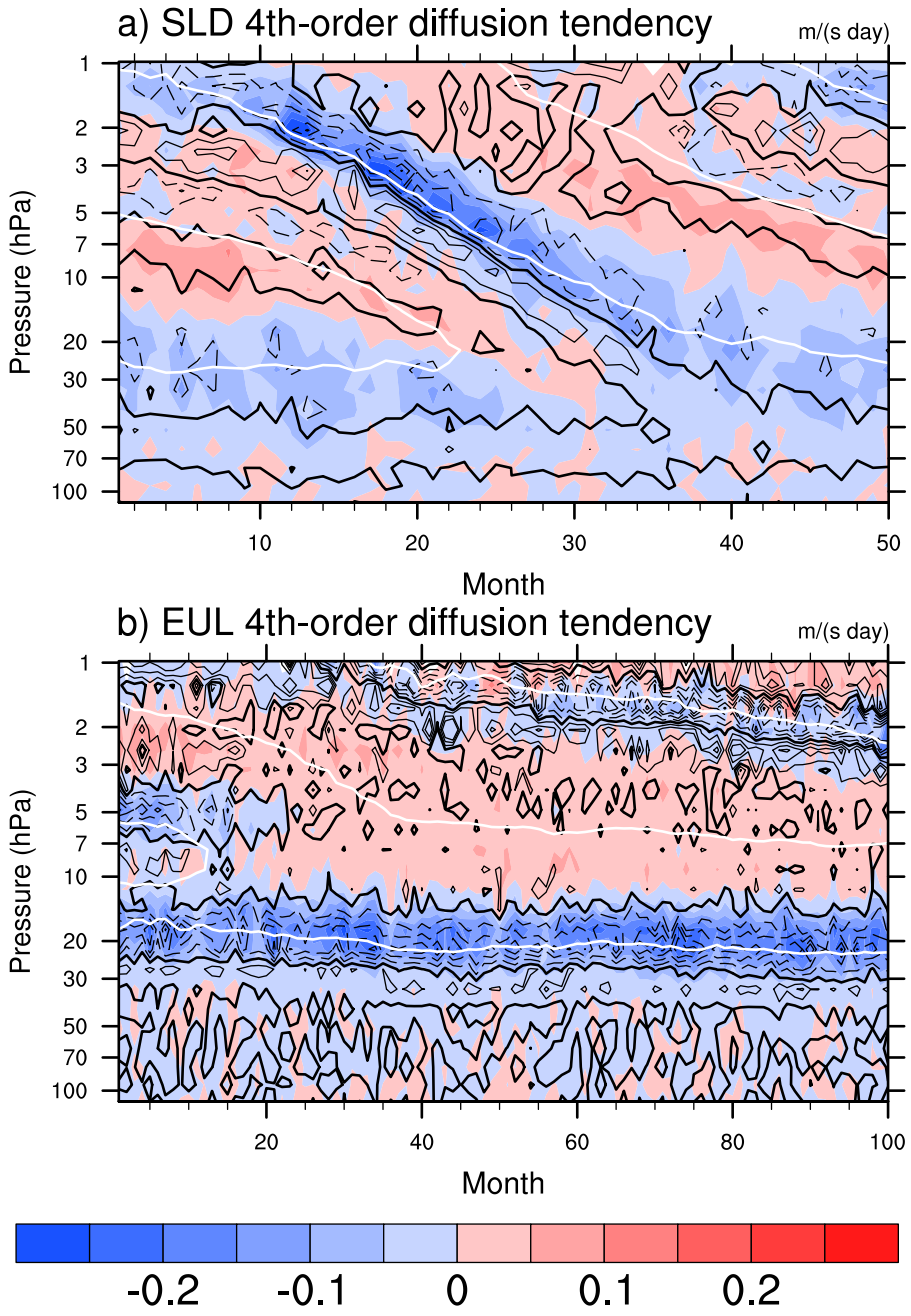

Figure 3.8: Time-pressure cross sections of the monthly-mean zonal-mean acceleration by 4th-order horizontal hyper-diffusion (in color) with $K_4 = 5 \times 10^{15}$ m^4 s^{-1} (averaged between $\pm 2°$) for a) SLD (50 months) and (b) EUL (100 months). The contours of the TEM residual X are overlaid with contour spacing 0.1 m s^{-1} day^{-1}. Negative contours are dashed. The zero contour of the monthly-mean zonal-mean zonal wind is overlaid in white.

diffusive tendencies in the QBO domain can reach considerable magnitudes. However, *Krismer* (2014) (his chapter 3) states that diffusion is two orders of magnitude smaller than other terms in the QBO TEM balance (in particular compared to their parameterized wave drag) and therefore negligible. We hypothesize that this apparent controversy is likely connected to the use (*Krismer*, 2014) or non-use (*Hamilton et al.*, 2001; *Yao and Jablonowski*, 2013) of GWD parameterization schemes. Most often, the zonal wind forcing by parameterized gravity waves becomes so dominant, that other processes could be overshadowed or suppressed. Our idealized HS studies can reveal such sensitivities without judging what the more realistic scenario in nature is. Unfortunately, most QBO-TEM studies in the literature do not discuss their TEM residual X term and thereby leave the budget open. In a companion study, we will report on HS simulations with an added GWD scheme and prescribed gravity wave sources (*Lindzen*, 1981), and re-evaluate the composition of the zonal momentum balance. The results highlight that QBOs in GCMs can be driven by very different forcing mechanisms. Our process study helps disentangle the composition of the forcing, and sheds light on causes and effects.

3.5 Wave generation and instability indicators

Resolved waves and their wave-mean flow interactions are important drivers of the QBO in the idealized HS experiments. In nature, a broad spectrum of planetary-scale waves and small-scale gravity waves are generated via many different mechanisms such as topography, land-sea temperature contrasts, convection, wind shear, dynamic instabilities, geostrophic adjustments of unbalanced flows in the neighborhood of jet streams and frontal zones, and nonlinear wave-wave interactions (see e.g. the review by *Fritts and Alexander* (2003) or *Plougonven et al.* (2003)). The term wave-wave interactions refers to wave superpositions that have been observed to be a source of middle-atmosphere gravity waves. Free traveling planetary (Rossby) modes or global

normal modes are also present in the middle atmosphere that might potentially be linked to barotropic and baroclinic instability as suggested by *Andrews et al.* (1987) (their chapters 4.4 and 5.5). Furthermore, midlatitudinal Rossby waves have been observed to trigger equatorial MRG and Kelvin waves (*Magaña and Yanai*, 1995; *Straub and Kiladis*, 2003). A comprehensive analysis of all wave generation mechanisms and how they might relate to the QBOs in the SLD, EUL and SE dynamical cores is beyond the scope of this chapter. This topic is even an active research area and not fully understood. However, we can narrow down the potential wave generation mechanisms by noting that topography, land-sea temperature contrasts and convection can be ruled out due to the HS experimental setup. In particular, we now explore whether dynamic instability indicators show systematic differences in the dynamical cores.

Instabilities can serve two purposes. They can either act as a launch pad for waves or, alternatively, can trigger local turbulence and mixing, thereby acting as a wave dissipation mechanism and a preventer of very large vertical wind shears. We explore both routes. In particular, we assess the following instability indicators that are necessary, but not necessarily sufficient, conditions for the occurrence of barotropic, inertial, baroclinic, static and Kelvin-Helmholtz (KH) instabilities. These are

$$f(f+\zeta) < 0 \quad \text{(inertial)} \tag{3.8}$$

$$\beta^* = \frac{\partial(f+\zeta)}{a\partial\phi} < 0 \quad \text{(barotropic)} \tag{3.9}$$

$$\frac{\partial PV}{a\partial\phi} < 0 \quad \text{(baroclinic \& barotropic)} \tag{3.10}$$

$$Ri = \frac{N^2}{(\partial u/\partial z)^2} < 0 \quad \text{(static)} \qquad < 0.25 \quad \text{(KH)} \tag{3.11}$$

where ζ symbolizes the relative vorticity, PV stands for Ertel's potential vorticity, β^* is defined as the meridional gradient of the absolute vorticity, and Ri is the definition of the Richardson number that relates the squared Brunt-Väisälä frequency N^2 and

the vertical shear $\partial u/\partial z$ of the zonal wind. The use of ζ in Eqs. (3.8) and (3.9) instead of the often used meridional gradient of the zonal-mean zonal flow $\overline{u}_y$ captures zonal asymmetries as suggested by *O'Sullivan and Hitchman* (1992). The Richardson number serves two purposes. A negative Ri number indicates static instability which triggers overturning circulations. In case of $Ri < 0.25$ the criterion for the KH shear instability is fulfilled.

Inertial instability is a parcel instability that occurs frequently in equatorial regions where the meridional shear of the zonal wind is strong (*Andrews*, 1987). In case of inertial instability meridional circulations arise in order to redistribute the angular momentum imbalance. Baroclinic instability is most dominant in the mid- and high latitudes. It fosters the development of extratropical waves which have been observed to trigger Kelvin waves in the equatorial region (*Straub and Kiladis*, 2003; *Yang et al.*, 2007). Furthermore, the sign reversal of the meridional PV gradient (the *Charney and Stern* (1962) stability criterion) is also present in tropical latitudes and indicates the possible presence of baroclinic and/or barotropic instability as a local wave trigger. We also assess the condition for barotropic instability independently via β^* that is of central importance in the tropics. The necessary condition is that β^* must switch sign.

3.5.1 Instabilities in the upper troposphere

It is widely known that upward traveling waves with tropospheric origins can transport energy and momentum into the tropical middle atmosphere. As suggested in *Nissen et al.* (2000) dynamic instabilities might serve as a trigger for such tropical waves. In particular, *Nissen et al.* (2000) linked an increased number of PV-gradient sign reversals in the upper equatorial troposphere to an increased Kelvin wave activity in their model. In order to check for such occurrences Fig. 3.9 depicts selected 30-day Hovmöller diagrams in the upper atmosphere (at 300 hPa near the equator)

for all instability indicators. The shaded areas are negative and indicate where the instability criterion is satisfied. The Kelvin-Helmholtz (KH) criterion $Ri < 0.25$ is marked in red in the rightmost column.

The figure shows that the conditions for KH and static instabilities are rarely satisfied at 300 hPa. However, this does not generally exclude KH instability as a possible wave generation process in the tropics since the excitation of large-scale gravity waves has been documented for unstable shear layers in zonal jets (*Fritts*, 1982, 1984). The persistent easterly jets above the tropical tropopause (between 80-40 hPa, Fig. 3.3) could therefore be candidates for KH instabilities, which will be investigated further in the future. All other instability indicators at 300 hPa show intermittent, but rather organized, patterns that mostly travel westward. The barotropic and baroclinic instability indicators are most often fulfilled by the SLD dynamical core. The shaded areas of the inertial instability indicators seem to be comparable in all four dycores. In general, the density of the shaded areas for all five stability indicators in FV, EUL and SE does not reveal any systematic differences. However, the magnitudes of the FV indicators are generally lower than the magnitudes of the indicators in SLD, EUL and FV (not shown, but see a second example for inertial instability in Fig. 3.10). These higher magnitudes in SLD, EUL and SE most likely lead to a more effective triggering of instabilities and tropospheric waves.

3.5.2 Instabilities in the stratosphere

While tropospheric instabilities might serve as wave triggers, stratospheric instabilities are most likely connected to upward propagating breaking waves which trigger turbulence and mixing (*Dunkerton*, 1981; *Fritts and Rastogi*, 1985; *Hayashi et al.*, 2002). Gravity wave drag schemes are often built upon this principle, such as the scheme by *Lindzen* (1981). It dissipates parameterized gravity waves once the conditions for convective overturning (static instability) or Kelvin-Helmholtz insta-

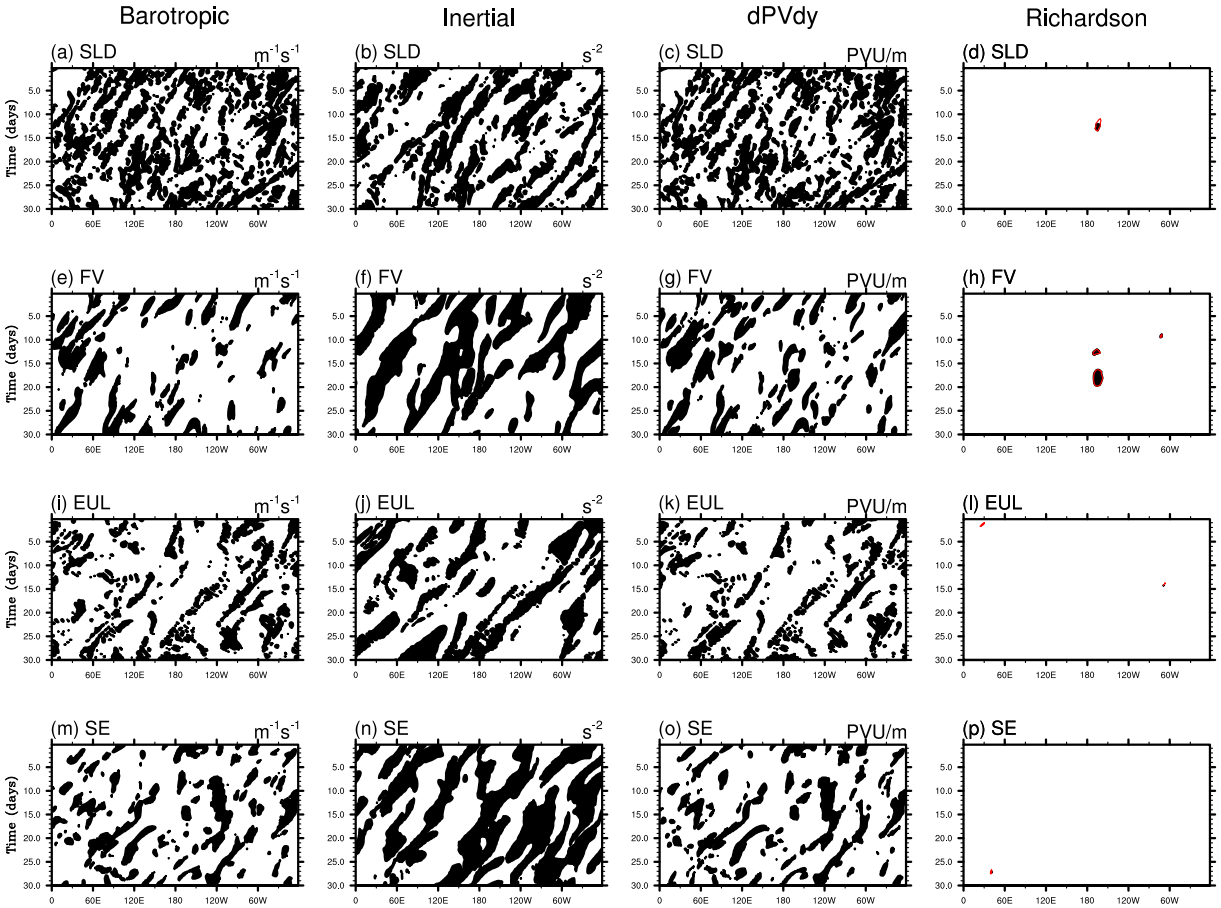

Figure 3.9: 30-day Hovmöller diagrams at 300 hPa along the closest latitude to the equator in the Northern Hemisphere for different instability indicators: (leftmost column) barotropic, (second column) inertial, (third column) baroclinic, and (rightmost column) Kelvin-Helmholtz and static instability via Richardson (Ri) number). Time goes down. The rows depict (a-d) SLD, (e-h) FV, (i-l) EUL and (m-p) SE. Shaded areas are negative which means that the criterion is fulfilled. The $Ri < 0.25$ contour is marked in red in the rightmost column.

bility are fulfilled according to a "saturation" theory. Inertial instability in the upper atmosphere occurs in the form of a "pancake structure" that appears in the divergence of the meridional wind field. As discussed by *O'Sullivan and Hitchman* (1992), if a parcel in a rotating field is displaced by a meridional distance δy it accelerates at the rate

$$\frac{\partial^2 \delta y}{\partial t^2} = -f(f+\zeta)\delta y \tag{3.12}$$

if $f(f+\zeta) < 0$. Since the acceleration is in the direction of δy, local divergence results. Once the parcel passes its neutral state, deceleration leads to local convergence. The divergence and convergence zones alternate in the horizontal and are vertically stacked (the "pancake"). The disturbance growth-rate is largest at small vertical scales whose size depend on the diffusive properties of the model (*Dunkerton*, 1981). *Hayashi et al.* (2002) showed that pancake structures occasionally occur in observations near the stratopause and in the mesosphere where they last for about two weeks. In our dynamical core simulations we observe rather persistent pancake structures in the stratosphere near the QBO domains.

Figure 3.10 shows the zonal-mean divergence $[(a\cos\phi)^{-1}\partial(\overline{v}\cos\phi)/\partial\phi]$ of the meridional wind for each dycore, using a single instantaneous data snapshot. In SLD the pancake structure is present upwards of about 50 hPa and reaches a peak magnitude of 2×10^{-6} s^{-1}. The occupied latitudinal region expands with increasing height and extends to 30° N/S near the model top. This meridional width is typical, and was also found by *Hitchman et al.* (1987) and *O'Sullivan and Hitchman* (1992). In the FV dycore (Fig. 3.10b), the divergence pattern is an order of magnitude weaker and barely visible, suggesting that mixing processes via inertial instability might not be important in FV's stratosphere. In EUL and SE (Fig. 3.10c,d), the peak values are around 5×10^{-6} s^{-1}, and the structure expands slightly beyond 30° N/S. The pancake patterns in all models propagate downward over time, which was also observed by *Hitchman et al.* (1987). *Hitchman et al.* (1987) reported on correlations

between the tropical pancake structure and midlatitudinal Rossby waves. However, in our simulations it is difficult for midlatitudinal Rossby waves to propagate into the upper equatorial region due to the persistent easterlies that surround the QBO domain (see Fig. 3.3). We therefore suggest that the inertial instability patterns in Fig. 3.10 could be connected to resolved-scale breaking gravity waves in the tropics with upward oriented energy transports (upward group speeds), whose corresponding phase speeds point downward. This possible link needs further investigation.

In addition to inertial instability, barotropic instability is also commonly observed in the QBO domain due to the rather narrow westerly equatorial jets (*Hamilton*, 1984). The instability happens persistently around $\pm 15^{\circ}$ in observations and lasts for multiple months, which was e.g. shown by *Shuckburgh et al.* (2001). They demonstrated that mixing in the tropics and subtropics is a consequence of both breaking planetary waves and barotropic instability. *Shuckburgh et al.* (2001) also showed that negative β^* regions were correlated with increasing E-P flux divergence, and occurred predominantly in easterly QBO regions that flank the westerly jet. This pattern was also reported by *Hamilton et al.* (2001) for their QBO simulations.

Figure 3.11 depicts instantaneous latitude-pressure snapshots of negative β^* (striped) which overlay the zonal wind (colored) at a selected longitude. As also seen by *Hamilton et al.* (2001) and *Shuckburgh et al.* (2001) the regions with negative β^* in Fig. 3.11 are mostly located in the easterly wind zone and flank the westerly jet in all four dycores. FV shows the fewest occurrences of negative β^* which is also obvious at other times (not shown). The characteristics of the negative β^* distributions in EUL and SE are similar and seem to occupy wider areas in the stratosphere in comparison to SLD. As an aside and related to the earlier tropospheric discussion, Fig. 3.11 also shows intermittent negative β^* throughout the tropical troposphere where barotropic instability could serve as a source for tropical waves.

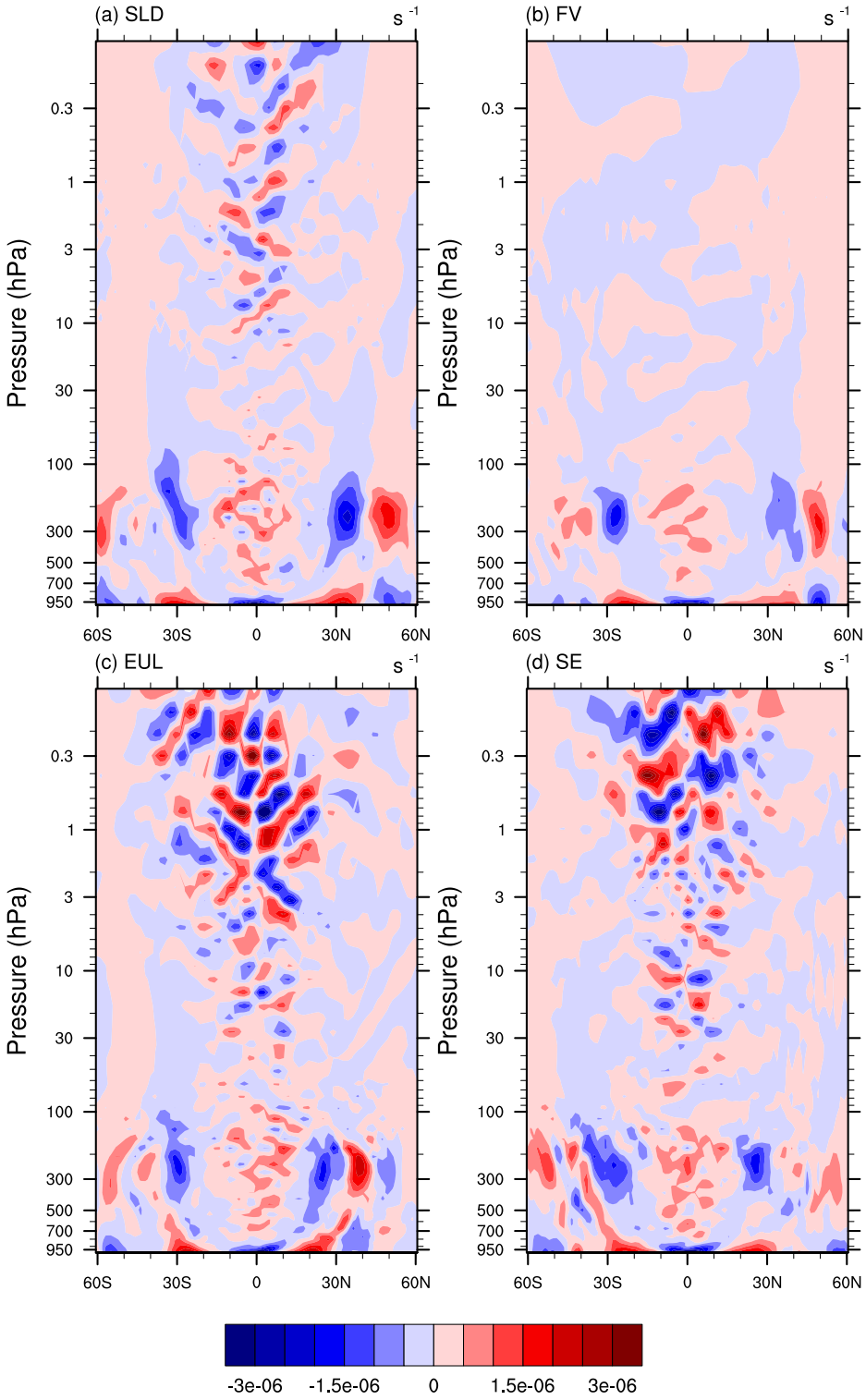

Figure 3.10: Latitude-pressure cross sections of the zonal-mean divergence of the meridional wind for an instantaneous data snapshot for a) SLD, b) FV, c) EUL and d) SE.

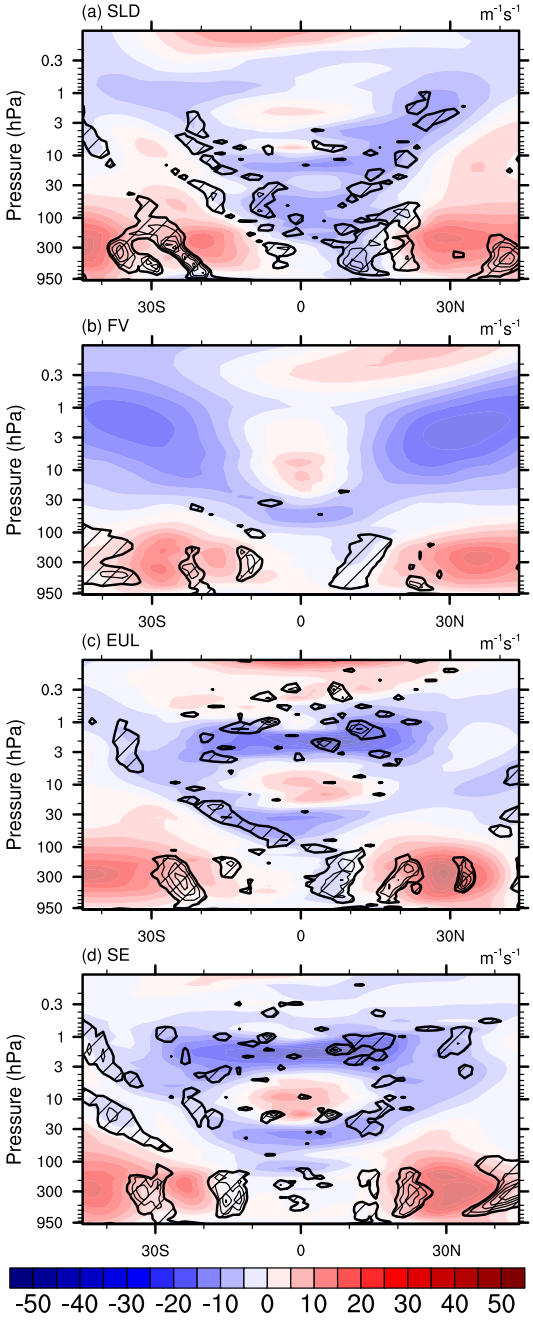

Figure 3.11: Latitude-pressure cross sections of β^* (negative areas are striped) and the zonal wind (colored) for an instantaneous data snapshot at a selected longitude for (a) SLD, (b) FV, (c) EUL and (d) SE.

3.6 Wave analysis

In order to compare the resolved wave activity in the four dynamical cores, a wavenumber-frequency analysis is performed following the analysis method by *Wheeler and Kiladis* (1999). The analysis uses 6-hourly instantaneous temperature data for 30 months, from 15°N to 15°S at ∼22 hPa. The wavenumber-frequency spectra are based on many successive overlapping (by 30 days) 96-day data segments that are averaged over the 30 months. The corresponding simulation years for each dycore are the same as listed in Chapters 3.4 and 3.4.2.

Yang et al. (2011) showed how the wavenumber-frequency spectra are impacted by the Doppler shift in the presence of different zonal background velocities. From linear shallow water theory, the background wind modifies the dispersion curves according to $\omega = \omega_0 + \bar{u}k$ where ω and ω_0 are the wave frequencies with and without the Doppler shift, $\bar{u}$ denotes the zonal background wind and k stands for the zonal wavenumber. In the wavenumber-frequency analyses (Fig. 3.12) we overlay the dispersion curves with background wind speed $\bar{u} = 0$ m s^{-1} (solid lines) and the Doppler-shifted dispersion curves with background wind speed $\bar{u} = -7$ m s^{-1} (dashed lines) for the equivalent depths h of 12, 50, and 200 m. These equivalent depths correspond to the zonal wave speeds c of about 11, 22 and 44 m s^{-1} ($c = \sqrt{gh}$ with gravity g) and approximate vertical wavelengths L_z of 2.8, 6.2 and 12.6 km, assessed via $m^2 = N^2/(gh) - 1/(4H)$, where $m = 2\pi {L_z}^{-1}$ symbolizes the vertical wavenumber. These linear estimates take into account that the squared stratospheric Brunt-Väisälä frequency N^2 in the tropics and stratospheric scale height H are given by $N^2 \approx 5 \times 10^{-4}$ s^{-2} and $H \approx 5.85$ km in the idealized simulations. This range of phase speeds and vertical wavenumbers encapsulates the typical range of observed equatorially trapped waves in the stratosphere like Kevin and MRG waves. Thereby, our analysis sheds light on their presence in idealized simulations that omit important wave generation mechanisms, like moist convection.

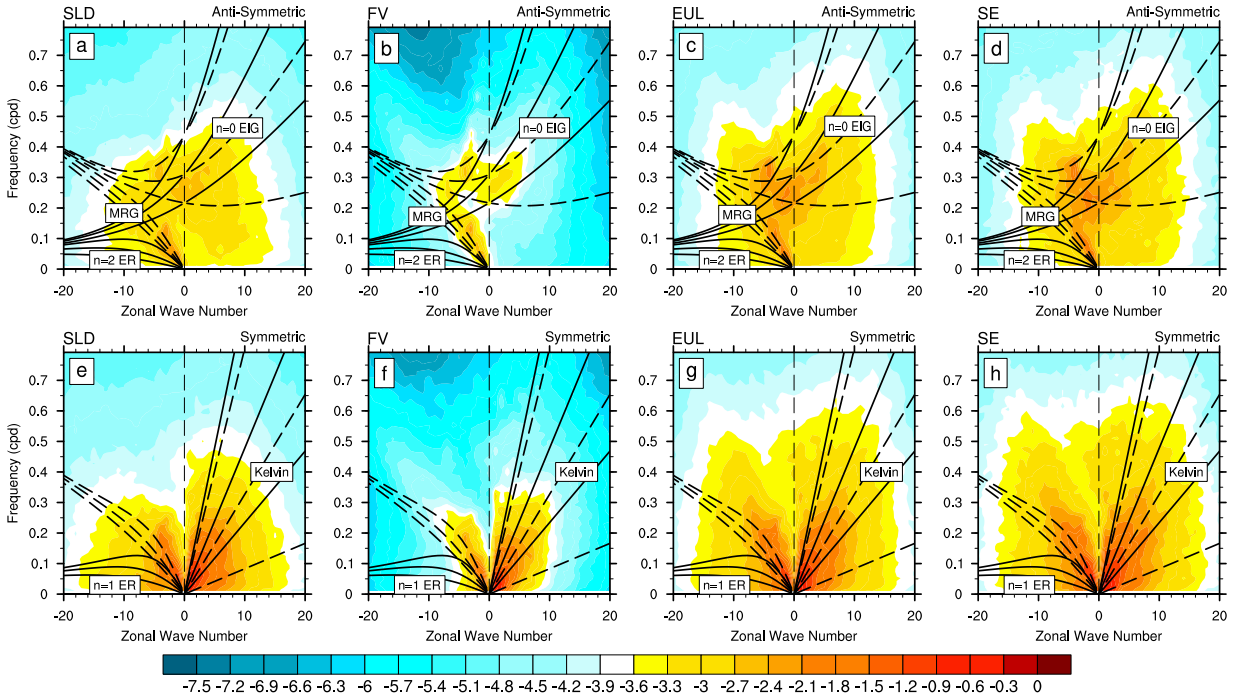

Figure 3.12: Wavenumber-frequency analyses for the temperature field at 22 hPa: raw power spectra (logarithmic scale in $\log_{10}$(K)) for SLD, FV, EUL and SE (from left to right), averaged over 30 months in the region 15°S-15°N. The first (second) row shows the anti-symmetric (symmetric) component. The overlaid solid ($\overline{u} = 0$ m s^{-1}) and Doppler-shifted dashed ($\overline{u} = -7$ m s^{-1}) dispersion curves correspond to h = 12, 50 and 200 m (lowest lines are h = 12 m). Negative wavenumbers indicate easterly waves.

Figure 3.12 shows the $\log_{10}$ of the raw power spectrum of the temperature wavenumber-frequency analyses for (a,e) SLD, (b,f) FV, (c,g) EUL and (d,h) FV. The first row is the anti-symmetric component and the second row is the symmetric component. In the anti-symmetric plots we depict the dispersion curves for MRG, n=0 Equatorial Inertia-Gravity waves (EIG) and n=2 Equatorial Rossby waves (ER). In the symmetric plots we show the dispersion curves for Kelvin waves and n=1 ER. The symbol n is the meridional mode number. As e.g. discussed in *Tindall et al.* (2006), the temperature waves are symmetric when n is odd and anti-symmetric when n is even. Negative (positive) zonal wavenumbers indicate easterly (westerly) waves.

The anti-symmetric plots show spectral peaks for n=2 ER. The spectral peaks for ER mainly lie around wave numbers -1 to -5 with frequencies $\leq$ 0.2 cycles per day (cpd). Spectral peaks for MRG at wavenumber 4 are apparent with periods of 3-4 days. Moreover, spectral peaks for n=0 EIG waves are detected in the anti-symmetric plots. In the symmetric plots, strong peaks for Kelvin waves and n=1 ER are detected with small wavenumbers and low frequencies. However, these wave signals are highly influenced by the background red noise. A wavenumber-frequency plot for the SLD simulation without the background signal was shown in Chapter II. It revealed that the most dominant peaks in the Kelvin wave regime lie around wavenumbers 1-2 with 15–30-day periods. The wave signatures follow the Doppler-shifted dispersion curves rather closely.

In Fig. 3.12 we do not remove the background spectrum, since it carries important information about the overall resolved wave activity in the four dycores. The reduced occurrence of the strong (yellow- and red-colored) power range in FV indicates a reduced wave activity in both the anti-symmetric and symmetric regimes. This is also true at different pressure levels. The SLD simulation shows moderate wave activity. EUL and SE exhibits the strongest resolved wave activities which are of comparable strenghts. The wave activity in all models correlates well with their corresponding TEM analyses (Chapter 3.4) and instability discussions (Chapter 3.5). It shows that equatorial wave activities are abundant in the QBO models SLD, EUL and SE. These models have strong forcings by the E-P flux divergence and high potential for dynamic instabilities, which possibly served as wave triggers. On the other hand, the model with the fewest resolved waves, lowest E-P flux divergence, weakest potential for dynamic instabilities and no QBO is FV.

As vertically propagating waves grow their amplitudes with height, they start to break and transfer momentum and energy to the background wind field. The waves are strongly absorbed near their critical levels when their phase speeds approach the

speeds of the background flow. The QBO thereby works as a wave filter. This is demonstrated in Fig. 3.13 that shows the temperature wavenumber-frequency analyses at 181, 94, 22 and 2 hPa for the SE dynamical core as an example. The 30-month analysis period covers year 12.25-14.75 of the SE simulation that is characterized by weak easterly equatorial flows at 184 and 94 hPa, the transition from easterlies to the westerly QBO jet at 22 hPa, and mostly westerly conditions at 2 hPa as seen in Figs. 3.1d and 3.3d. The wave power in the temperature field at 181 hPa is low. This is typical as upward traveling temperature waves have small amplitudes in the troposphere due to their strong dependence on static stabilty (which is small in the equatorial troposphere).

Figures 3.13b,f show that the tropospheric waves have gained strength due to the decrease in density and increase in static stability around the tropopause level (94 hPa), especially the n = 2 ER and MRG waves in the anti-symmetric field. In addition, Kelvin waves are prominent at these levels. The easterly background flow in the region 94–22 hPa with jet speeds between 0 to -22 m s^{-1} (Fig. 3.1d) absorbs easterly waves of matching phase speeds, corresponding to the equivalent depths below $h = 50$ m. This absorption can best be seen in the $n = 1$ and $n = 2$ ER waves. Between 94 and 22 hPa the strengths of the slow ER waves with small wavenumbers are diminished and their peak magnitudes are shifted upright towards faster waves with higher equivalent depths (Fig. 3.13c). This shift is also somewhat visible in the MRG regime, although the absorption of slow MRG modes is incomplete during their upward propagation, which contributes to the lack of easterly wave driving in SE. Kelvin waves are unaffected by the easterly background flow below 22 hPa and propagate through it. However, between 22-2 hPa the mostly westerly background jet reaches magnitudes between 0-15 m s^{-1} and filters slow Kelvin waves with matching phase velocities. This is visible in Figs. 3.13g,h that show diminished Kelvin wave amplitudes at 2 hPa for small h. The amplitude distribution of the Kelvin waves

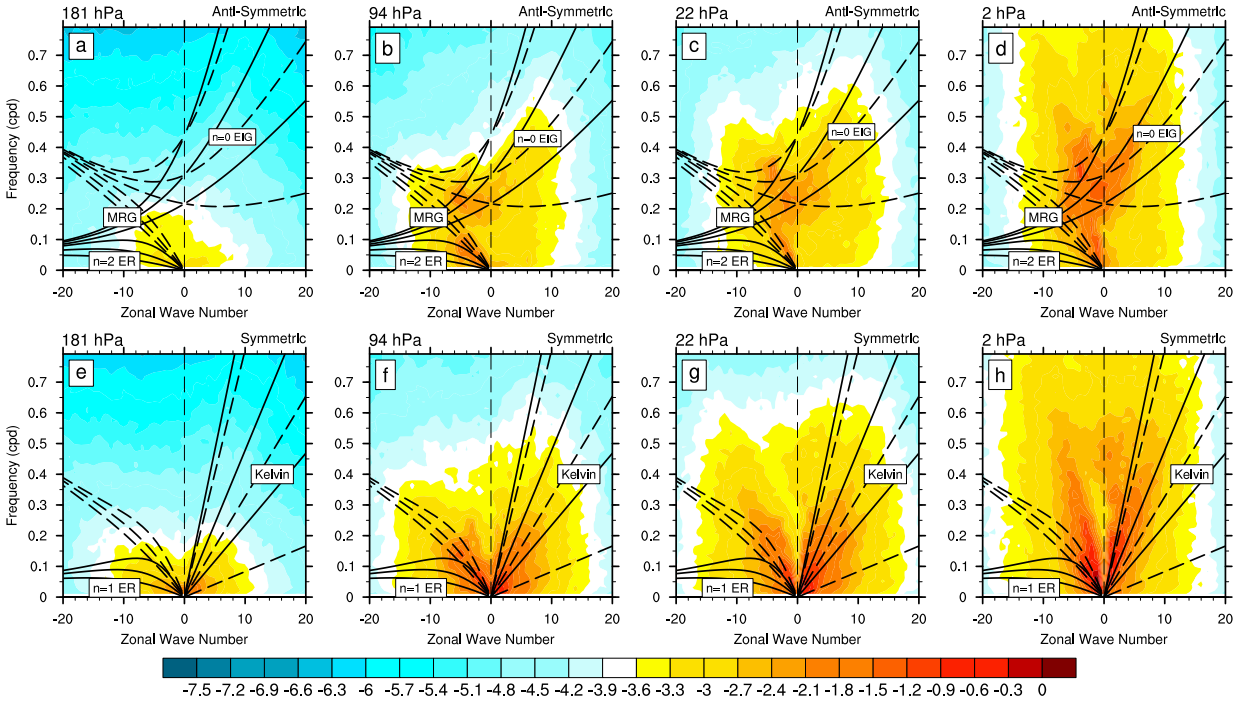

Figure 3.13: Wavenumber-frequency analyses for SE's temperature field: raw power spectra (logarithmic scale in $\log_{10}$(K)) at 181, 94, 22 and 2 hPa (from left to right), averaged over 30 months in the region 15°S-15°N. The first (second) row shows the anti-symmetric (symmetric) component. The overlaid solid ($\overline{u} = 0$ m s^{-1}) and Doppler-shifted dashed ($\overline{u} = -7$ m s^{-1}) dispersion curves correspond to $h = 12$, 50 and 200 m (lowest lines are $h = 12$ m). Negative wavenumbers indicate easterly waves.

becomes more upright and shifts towards faster Kelvin waves (with $h > 50$ m) which travel undisturbed through the stratosphere. Similar absorption patterns were also found in *Yang et al.* (2011) and *Krismer and Giorgetta* (2014).

3.7 Sensitivity of the QBO simulation to resolution and dissipation

In order to understand the role of model resolution and numerical dissipation schemes, several experiments are conducted to test the sensitivity of the QBO-like behavior to different horizontal and vertical grid-spacings and numerical diffusion

coefficients and sponge layer schemes. Here, we only focus on the SLD experiments to provide motivating examples for future sensitivity studies.

Figure 3.14 shows the QBO-like simulation in SLD with different horizontal 4th-order hyper-diffusion coefficients (monthly-mean zonal-mean zonal wind at the equator). The model resolution is kept the same as shown earlier, which is T63 in the horizontal and 55 levels in the vertical. Figure 3.14A is the same as figure 3.1a, but for 30 years, which are simulated without explicit numerical diffusions. Figure 3.14B, C and D are simulations with diffusion coefficient B) $K_4 = 5\times\ 10^{15}$ m^4 s^{-1}, C) $K_4 = 1\times\ 10^{16}$ m^4 s^{-1} and D) $K_4 = 2\times\ 10^{16}$ m^4 s^{-1}, respectively. The QBO period is $\sim$ 3.6 years without explicit diffusion, $\sim$ 3 years with $K_4 = 5\times\ 10^{15}$ m^4 s^{-1}, $\sim$ 2.7 years with $K_4 = 1\times\ 10^{16}$ m^4 s^{-1} and $\sim$ 2.5 years with $K_4 = 2\times\ 10^{16}$ m^4 s^{-1}. The QBO period become shorter with higher diffusion coefficient, but the wind amplitude diminishes with increasing the strength of the explicit horizontal diffusion. Moreover, the westerly domain of the QBO-like oscillation shrinks and sits higher with increasing explicit diffusion. The westerly domain occupies the region between 30 to 0.3 hPa in figure 3.14a and 20 to 0.3 hPa in Figure 3.14d. Therefore, too much diffusion suppresses the QBO.

Figure 3.15 shows the monthly-mean zonal-mean zonal wind at the equator with different horizontal resolution in the SLD simulation. No explicit horizontal diffusion is used, and the vertical resolution is the same as before (55 levels). Figure 3.15E to 3.15H are simulations with T42 (313 km grid-spacing around the equator), T63 (208 km), T85 (156 km) and T106 (125 km) respectively. The QBO-like periods are 48 months (E, T42), 45 months (F, T63), 36 months (G, T85) and 32 months (H, T106) due to the improved wave forcing at higher resolutions. This shows that increased horizontal resolution speeds up the QBO period. The QBO-like oscillations occupy the vertical domain around 30- 1 hPa which does not vary with different horizontal resolutions. However, the wind amplitude changes slightly with different horizontal

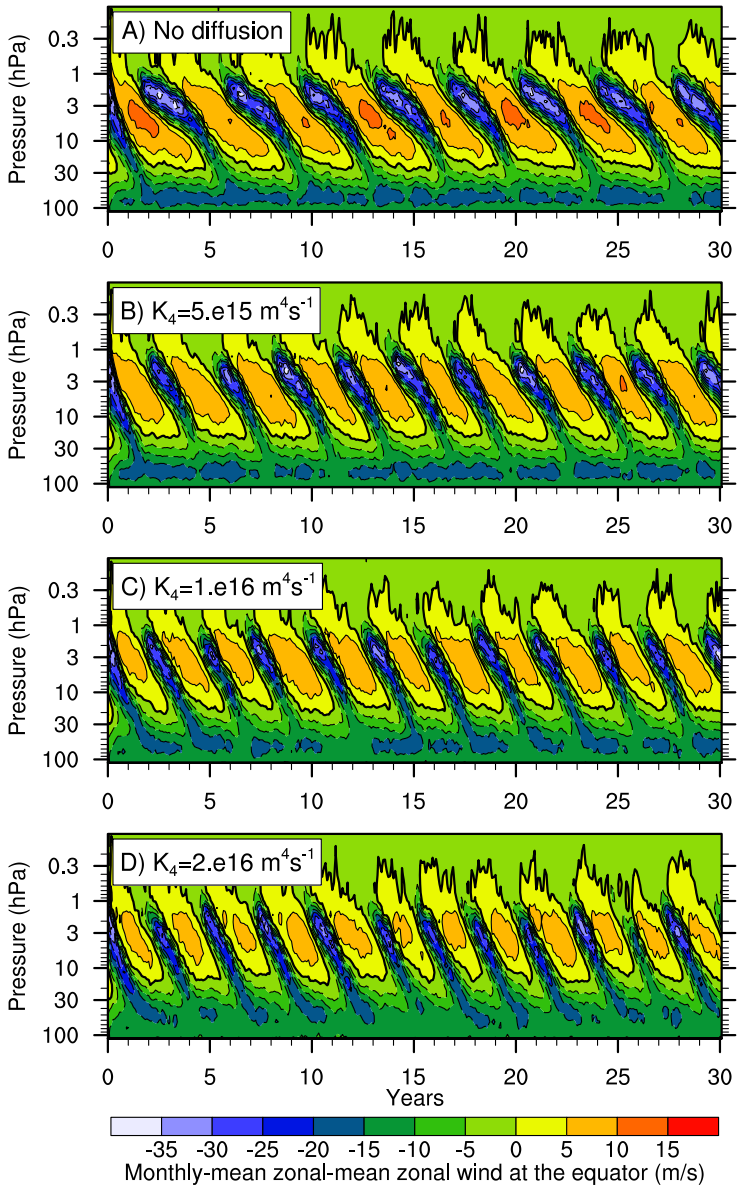

Figure 3.14: Zonal-mean monthly-mean zonal wind time-height cross sections averaged between 2° N/S in the SLD dynamical core with different horizontal diffusion coefficients A) no diffusion, B) $K_4 = 5\times\ 10^{15}$ m^4 s^{-1}, C) $K_4 = 1\times\ 10^{16}$ m^4 s^{-1}, D) $K_4 = 2\times\ 10^{16}$ m^4 s^{-1}.

resolution. The T63 and T85 simulations have slightly stronger maximum westerly wind amplitudes ($\sim$ 15 m s^{-1}) compared to T42 and T106 simulation ($\sim$ 10 m s^{-1}).

Figure 3.16 depicts SLD simulations with different sponge layer setups, with the horizontal resolution T63 and no explicit numerical diffusion applied. The QBO-like oscillations show very different characteristics. Figure 3.16I shows a simulation without Rayleigh friction (RF) above 1 hPa. The wind amplitudes are high from $\sim$ -40 m s^{-1} to $\sim$ 30 m s^{-1}, and the oscillation extends to the model top at $\sim$ 0.1 hPa and beyond, the QBO-like period is longer than 15 years. Figure 3.16J has RF applied above 10 hPa with the same coefficient K_r as in Chapter 3.2.2. The QBO-like period is around 2.7 years, which is shorter than the QBO period in figure 3.14a with RF applied above 1 hPa and the identical K_r coefficient. Figure 3.16K and 3.16L shows RF applied at same position (1hPa) but with different strength. Figure 3.16 halves strength of the coefficient K_r in comparison to figure 3.14a. The QBO period is around 4.3 years. Figure 3.16L shows a simulation which the strength of the RF coefficient K_r in comparison to figure 3.14a. The period is $\sim$ 3.3 years. This shows that an increased strength of the Rayleigh friction sponge layer speeds up the QBO period. It also shows that the magnitude of the zonal wind is impacted by the sponge layer characteristics.

Figure 3.17 provides simulation results with horizontal resolution T63 but 67 vertical levels (with Δz = 900 m grid spacing) in the SLD simulation with different diffusion schemes and coefficients. Figure 3.17M shows simulation without explicit diffusion. The model can not sustain the QBO-like oscillation despite the better vertical resolution. Potentially, increased vertical resolution lets QBO vanish due to decreased numerical diffusion in the vertical. Figure 3.17N shows simulation with explicit 2nd-order diffusion in the vertical (with the coefficient $K_v = 0.5$ m^2 s^{-1}). The QBO recovers with a period around 4.3 years, in the domain between 20 to 1 hPa. With 4th-order horizontal diffusion (K_4= 5$\times$ 10^{15} m^4 s^{-1} in figure 3.17O and K_4 =

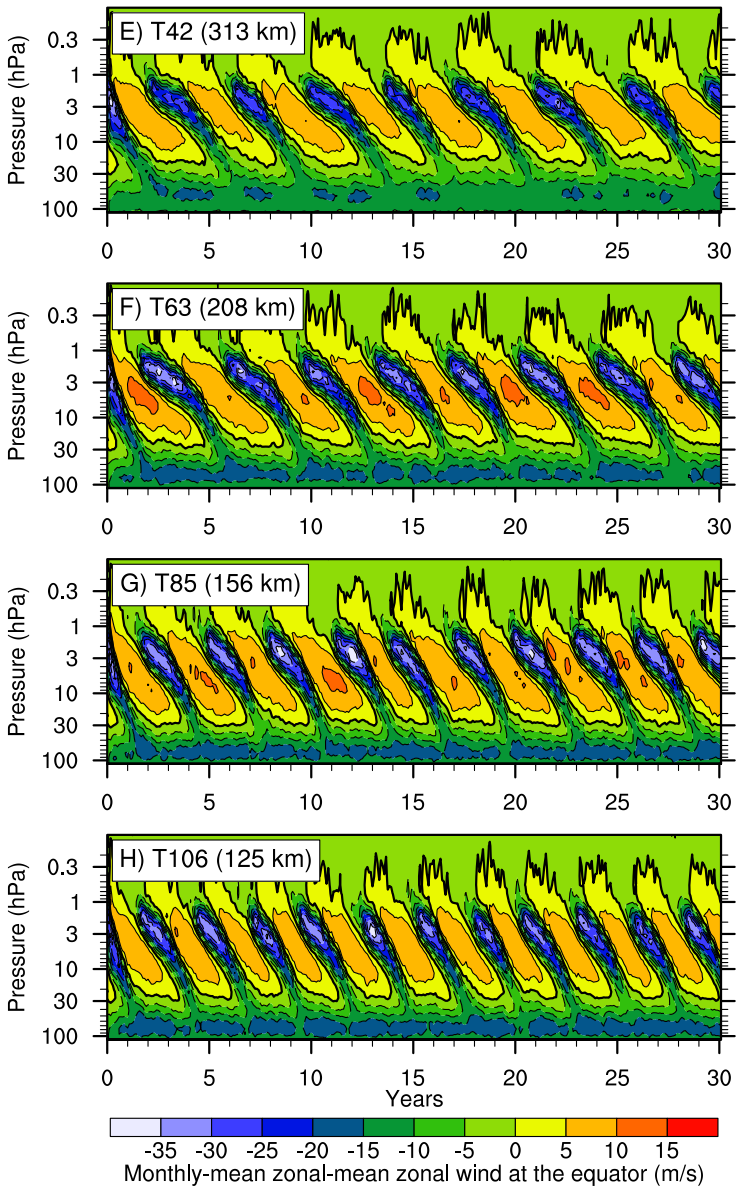

Figure 3.15: Zonal-mean monthly-mean zonal wind time-height cross sections averaged between 2° N/S in SLD dynamical core with different horizontal resolutions E) T42 (313 km), F) T63 (208 km), G) T85 (156 km), H) T106 (125 km).

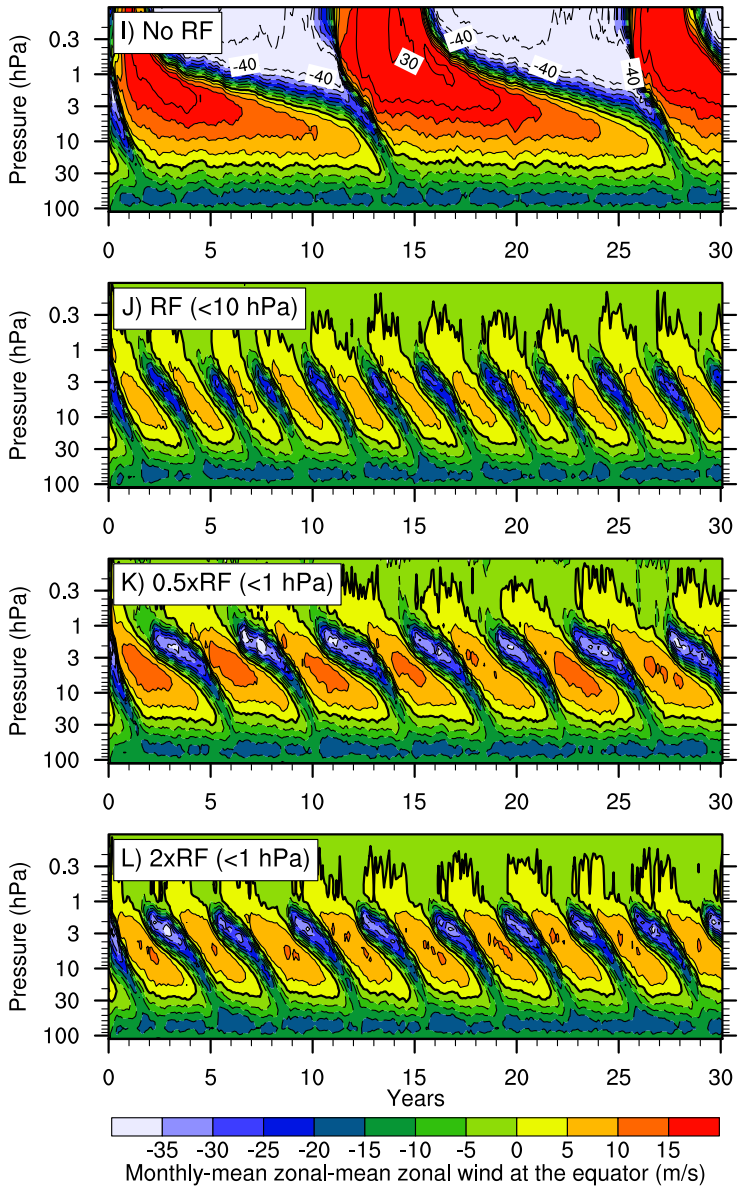

Figure 3.16: Zonal-mean monthly-mean zonal wind time-height cross sections averaged between 2° N/S in the SLD dynamical core with different sponge layer characteristics I) no Rayleigh Friction, J) Rayleigh Friction applied at levels between 10 hPa to model top, K) 0.5× Rayleigh Friction applied at levels between 1 hPa to model top, L) 2× Rayleigh Friction applied at levels between 1 hPa to model top.

$2\times\ 10^{16}$ m^4 s^{-1} in figure 3.17P), the QBO-like oscillation recovers as well. However, the oscillation periods vary greatly dependen on the diffusion coefficient. The QBO period is longer than 10 years with $K_4 = 5\times\ 10^{15}$ m^4 s^{-1} in figure 3.17O, and ~ 4 years with $K_4 = 2\times\ 10^{16}$ m^4 s^{-1} in figure 3.17P.

These sensitivity studies demonstrate the paramount impact of the diffusion and sponge layer characteristics on the atmospheric circulation. This will be explored in greater detail in a future study.

3.8 Summary and outlook

This study demonstrated that QBO-like oscillations can be simulated in an ensemble of dry GCM dynamical cores when driven by the *Held and Suarez* (1994) forcing. The HS forcing replaces the complex physical parameterization package in GCMs with a simple Newtonian temperature relaxation and low-level Rayleigh friction, that mimic the radiative transfer and planetary boundary layer mixing on a flat Earth. Such an idealized setup gives easier access to an improved understanding of causes and effects in dynamical cores, that are otherwise difficult to isolate. The tropical stratospheric circulations in four dynamical cores were explored that are options in CAM5. These are the SLD, FV, EUL and SE dynamical cores which are built upon the same hydrostatic equation set, but utilize different numerical schemes, diffusion mechanisms, computational grids and mesh staggering options. The central question was how the model design choices impact the wave generation, propagation and dissipation mechanisms in the equatorial region, and whether QBO-like oscillations are supported in the tropical stratosphere. Identical stratospheric grid spacings of about $\Delta x \approx 210$ km and $\Delta z = 1.25$ km were utilized with model tops at 0.1 hPa.

The study revealed that three (SLD, EUL and SE) out of the four CAM5 dynamical cores developed spontaneous QBO-like oscillations in the upper equatorial stratosphere. The SLD dynamical core shows a tropical zonal wind oscillation that is

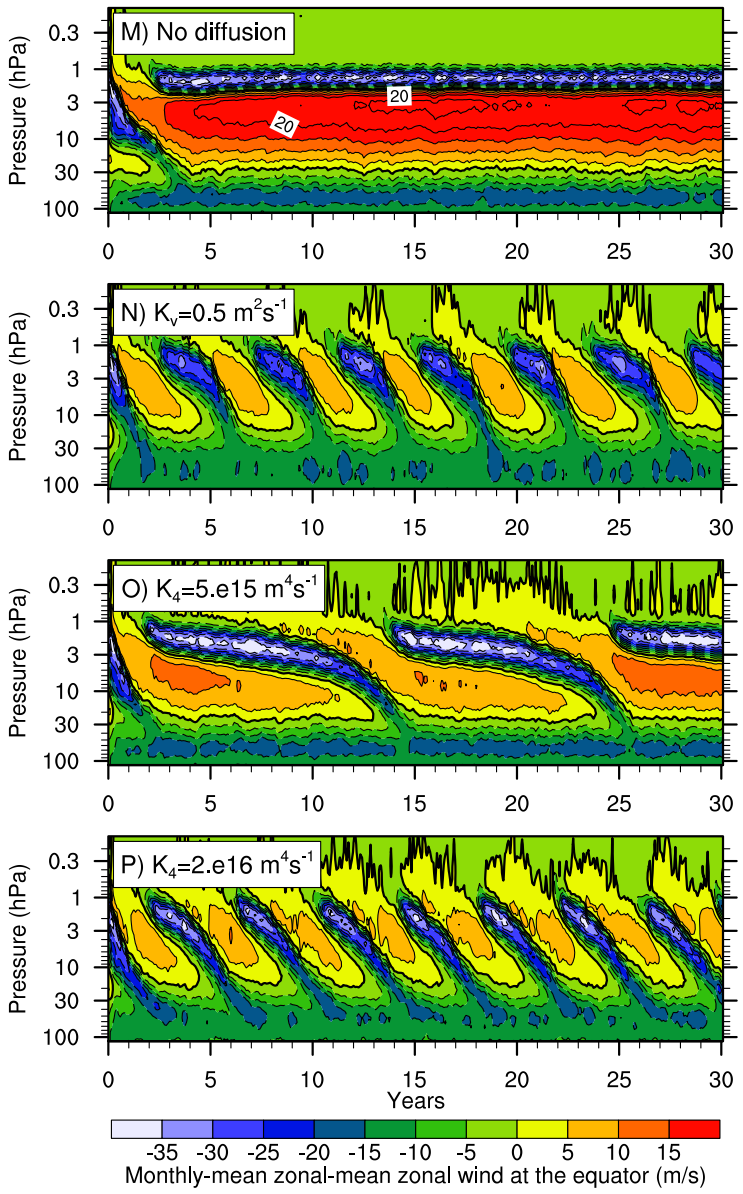

Figure 3.17: Zonal-mean monthly-mean zonal wind time-height cross sections averaged between 2° N/S in the SLD dynamical core with 67 levels and different diffusion mechanisms M) no diffusion, N) explicit second-order diffusion in the vertical K_v = 0.5 m^{2}s^{-1}, O) explicit 4th-order diffusion $K_4 = 5\times 10^{15}$ m^{4}s^{-1}, P) explicit 4th-order diffusion $K_4 = 2\times 10^{16}$ m^{4}s^{-1}.

closest to observation. However, the average period of SLD's QBO-like oscillation is 3.6 years, which is longer than observation, and covers the region between 1-50 hPa. The EUL and SE simulations closely resemble each other, but differ greatly from SLD. Their QBO periods are over 13 years, and the oscillation occupies the narrow band between 1-30 hPa. The QBOs lie too high in comparison to observations, but have realistic zonal wind magnitudes between -35 and 15 m s^{-1}. The FV dynamical core does not sustain the oscillation. The initial wind shear is dissipated within the first six years of the simulation.

The TEM analyses revealed that the E-P flux divergence (the resolved waves) is the dominant driver of the QBOs. However, the resolved wave forcing is strongly counteracted by the TEM residual, which represents the forcing by implicit numerical or explicitly-added diffusion and the damping via the thermal HS relaxation. The diffusive tendencies explain the gross features of the residual, and therefore play a considerable role in these idealized simulations. The analysis of the Brewer-Dobson circulation showed that the downward propagation of SLD's QBO is sped up by a mean descent in the QBO domain due to a strong secondary meridional circulation, whereas EUL's and SE's QBOs are slowed down by a mean ascent in the tropical stratosphere.

The wave analyses showed that waves are abundant in SLD's, EUL's and SE's tropical atmosphere despite the absence of moist convection as a typical wave trigger or a GWD scheme. The wave activity in FV and its E-P flux divergence are reduced. This raises questions about the wave generation mechanisms in dry HS experiments. We focused on dynamic instabilities as a potential wave triggering mechanism in the troposphere and wave dissipation process in the stratosphere. In particular, there are indications that the increased occurrences of strongly negative instability indicators in SLD, EUL and SE are related to their more vigorous wave activities and higher magnitudes of the resolved wave forcing in comparison to FV. This causality needs

further investigations which we plan to pursue in the future. This chapter focused on the dynamical core intercomparison aspects of the QBO investigation. The role of the horizontal and vertical grid spacings, diffusion mechanisms and their coefficients, sponge layer settings, as well as Brunt-Väisälä frequencies and thermal relaxation times in the stratosphere were partly discussed, but will be evaluated in greater detail in the future. In addition, we will shed light on the effects of simplified moisture processes and added gravity wave drag schemes on the QBOs in the dynamical cores, as demonstrated in Chapter V.

The periods and amplitudes of the oscillations are highly dependent on the details of the numerical schemes, the strengths of explicit vertical or horizontal diffusion, the horizontal and vertical resolutions and the characteristics of the sponge layer. The results suggests that the sponge layer (although located at 1 hPa above the QBO region) has downward impact on the QBO.

CHAPTER IV

Idealized Sudden Stratospheric Warmings in an Ensemble of Dry GCM Dynamical Cores

4.1 Introduction

In the winter stratosphere, the zonal-mean temperature field normally decreases from the tropics towards the pole. The zonal-mean zonal wind in the winter stratosphere is dominated by a westerly jet, peaking in the higher mid-latitudes, which is also called the "polar night jet". However, during some winters, the polar temperature occasionally increases rapidly with time, resulting in a poleward increase in the zonal-mean temperature and the breakdown of the westerly jet. The temperatures at the pole can increase by 40-60 K in a week at 10 hPa (*Andrews et al.*, 1987; *Schoeberl*, 1978). Such an event is called a sudden stratospheric warming (SSW). The event is considered a "major warming" if the zonal wind reverses to an easterly wind. In case the westerly flow does not reverse the SSW is called a "minor warming". According to *Charlton and Polvani* (2007), 31 SSWs (dependent on the detection criteria and datasets) happened in a 45-year period from 1958 to 2002.

The World Meteorological Organization (World Meteorological Organization (WMO)) definition of SSWs is based on the direction of the zonal wind at 10 hPa and 60° N/S. This criterion has been widely used over the past decades. However, the time series

of the Annular Mode (AM) is also suitable to define SSWs (*Baldwin*, 2003; *Gerber and Polvani*, 2009). The Annular Modes are defined as the north-south shifts of atmospheric mass between the polar regions and the mid-latitudes. Therefore the pressure anomaly has opposite signs between the polar caps and mid-latitudes. The variations of the strength of the polar vortex can be characterized by AM phases. The time series of the annular mode can be used as an index of SSWs instead of the zonal wind at 60°N/S and 10 hPa to avoid the possible inaccuracy that is induced by the latitudinal shift of the polar vortex.

SSWs are mainly generated and influenced by the upward propagation of the tropospheric planetary (Rossby) waves and their interactions with the stratospheric mean flow (*Matsuno*, 1971). Observations have suggested that the onsets of SSWs could be related to the atmospheric blocking events and the increased activities of easterly planetary waves (*Labitzke*, 1965; *Naujokat et al.*, 2002; *Wang and Alexander*, 2009; *Martius et al.*, 2009; *Woollings et al.*, 2010; *Vial et al.*, 2013). Especially the zonal wavenumbers $s = 1, 2$ are most important for the SSW forcing (*Matsuno*, 1971; *Holton*, 1976). Zonal wind deceleration due to wave breaking near the critical level causes the transition from westerlies to easterlies and the desent of the critical level. The polar jet is replaced by an easterly zonal-mean wind during SSWs. The easterly zonal wind blocks wave energy from further propagating upward and eventually reverses back to westerlies at a later stage of the SSW event (*Holton*, 1976).

Planetary waves have larger amplitudes in the Northern Hemisphere than in the Southern Hemisphere due to larger thermal and orographic forcing (*Andrews et al.*, 1987). The stratospheric waves generally propagate eastward in the Southern Hemisphere winter while both eastward and westward motions are present in the Northern Hemisphere winter (*Shiotani et al.*, 1990; *Chshyolkova et al.*, 2005). SSWs are much more frequent in the Northern Hemisphere than the Southern Hemisphere due to the weaker planetary forcing, the much lower temperatures and thereby stronger polar

vortex in the Southern Hemisphere (*Manney et al.*, 2005). Therefore, most of the previous even simplified simulations of SSWs are forced with topography in the Northern Hemisphere (*Naito et al.*, 2003; *Naito and Yoden*, 2006; *Gerber and Polvani*, 2009; *Sun et al.*, 2012).

SSWs are also modulated by the Quasi-Biennial Oscillation (QBO). According to *Holton and Tan* (1980), SSWs are more frequent during the easterly QBO phases, since planetary waves are then mostly confined to the mid-latitudes. This causes the planetary waves to have more interaction with the polar vortices (*Naito et al.*, 2003; *Naito and Yoden*, 2006; *Watson and Gray*, 2014). The variability of the polar vortex is not only influenced by the QBO. Various forcings such as the sea-surface temperature, the 11-year solar cycle, El Nino and La Nina events can also influence the polar vortex and the interactions between the QBO and the polar vortex (*Baldwin et al.*, 2001; *Wei et al.*, 2007).

Despite the fact that the influence of tropospheric activities on the stratospheric circulation has been known for decades, the influence of stratospheric events on the troposphere has only been assessed very recently (*Baldwin et al.*, 2001; *Gerber and Polvani*, 2009; *Hitchcock and Simpson*, 2014). *Baldwin et al.* (2001) stated that the SSW-induced pressure anomaly travels downward to the troposphere with a time scale of 30-60 days. These annular modes are known to modulate the surface weather systems, including the positions of mid-latitude troughs and ridges, tropical storm tracks, etc. Therefore, the processes in the stratosphere influence the probability and positions of extreme events near the surface. However, the mechanisms of this troposphere-stratosphere coupling are still unclear.

Most of the previous SSW studies with General Circulation Models (GCMs) used model setups with realistic topography and comprehensive physical parameterization packages. In order to understand the basic physical phenomena of SSWs and their interactions with the QBO and the troposphere, we simulate SSWs with a rather

simple model setup. The simulation uses only dry dynamical cores driven by Newtonian cooling and Rayleigh friction. The role of different numerical schemes is thereby investigated in this chapter.

The purpose of this chapter is twofold. First, we present a SSW simulation with a very simple setup which eliminates most of the natural variability that may influence SSW dynamics in nature. This provides a pure dynamical view of SSWs and their interaction with the QBO. Secondly we conduct an idealized dynamical core intercomparison in order to assess the impact of numerical schemes on the stratospheric circulation. This chapter is structured as follows The model descriptions are provided in Chapter 4.2. Chapter 4.3 presents the simulation results when using different dynamical cores. Chapter 4.4 investigates the SSW mechanisms using a variaty of wave analysis methods. Chapter 4.5 discusses the interactions of SSWs with the QBO and the troposphere. Chapter 4.6 shows a warm pole bias of the SLD dynamical core in this HSW simulations. Conclusions are provided in chapter 4.7.

4.2 Model Description and Experiment Setup

We utilize the Community Atmosphere Model (CAM) version 5, which has been developed by the National Center of Atmospheric Research. Four dynamical cores are used in this study: spectral transform semi-Lagrangian (SLD), Finite-Volume (FV), spectral transform Eulerian (EUL) and Spectral Element (SE). A detailed description of these four dynamical cores can be found in *Neale et al.* (2010). These dynamical cores have also been used in the related QBO study in Chapter III. The models have 55 vertical levels with a model top at 0.1 hPa using a hybrid $\sigma - p$ (also called η) vertical coordinate with variable vertical resolution. The vertical grid spacing is $\sim$ 0.2 km near the surface and increases with height in the troposphere. We select a constant 1.25 km grid spacing in the stratosphere between 100-3 hPa, and let the spacing increase to 2 km at the model top. The horizontal resolutions

for all dynamical cores are about 2°×2° or ∼220×220km in equatorial regions. This corresponds to the triangular truncation T63 in the spectral transform models SLD and EUL.

An idealized simulation with neither moisture, topography nor a seasonal cycle is utilized in this study. The SSW is simulated using the Held-Suarez-Williamson (HSW) forcing, which is a modification of the Held and Suarez (HS) forcing (*Held and Suarez*, 1994) in the stratosphere suggested by *Williamson et al.* (1998). The HS forcing consists of a Newtonian relaxation of the temperature field towards a prescribed equilibrium state and Rayleigh damping of low-level winds. These processes mimic the effects of radiation and boundary layer friction. However, the HS forcing was designed to keep the tropics and stratosphere passive. The HS is isothermal in the stratosphere, therefore has no typical stratospheric structures. The HSW forcing has the same setup as the HS forcing, only with a different equilibrium temperature profile in the stratosphere above 100 hPa.

The stratospheric equilibrium temperature T_{eq} in HSW is defined as (*Williamson et al.*, 1998)

$$T = T_0\Big[min\Big(1, \frac{p}{p_d}\Big)\Big]^{R\gamma_d/g} + T_0\Bigg\{\Big[min\Big(1, \frac{p}{p_i}\Big)\Big]^{R\gamma_i/g} - 1\Bigg\} \tag{4.1}$$

where $T_0 = 200$ K , $\gamma_d = 2$ K km^{-1}, R = 287 J K^{-1} kg^{-1}, g = 9.80655 m s^{-2} and γ_i = − 3.345 K km^{-1}. This temperature profile is depicted in figure 1.5. The first term is effective when $p \leq p_d$, and leads to a uniform decrease in temperature with height for all latitudes with lapse rate γ_d. The second term counteract the first term in the tropics which becomes effective when $p \leq p_i$, and causes a temperature increase with height with lapse rate $-\gamma_i$. The pressure threshold p_i depends on latitude ϕ and is defined as

$$p_i = p_{eq} - (p_{eq} - p_{pl})\frac{1}{2}\{1 + tanh[A(|\phi| - \phi_0)]\} \tag{4.2}$$

where $p_{eq} = p_d$, $p_{pl} = 1$ Pa, $\phi_0 = 60°$, $A = 2.65$ / $\Delta\phi_0$, and $\Delta\phi_0 = 15°$. In the original HSW setup, p_{pl} is set to 2 hPa. Here p_{pl} is modified to 1 Pa which coincides with the position of our higher model top.

We apply additional Rayleigh friction to the zonal wind field near the model top between $1 - 0.1$ hPa. A detailed description of this Rayleigh friction is described in Chapter III. The friction utilizes the damping time scale $1/K_r$ of about 41 days at 1 hPa and 2 days at 0.1 hPa.

4.3 SSW signals in different dynamical cores

4.3.1 SSW signals

According to the WMO definition of SSWs and most previous studies, we use the 60°N/S zonal-mean zonal wind to identify SSWs (*Charlton and Polvani*, 2007). Figure 4.1 shows the zonal-mean zonal wind at grid points that are closest to 60°N at 9.3 hPa for each dynamical core (60.62°N for SLD and EUL, 61° for FV and 60.47° for SE) and depicts instantaneous 6-hourly data for 30 years. The zonal winds around 60°N are typically westerlies. When the wind reverses during major SSW events, the wind speed drops below zero (crosses the 0 m s^{-1} line). Figure 4.1 shows that major warmings (events with zonal wind reversal) are observed for the SLD dynamical core about 12 times in the 30-year record. However, there are no major warmings in the other three dynamical cores (the one in FV before month 9 occurs during the spinup period of the model, therefore is not counted). Although the wind speeds for each dynamical core have strong fluctuations, we can observe that the SLD mid-latitude jet is weaker than the other three dynamical cores, followed by the FV simulation. The EUL and SE zonal winds are comparable with maxima around 45 m s^{-1} which are stronger than the FV and SLD maxima.

Figure 4.2 shows a 30-year record of the zonal-mean temperature at 9.3 hPa, near

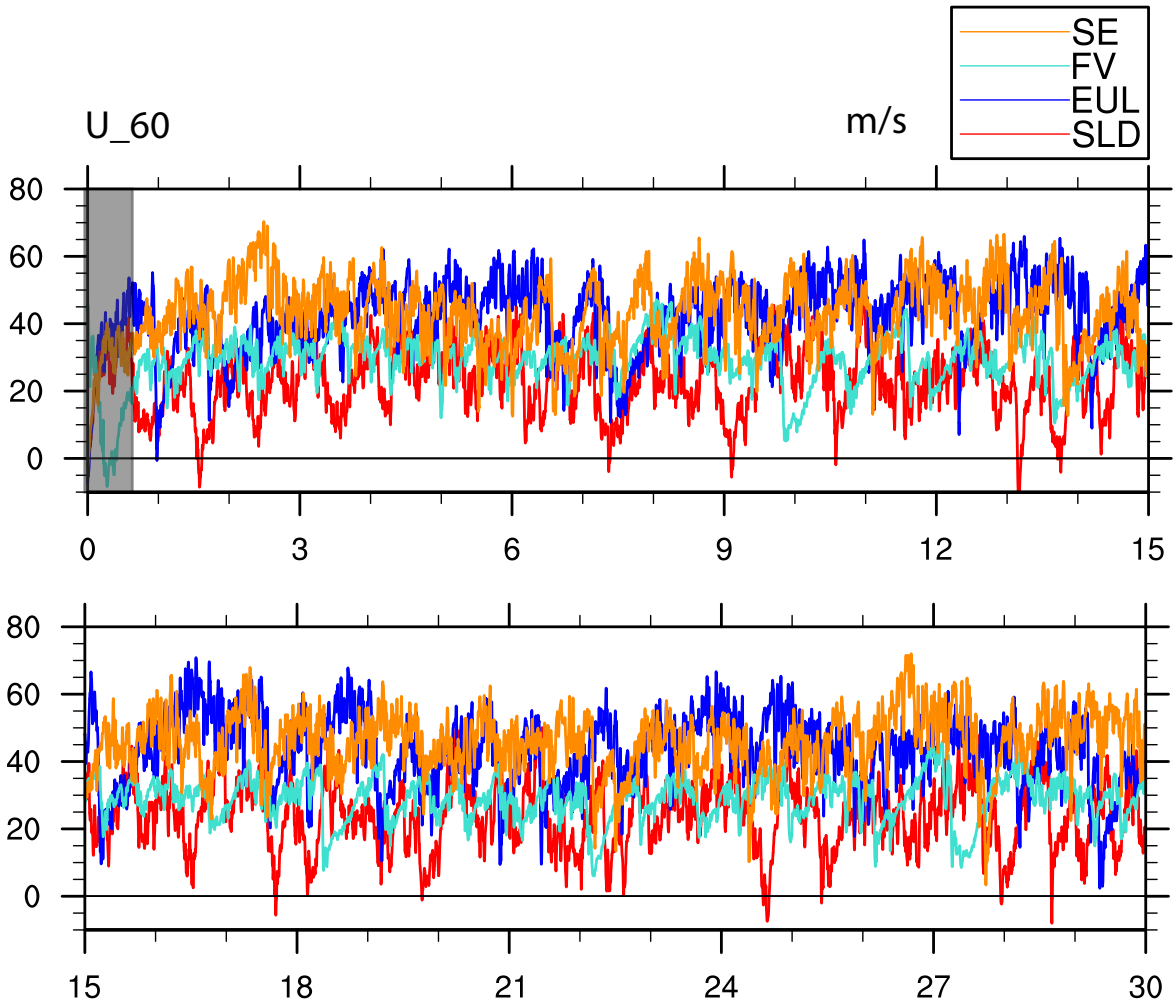

Figure 4.1: 30-year time series of the zonal-mean zonal wind at 60°-61°N 9.3 hPa for four dynamical cores (60.62°N for SLD and EUL, 61° for FV and 60.47° for SE). The spinup period is shaded in gray.

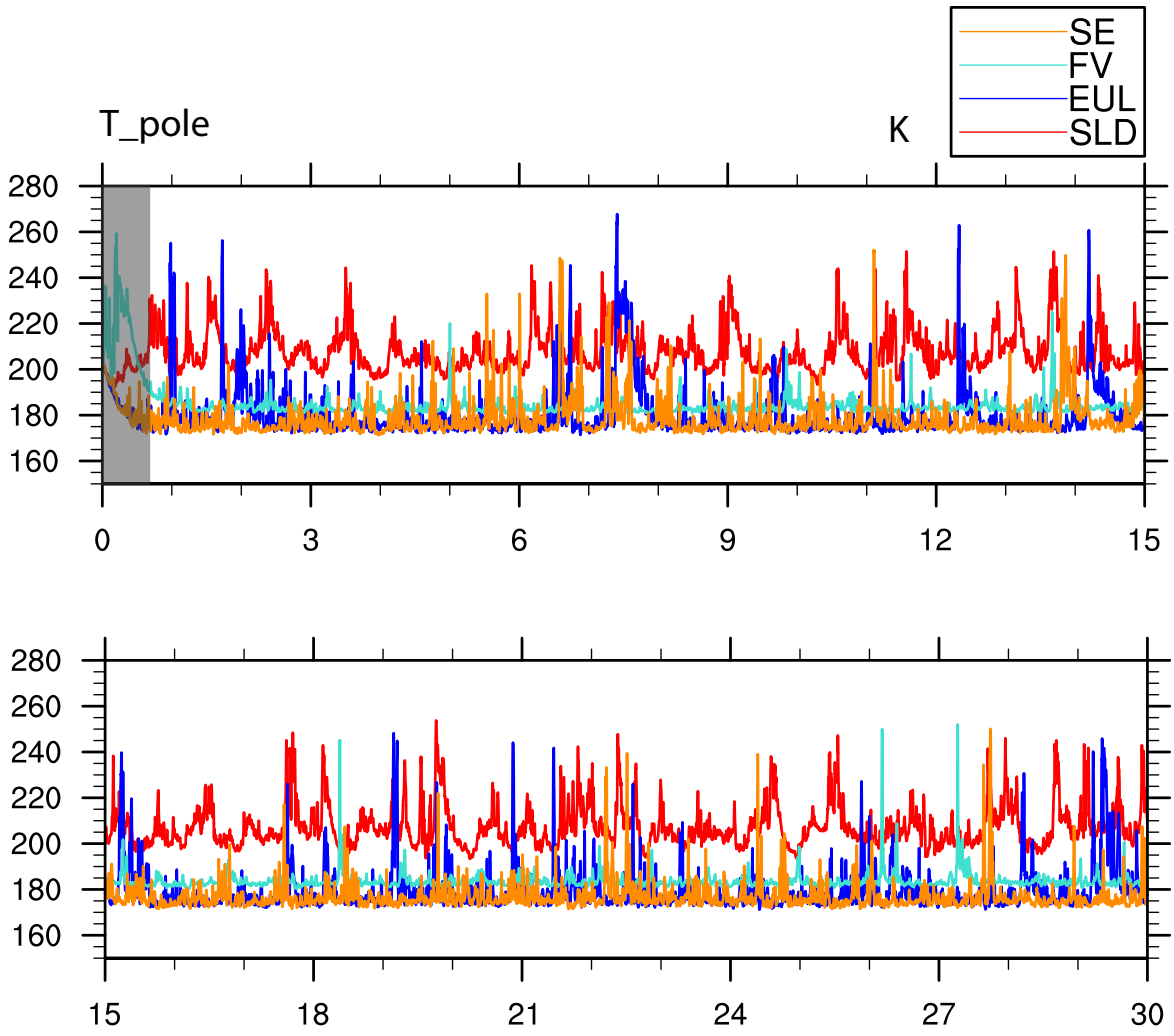

Figure 4.2: 30-year time series of the zonal-mean temperature near North Pole (88°-89°N) at 9.3 hPa (88.57° for SLD and EUL, 89°N for FV and 88.59°N for SE). The spinup period is shaded in gray.

the North Pole (88.57° for SLD and EUL, 89°N for FV and 88.59°N for SE) using 6-hourly instantaneous data. Most often, the polar temperature stays at a cold level, around 175K for EUL and SE, 185K for FV and 205K for SLD. This indicates that SLD has a much warmer polar temperature than the other three dynamical cores in the stratosphere. When SSW events occur, the pole temperature increases in a very short time. In the SLD simulation the temperature increases to about 250 K in some of the SSW events, with a temperature increase of around 45 K, and such events are quite frequent. In FV the warm phases can reach 245 K, therefore the polar temperature increases by about 60 K. The FV simulation has 5 minor warming events in the 30-year period. The SE simulation shows a polar temperature increase of around 70 K with a temperature maximum of about 245 K during the minor SSWs. The SE simulation has around 9 warming events. The EUL simulation has the strongest temperature increase of all simulations. The polar temperature reaches around 270 K during the minor SSW event between year 7-8. During other warming events in EUL, the temperature often reaches 250 K, which indicates a 75 K temperature increase in a short period of time. EUL exhibits 14 minor warming events in the 30-year period. A SSW statistic is provided in table 4.1.

Figure 4.3 shows the temperature gradient at 9.3 hPa, using the zonal-mean temperature at 60°N minus the zonal-mean temperature at the latitude circle closest to the North Pole ($T_{60} - T_{pole}$). The temperature differences between 60°N and the North Pole are mostly positive ($(T_{60} - T_{pole}) > 0$). However, during SSW events the temperature differences become negative ($(T_{60} - T_{pole}) < 0$) (*Krüger et al.*, 2005; *Charlton and Polvani*, 2007). In most of the events, the temperature difference drops for more than 50 K in a short period of time. The temperature gradient in SLD data is very different than the other three dynamical cores. The temperature differences are about 20 K for SLD but about 45 K for other three dynamical cores. Note that we discard the data from the first 8 months to eliminate the influence of the initial data during

Table 4.1: SSW statistics for different dynamical cores. Number of events, temperature increase during SSWs (Δ T) , and regular North Pole temperature (Tpole)

Dycore	# of Events	Δ T	Tpole
SLD	30	45 K	205 K
EUL	14	75K	175 K
FV	5	60 K	185K
SE	9	70 K	175 K

the model spinup period.

Also note that although the polar temperature increases drastically during SSWs, the zonal wind does not necessarily reverse. The zonal wind decreases prior to each warming event and continues to weaken after each event before the westerly jet is recovered.

4.3.2 Stratospheric circulations

The different SSW characteristics and their regular mean wind and temperature in the stratosphere in the four dynamical cores indicate that the climatic states differ greatly despite the identical HSW forcing. Figure 4.4 shows the pressure-latitude cross section of the 30-year mean zonal wind from the four dynamical cores. The tropospheric jets are similar in all dynamical cores, with maximum wind speeds around 30 m s^{-1} that are centered at around 40° N/S at 250 hPa. However, the stratospheric jets show significant differences. The SLD stratospheric polar jets have a maximum wind speed of 40 m s^{-1}. However, the polar jets in other three dynamical cores are about 70 m s^{-1}. The SLD stratospheric jets have a lower jet center at about 4-5 hPa, whereas the stratospheric jets center of the other three dynamical cores are at about 2 hPa. The FV simulation has a stronger easterly jet in the tropical and low-latitude stratosphere. This result is consistent with the FV simulation with the HS forcing in Chapter III. Consequently the easterly jet region is wider in the FV simulation compared to the other three dynamical cores; especially in the lower stratosphere

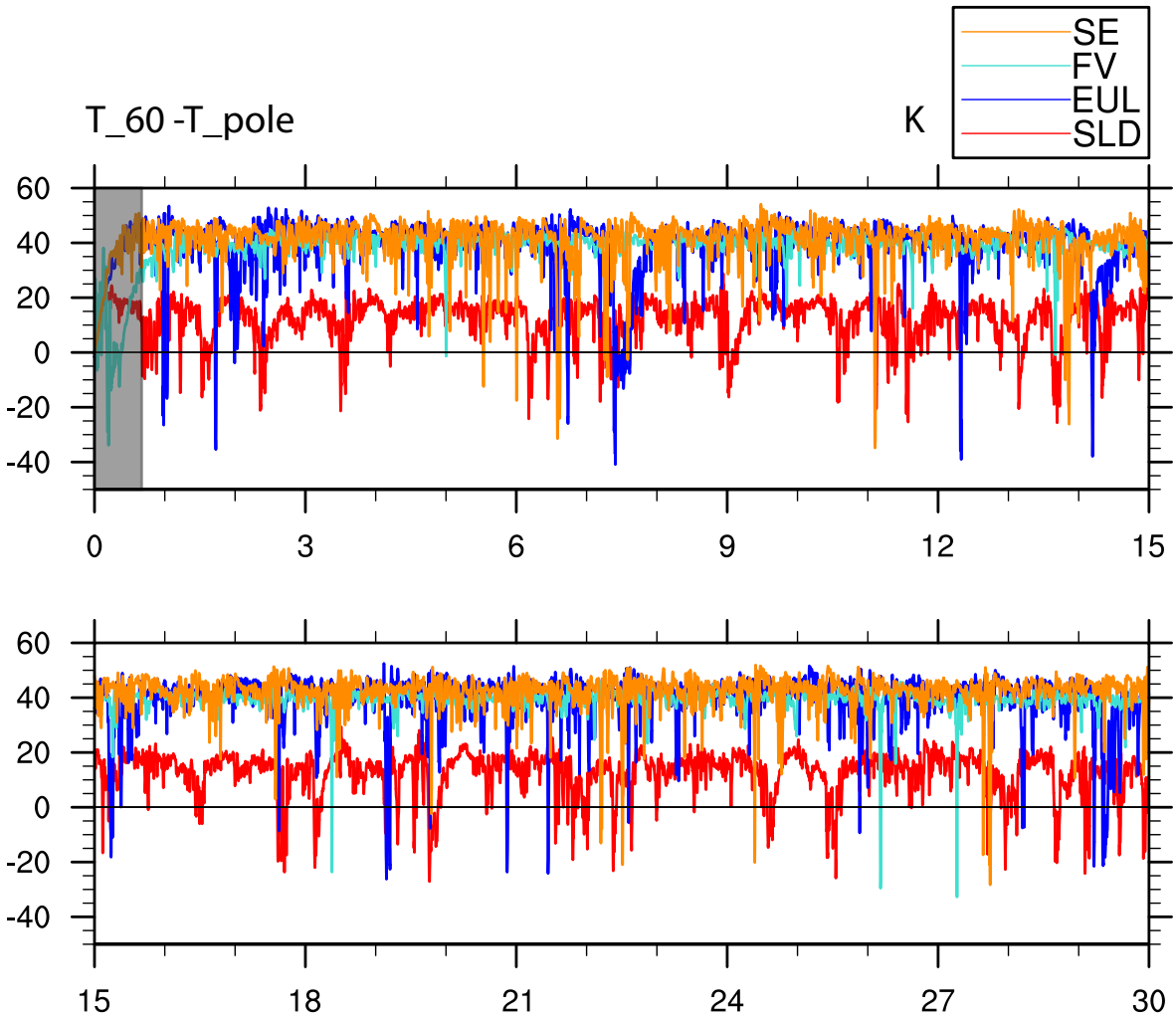

Figure 4.3: 30-year time series of the zonal-mean temperature gradient between the midlatitudes (60°-61°N) and the North Pole (88°-89°N) at 9.3 hPa. The spinup period is shaded in gray.

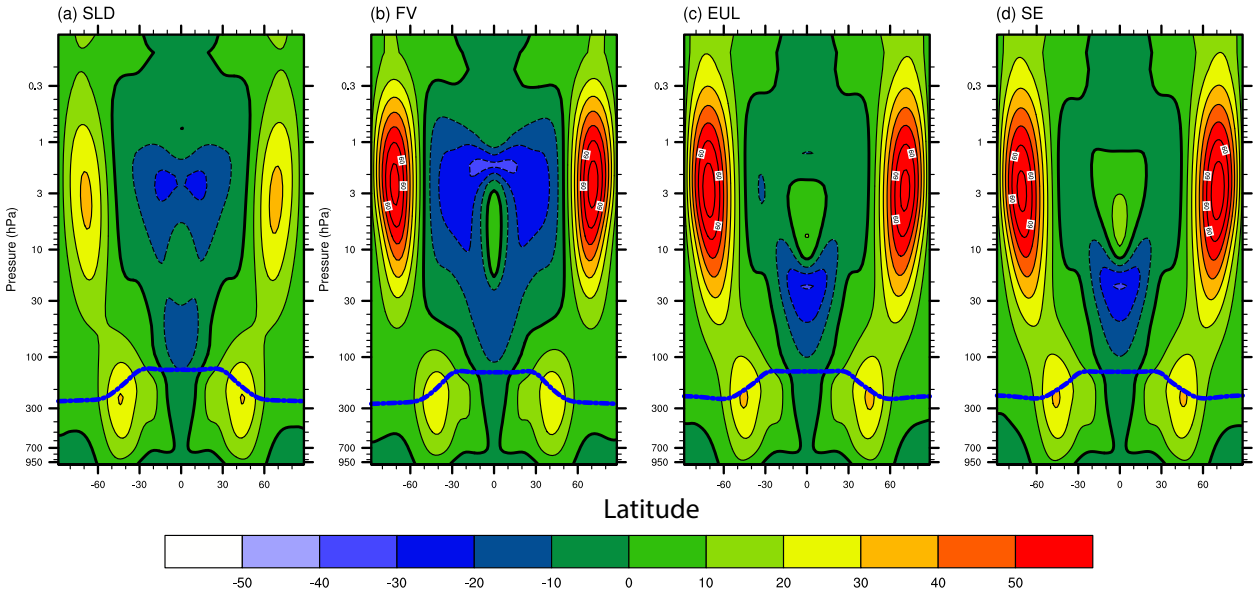

Figure 4.4: Pressure-latitude cross section of the 30-year mean zonal-mean zonal wind from different dynamical cores. a) SLD, b) FV, c) EUL and d) SE. The zero line is enhanced. Blue lines indicates the tropopause position of each simulation.

between 10-100 hPa. The 0 m s^{-1} lines in the FV simulation are at 50° N/S, but around 30° N/S for the other three dynamical cores.

The differences in the stratospheric jets are partially coming from the different temperature responses to the HSW temperature relaxation which is linked to the zonal wind via the thermal wind balance. The different wave-mean flow interactions in the dynamical cores also play a role in causing the differences in jet strength and position. In the tropical region of the stratosphere, the flow characteristics of the four dynamical cores also differ greatly as discussed in Chapter III. Besides the influence of the dynamical cores, the differences are also due to the specific QBO phases. The influence of the QBO on the stratospheric circulation and SSW events will be explained in Chapter 4.5.

The pressure-latitude cross sections of monthly-mean temperature fields from the four dynamical cores are presented in Figure 4.5. The latitudinal temperature gradient in the stratospheric mid-latitudes in SLD is very different from the other three

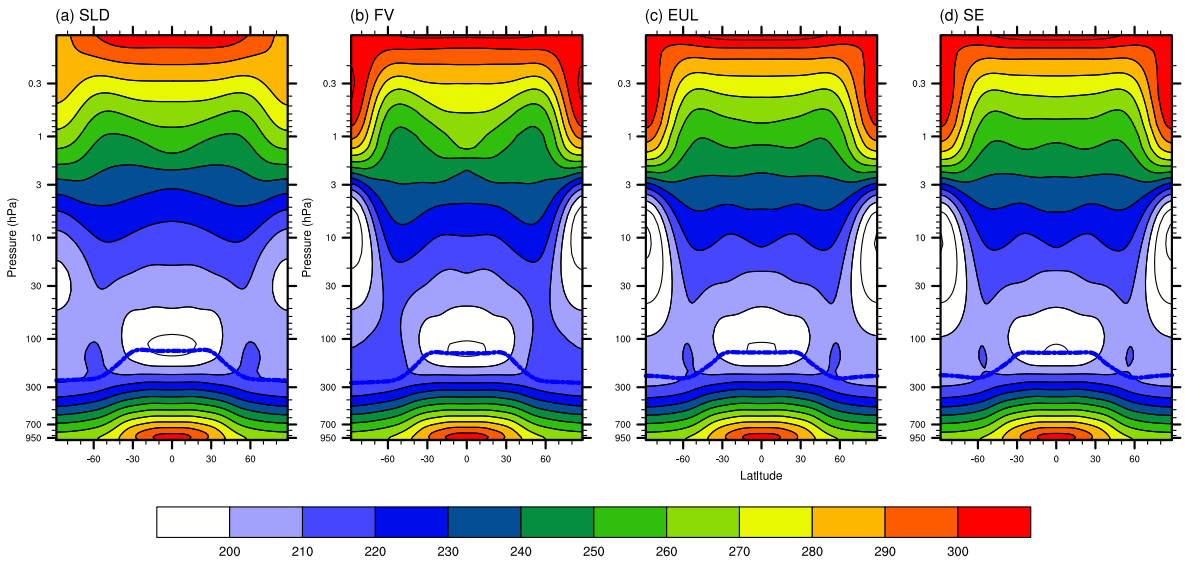

Figure 4.5: Pressure-latitude cross section of monthly-mean zonal-mean temperature field from different dynamical cores. a) SLD, b) FV, c) EUL and d) SE. Blue lines indicates the tropopause position of each simulation.

dynamical cores. The cold pole center in the lower stratosphere for the SLD simulation lies around 30 hPa with a minimum of 190 K, whereas it lies around 10 hPa with a minimum of 170 K in the other three dynamical cores. Strong positive pole to equator temperature gradients are observed in FV, EUL and SE above 3 hPa, but the gradient is much reduced in SLD. The FV simulation has a warmer stratosphere in the mid-latitudes. In particular, the SLD, EUL and SE temperatures at 100 hPa and 60° N/S are about 200 K, but only lie around 210 K in FV in the same region. This results in a larger latitudinal temperature gradient in the FV simulation in the mid-latitudinal stratosphere, which creates stronger easterly jets (Figure 4.4b).

Overall, SLD has more frequent SSW events than the other three dynamical cores. SLD's stratospheric mid-latitudinal zonal wind jets are weaker and their latitudinal temperature gradients are also weaker than the other three dynamical cores. The reasons why SLD behaves differently in the stratosphere in comparison to the other

three dynamical cores are not completely clear. However, we explore some potential reasons from both the numerical and physical points of views in chapter 4.6. The differences are analyzed and compared in the following sections.

4.4 Wave Analysis

In this section, we mainly focus on the wave activity during the life cycles of SSWs. Previous research on SSW has been focused on the precursors in order to enhance the SSW predictability (*Sun et al.*, 2012; *Naujokat et al.*, 2002). To assess the SSW precursors, we have to understand the initiation mechanisms of SSWs. The initiation mechanisms are mostly affected by planetary wave activities. Observational data have shown that planetary waves with zonal wavenumber 1 and 2 play an important role in SSW initiation (*Naujokat et al.*, 2002). Moreover, anomalous upward Eliassen-Palm (E-P) fluxes from the troposphere into the stratosphere are observed right before SSWs or during the early stages of SSWs (*Sun et al.*, 2012; *Limpasuvan et al.*, 2004). In our model simulations the stratospheric polar vortex always recovers after each SSW events since there are no seasonal differences in the mean states. However, in reality the recovering mechanisms depend on the time of the year, e.g. a collapsed polar vortex does not recover if the warming happens in spring, which is called the stratospheric final warming (*Sun et al.*, 2011). Such cases are beyond the scope of this idealized study without seasonal cycles. In this section we analyze the wavenumber 1 and 2 activity to study the SSW initiation processes. Transformed Eulerian Mean analysis is also used to study the wave-mean flow interaction.

4.4.1 Wavenumber 1 and 2 activities

Between year 6-7, there are several temperature reversals at 10 hPa that occur both in SLD and EUL (Figure 4.3). They are accompanied by large temperature gradient ($T_{60} - T_{pole}$) changes during a short period of time.

Figure 4.6 shows the Hovmöller diagrams of the wavenumber 1 and 2 components from the temperature anomaly (deviations from the zonal-mean) at 60°N using a fast Fourier transform method at 1hPa and 10 hPa for both SLD and EUL. In SLD, westward wavenumber 1 components are observed during most of the time at both the 1hPa and 10 hPa levels, with enhanced wave amplitudes around the SSW events. Eastward activity sets in after the SSW event which helps recover the polar vortex. For wavenumber 2, we observe quasi-stationary waves between year 6.60-6.70 and 6.90-7.00 at both 1hPa and 10 hPa, which suggests that stationary waves can be produced without topography. The wavenumber 2 components turn westward before and after the SSW event. *Naujokat et al.* (2002) observed similar phenomena in their analysis for the December 2001 major warming.

Figure 4.6 c) and d) shows the same analysis for EUL. Westward wavenumber 1 components are observed throughout the whole time, the wave amplitude enhances before and during the SSW event. Enhanced westward wavenumber 2 components are also observed before and after the SSW onset. Overall, the wave amplitudes in EUL around this SSW event are higher than the wave amplitudes in SLD. This indicates stronger planetary waves in the EUL than the SLD simulation which leads to stronger wave-mean flow interactions. This is one of the reason that we observe higher temperature changes during SSW events in EUL than in SLD.

4.4.2 Transformed Eulerian Mean analysis

Figure 4.7 shows the Eliassen-Palm (E-P) flux during the life cycle of a sudden stratospheric warming event in SLD. From left to right the figure depicts the early stage, mature stage, and recovering stage of an SSW event. The arrows are scaled E-P flux vectors. In particular we scale the vectors using

$$(\tilde{F}_\phi, \tilde{F}_p) = (1000.0hPa/p)^{0.5} \times cos\phi \left(\frac{1/a * F_\phi}{s_\phi}, \frac{F_p}{s_p} \right) \tag{4.3}$$

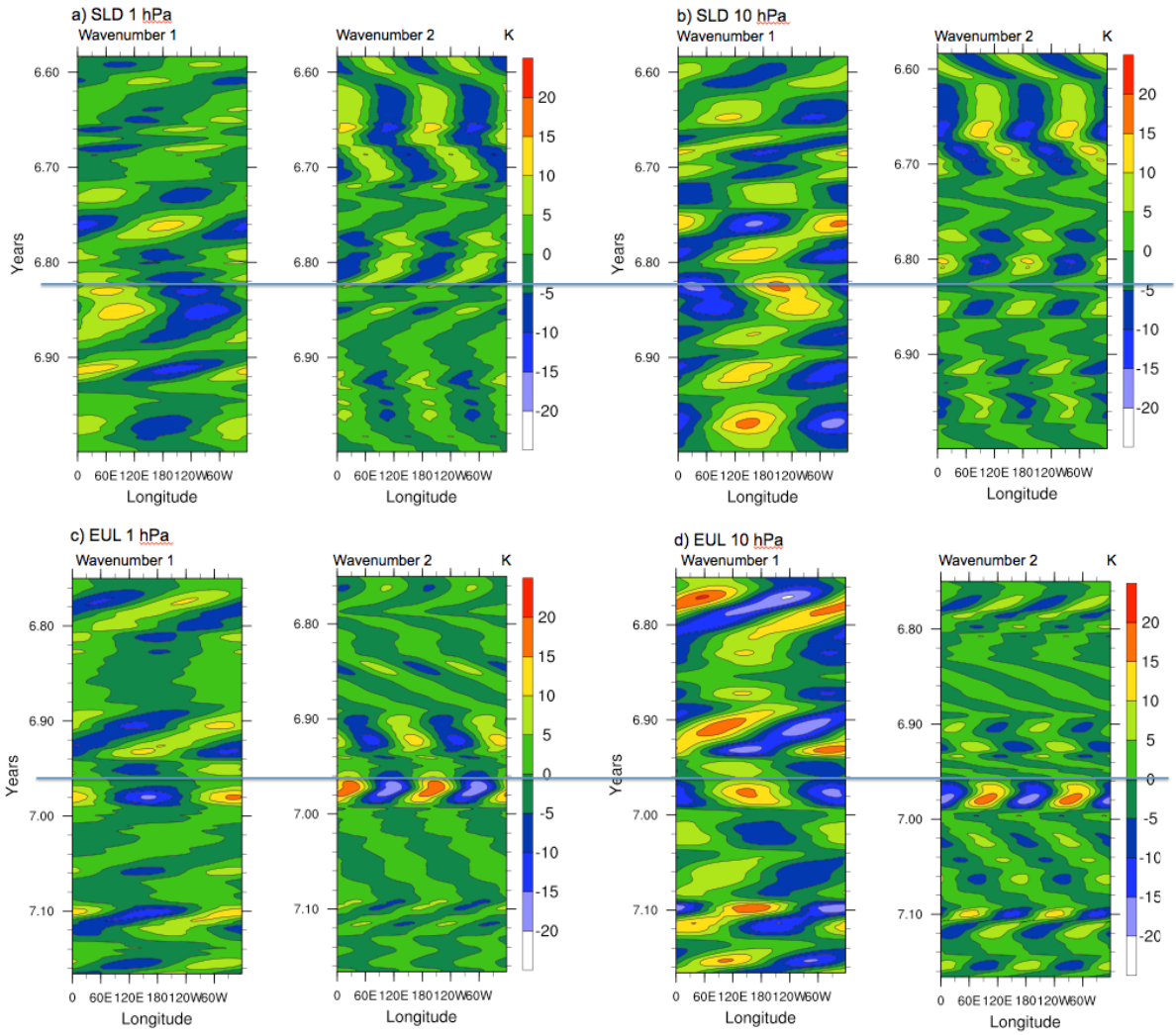

Figure 4.6: Hovemöller diagram for wavenumber 1 and 2 in SLD (a, b) and EUL (c, d) at different levels (1hPa (a, c) and 10 hPa (b, d)). The result is obtained from Fourier analysis using 6-hourly temperature anomalies at 60°N. The blue line indicates the onset of an SSW event.

where F_ϕ, F_p are the horizontal and vertical components of the E-P flux, $\tilde{F}_\phi$, $\tilde{F}_p$ are the scaled E-P flux vector, a is the earth radius, $s_\phi = \pi$ (radians) and $s_p = 10^5$ (Pa). The background contours are the scaled divergence of the E-P flux, with negative values dashed, the values above 100 hPa are multiplied by a factor of 2. This method is widely used (e.g. *Taguchi and Hartmann* (2006)). The E-P flux here is calculated using the quasi-geostrophic approximation (*Edmon et al.*, 1980).

During the early stage of the SSW (figure 4.7a), the divergence of the E-P flux is negative in the stratosphere. This means the acceleration due to wave-mean flow interaction is westward, which weakens the polar vortex. At this time, the E-P flux vectors are upward with high magnitudes in mid-latitudes, indicating upward tropospheric wave fluxes.

During the mature stage (figure 4.7b), the divergence of the E-P flux is weakened in the stratosphere, but still negative, which weakens the westerly jet or even accelerates the now easterly polar jet in SLD. The E-P flux vectors have lower magnitudes as compared to the early stage, which indicates a reduced upward propagation of momentum flux. During the vortex recovering stage (Figure 4.7c), the divergence of the E-P flux turns positive (eastward) again in the stratosphere, with upward wave fluxes. Similar life-cycles are also observed in reanalysis data (*Limpasuvan et al.*, 2004).

In order to compare the wave-mean flow interaction in different dynamical cores, we perform a long term TEM analysis of all four dynamical cores using the method described in Chapter III. Figure 4.8 shows the 30-month mean zonal-mean divergence of the E-P flux at different levels in the four different dynamical cores. The positive (negative) values indicate eastward (westward) wind accelerations. At 500 hPa in Figure 4.8 a), the wave accelerations in the mid-latitudes are similar in all dynamical cores. The maximum westward acceleration is located around 55°N/S. The magnitude of the westward acceleration is similar in SLD, EUL and SE, but weaker in the FV

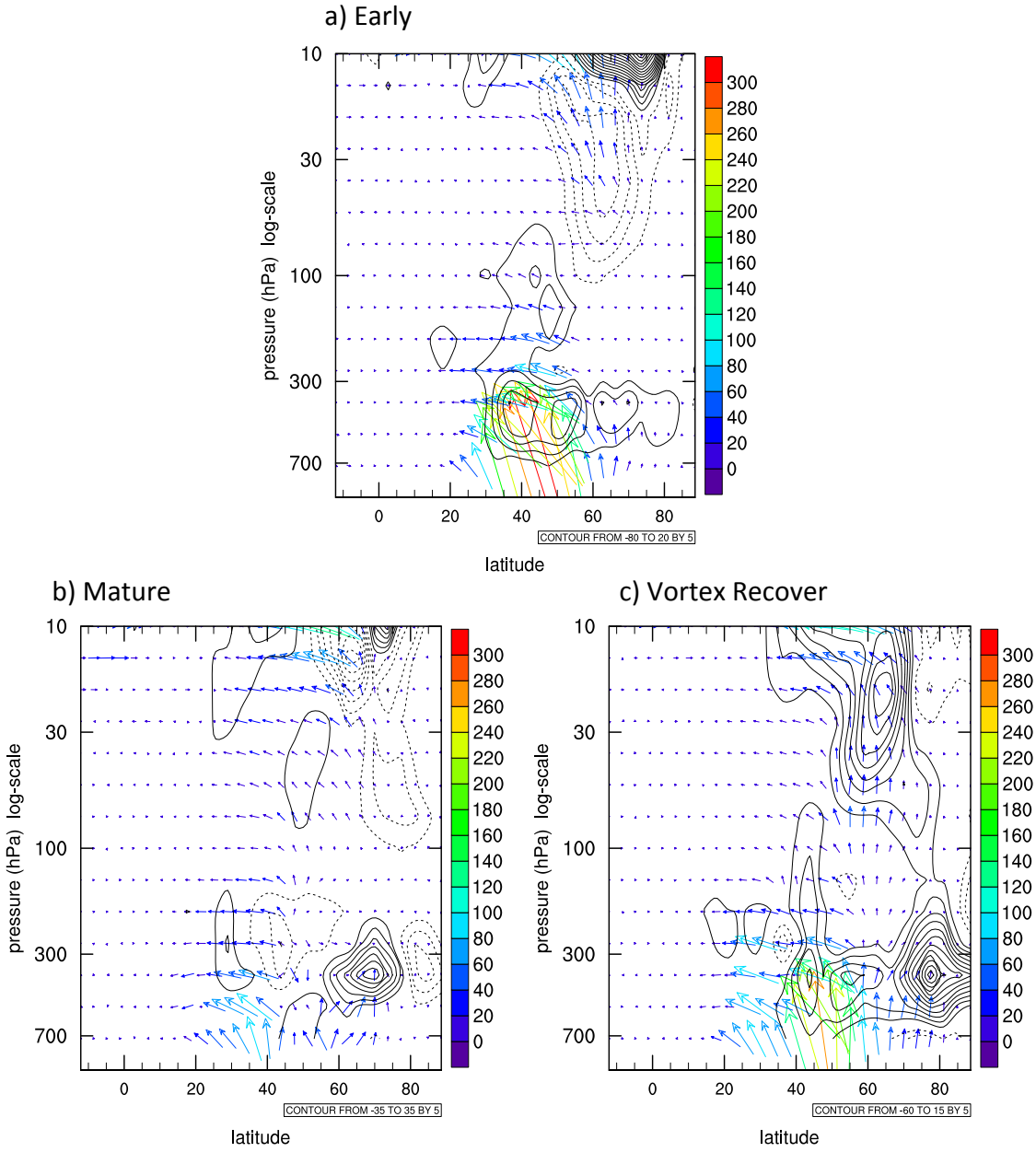

Figure 4.7: Wave-Mean flow interaction analysis using the Transformed Eulerian Mean (TEM) analysis (1 day average) using 6-hourly data from the SLD simulation. Vectors show scaled Eliassen-Palm (EP) flux vectors, the background contour shows the scaled divergence of the EP-flux in m/(s day) with contour interval 5 m / (s day) (negative contours are dashed). a) TEM analysis during one of the early days of an SSW event in the Northern hemisphere (around year 6), b) mature stage of the SSW event, c) recover stage of the polar vortex.

.

simulation.

In figure 4.8 b) at 100 hPa, the westward (negative) wind acceleration in SLD is significantly stronger than that in the other three dynamical cores. The maximum westward acceleration lies at approximately 40 °N/S. Figure 4.8 c) shows that the westward wind acceleration in SLD is about twice as strong as the EUL TEM forcing at 10 hPa, and around three times as strong as FV and SE. The maximum westward acceleration lies around 60 °N/S.

This TEM analysis shows that the SLD simulation has stronger average westward wind acceleration in the mid-latitudes than the other three dynamical cores. This westward wind acceleration decelerates the westerly jets in the stratospheric mid-latitudes. The higher wave-mean flow interaction in the lower stratosphere is another reason for weaker westerly jets in the SLD simulation, in addition to its lower latitudinal temperature gradients.

4.5 SSW interactions

4.5.1 Troposphere-Stratosphere Interaction

Recent research has demonstrated that the coupling between the stratosphere and troposphere is strong during winters and that some stratosphere anomalies are linked to surface weather (*Baldwin and Dunkerton*, 2001). However, the mechanism of this coupling is not completely understood. *Charlton and Polvani* (2007) stated that the coupling is observed primarily during winter and early spring when the polar vortex is most variable. *Baldwin and Dunkerton* (2001) noted that the weakening/strengthening of the stratospheric polar vortex is associated with an equatorward/poleward shift of the tropospheric extratropical jet. Therefore, the Annular Mode (AM) pattern can represent the strength of the stratospheric polar vortex. Meanwhile, the AM index, which characterizes the jet shift, has become an alter-

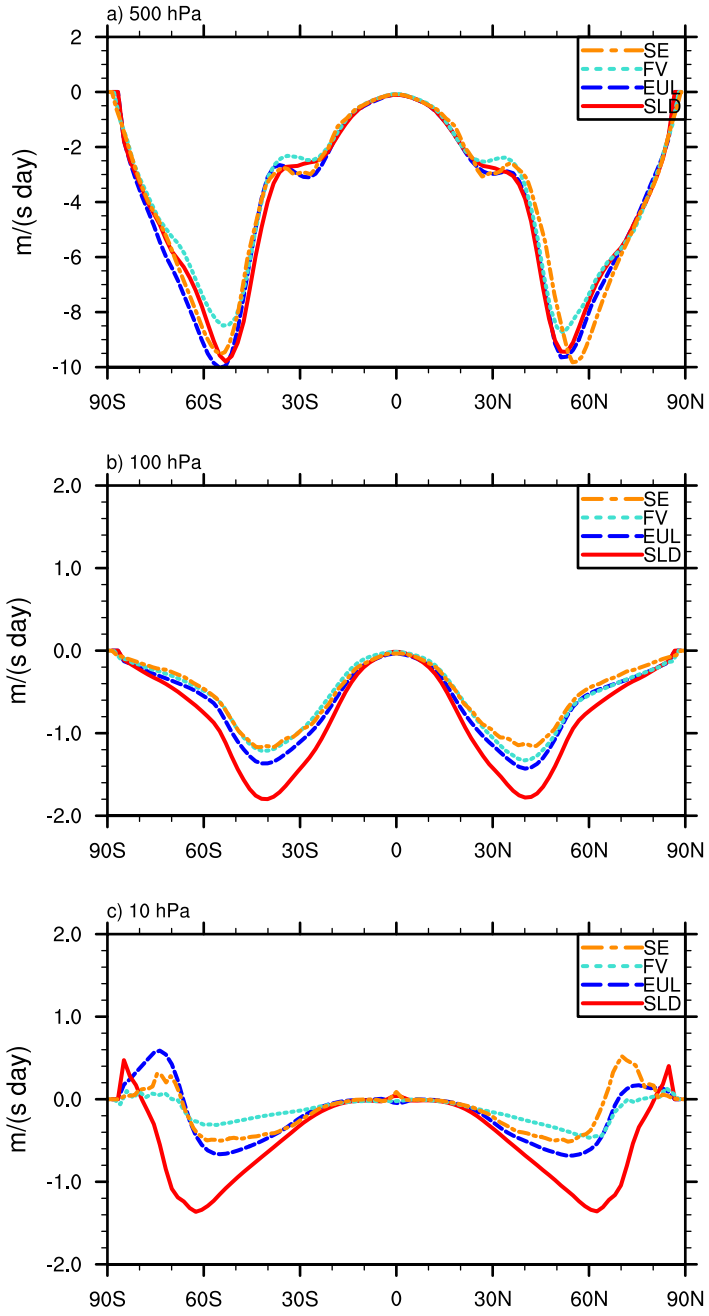

Figure 4.8: Wave-mean flow interaction analysis using the Transformed Eulerian Mean (TEM) analysis. 30-month-mean zonal-mean divergence of the unscaled E-P flux at a) 500 hPa, b) 100 hPa and c) 10 hPa, in m/(s day)

native way of detecting the stratospheric polar vortex changes. In particular, the Northern Annular Mode (NAM) index is used in the northern hemisphere. *Baldwin and Dunkerton* (2001) found that a weak stratospheric vortex, corresponding to a negative NAM index, tends to travel downward and shifts the surface annular mode index, thereby influencing the surface climate and weather systems.

In nature, the signals are influenced by numerous factors including El Niño and Southern Oscillation (ENSO), the 11-year solar cycle and others. The NAM pattern is also influenced by the topography and land sea contrast. *Gerber and Polvani* (2009) examined the stratosphere-troposphere coupling with an idealized GCM setup following the *Polvani and Kushner* (2002) forcing approach with idealized topography. The *Polvani and Kushner* (2002) forcing is similar to the HSW forcing and uses a temperature relaxation to mimic the radiative forcing. However, the *Polvani and Kushner* (2002) forcing prescribes a perpetual winter condition and is therefore not symmetric about the equator. *Gerber and Polvani* (2009) assessed a slightly more complex setup than ours and achieve similar results. We now evaluate how the stratosphere-troposphere coupling is represented in our even more idealized setup in comparison to *Gerber and Polvani* (2009).

Figure 4.9 shows an Empirical Orthogonal Function (Empirical Orthogonal Function (EOF)) analysis of the North Hemisphere geopotential height anomaly field using 6-hourly instantaneous data for the first 20 years of the SLD simulation. Figure 4.9 shows the first and second leading components of the EOF analysis at 10 hPa. We observe a highly zonally symmetric annular mode pattern in the leading EOF component which characterizes the polar vortex. This component explains 22.9% of the total variation, and is higher than observations. This zonal symmetry and high percentage is expected in a simulation with the idealized zonal symmetric forcing. We also observe a zonal wavenumber 1 pattern in the second leading EOF component which explains 18.5% of the total variance.

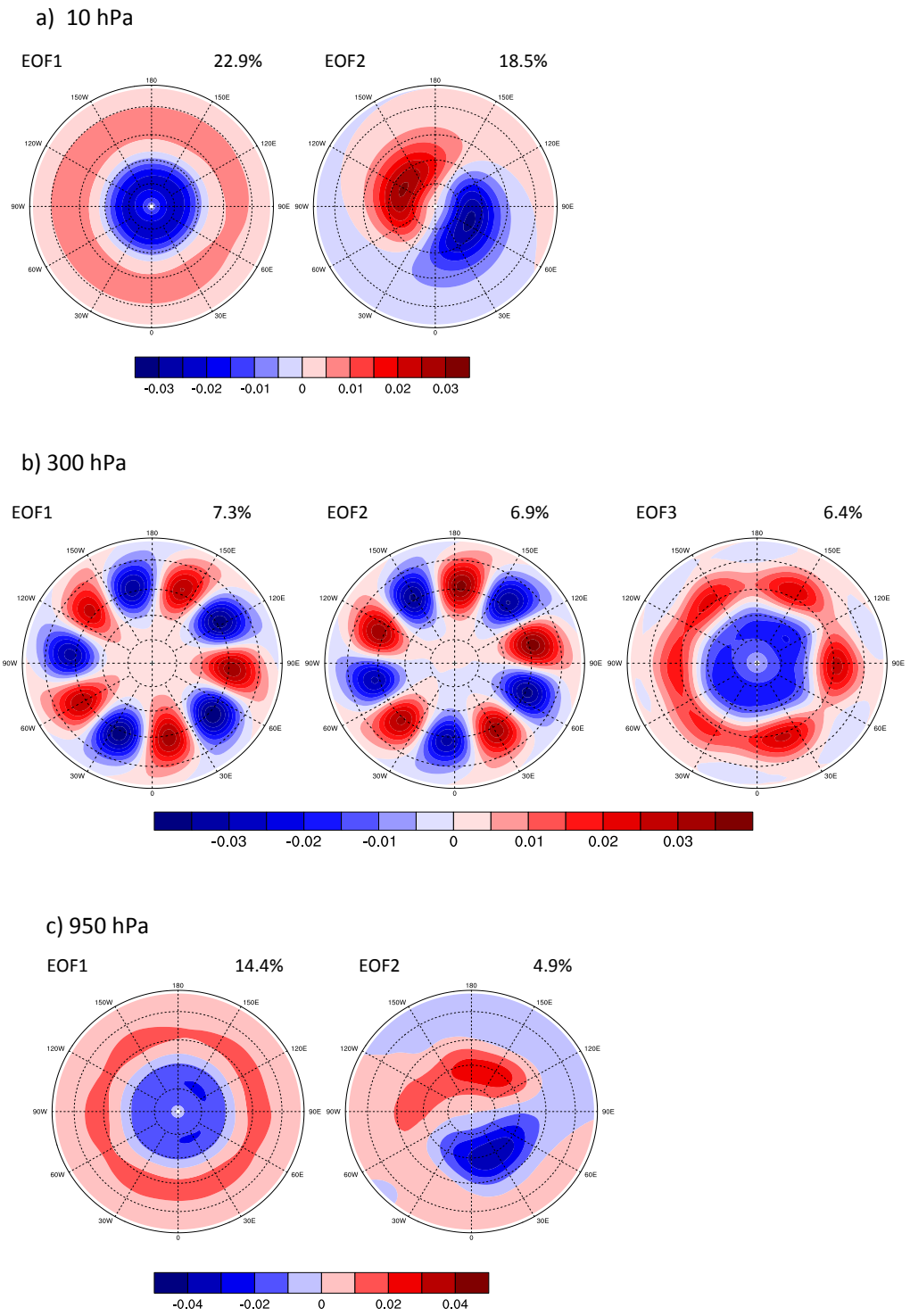

Figure 4.9: Empirical Orthogonal Function analysis on the 6-hourly instantaneous geopotential height anomaly field in Northern Hemisphere for the first 20-year SLD simulation at different levels. a) 10 hPa first and second leading components, b) 300 hPa first three leading components and c) 950 hPa first and second leading components.

Figure 4.9b shows the same EOF analysis at 300 hPa. We are able to observe a zonal wavenumber 5 pattern in the first and second EOF component which explains 7.3% and 6.9% of the total variation. This pattern cannot be seen in observations due to the disturbances induced by topography. The Annular Mode pattern is present in the third leading EOF, with a combination of a zonal wavenumber 6 pattern. These zonal wavenumbers 5 and 6 represent planetary waves that are observed in mid-latitudinal jets and are also an internal variation of the Earth atmosphere. These wavenumber 5 and 6 features are most common in our idealized simulation between 200-400 hPa at the levels where the tropospheric extratropical jets are strongest.

Figure 4.9c at 950 hPa shows an Annular Mode pattern for the leading EOF component (14.4%) and a zonal wavenumber 1 pattern (4.9%) for the second leading EOF component. The overall feature is similar to the 10 hPa plot but with a lower percentage. This is due to the relatively strong disturbances at the surface.

Overall, the EOF analysis shows a highly zonally symmetric pattern in this idealized simulation. We are able to detect several internal variabilities of the Earth's atmosphere using this tool. The planetary waves dominate the atmospheric variation at the levels where the tropospheric extratropical jets are strongest and the Annular Mode dominates the atmospheric variation in all other levels in both the stratosphere and lower troposphere.

We also examined the downward propagation of the time series. Figure 4.10 shows a SSW warming composite of the NAM time series (the third leading EOF components are chosen in levels between 200 - 500 hPa). We used the following SSW detection criteria of the normalized NAM time series at 10 hPa. The normalized NAM index must be less than 2.0 for a 10-day time span and must reach a local minimum. There should also be no other local minimum 15 days before and after the local minimum, otherwise it counts as a same event. Figure 4.10 shows a downward trend of the EOF time series 30 days after the central date (SSW) of the composite.

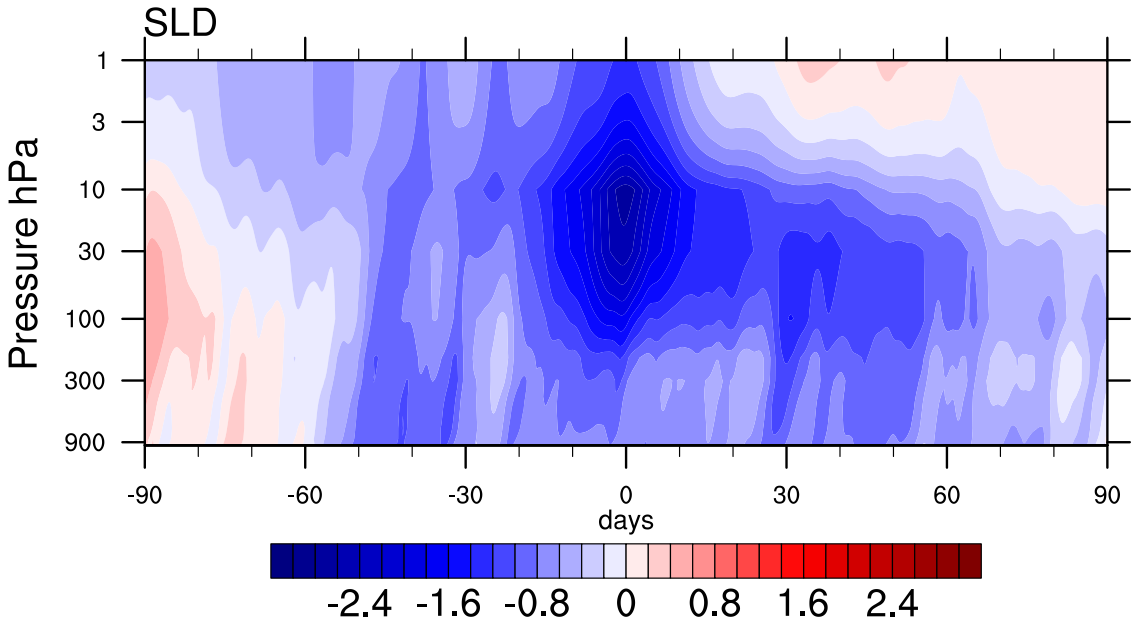

Figure 4.10: SSW composites of the annular mode time series in SLD. Normalized time series from Empirical Orthogonal Function analysis of geopotential height. 15 events are detected from a 20-year 6-hourly data. SSWs have downward impact on the troposphere.

However this trend is weaker than that shown in *Baldwin and Dunkerton* (2001) and *Gerber and Polvani* (2009). This is mainly due to the lack of planetary waves that are triggered by topography. *Gerber and Polvani* (2009) argued that the coupling between the stratosphere and troposphere during and after SSWs is mainly due to eddy momentum flux convergence. In an idealized simulation without topography as a major wave triggering mechanism, the eddy momentum flux is supposed to be weaker. However, we are able to simulate the same phenomenon without topography, which suggests that such coupling is also an internal property of the Earth's atmosphere.

4.5.2 SSW and QBO

Other than influencing the troposphere, SSWs also interacts with the tropical regions in the stratosphere. According to *Holton and Tan* (1980), a SSW is strongly modulated by the QBO phase. During an easterly QBO phase, the upward traveling

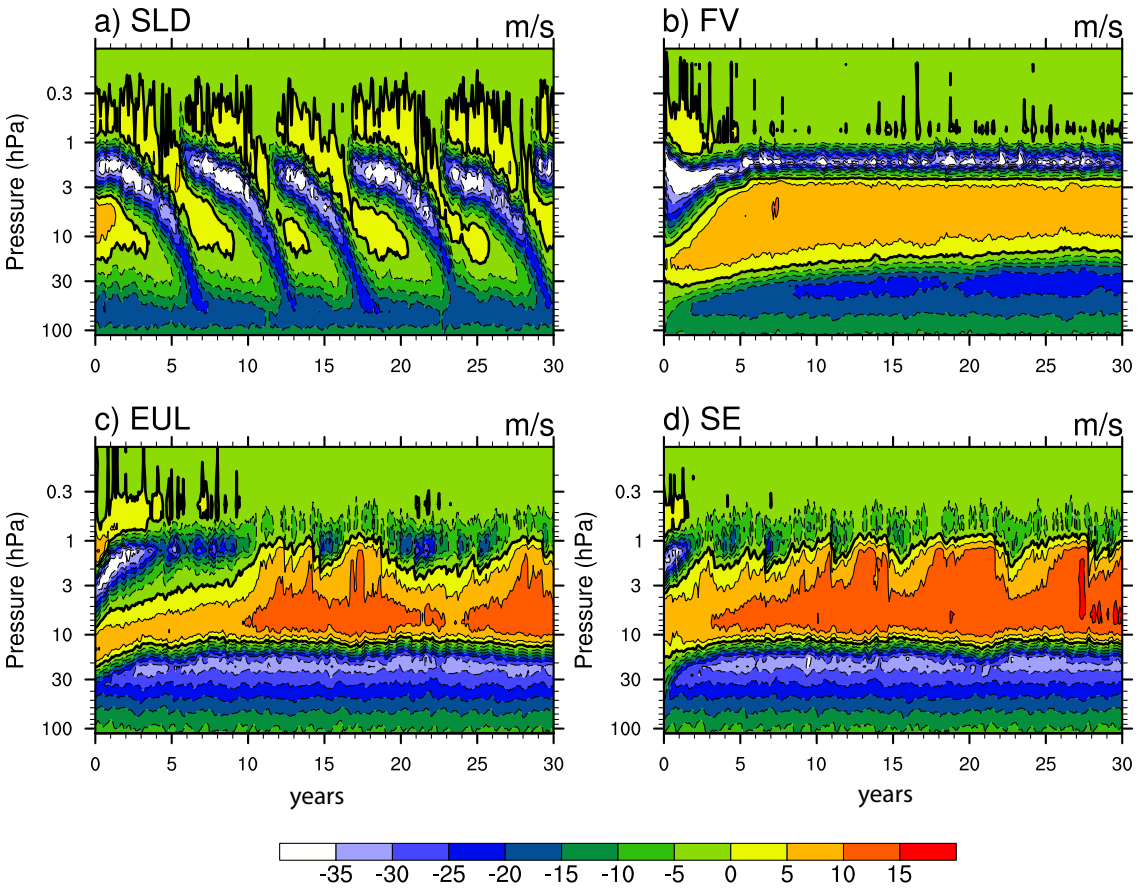

Figure 4.11: 30-year monthly-mean zonal-mean zonal wind at the equator from different dynamical cores, averaged between ±2°, in m s^{-1}. a) SLD, b) FV, c) EUL and d) SE.

planetary waves in the mid-latitudes are confined to the mid-latitudes (*Naito et al.*, 2003). Therefore, SSWs are more likely to be triggered during easterly QBO phases. However, in a recent study by *Garfinkel et al.* (2012) the QBO is more likely to modulate the meridional circulation which will further influence the polar vortex.

Figure 4.11 shows the 30-year monthly-mean zonal-mean zonal wind at the equator for different dynamical cores. Figure 4.11a shows the zonal wind of the SLD dynamical core simulation with the HSW forcing. A QBO-like oscillation with a period of 6 years occupies the vertical domain between 0.3 - 50 hPa. The oscillating wind amplitude is -35−5 m s^{-1}. The HSW simulation has a longer QBO period than the HS simulation

discussed in Chapter III, with a weaker westerly wind.

Figure 4.11b shows the zonal wind of the FV simulation. The FV simulation is not able to establish a QBO-like oscillation. An easterly jet with maximum wind speed of -35 m s^{-1} occupies the levels between 1-3 hPa, and a westerly jet occupies the levels between 3-30 hPa with a wind speed of 5 m s^{-1}. Another easterly jet is apparent in the lower stratosphere between 30-100 hPa with a wind speed of - 20 m s^{-1}.

Figure 4.11 c) and d) depict the zonal wind in the EUL and SE simulations. The simulation results for EUL and SE are very similar. These are not able to establish a QBO-like oscillation within this 30-year simulation period. A westerly jet with an amplitude of about 10 m s^{-1} occupies the region between 1-10 hPa and an easterly jet with $\sim$ - 30 m s^{-1} occupies the levels between 10 and 70 hPa.

Compared to the HS simulations with an isothermal equilibrium temperature in the stratospheric (Chapter III), the QBO periods are longer in the SLD dynamical core, and EUL and SE lost their QBO-like patterns. The reason for this is the inclusion of the stratospheric polar vortices which are triggered by the stratospheric mid-latitude temperature gradients in the *Williamson et al.* (1998) modified temperature profile. Also note that the HSW simulations have stronger and more realistic Brewer-Dobson circulations than the HS experiments shown in Chapter III. The increased upwelling induced by the Brewer-Dobson circulation in the tropics plays a counteracting role and slows the downward QBO propagation speed (*Baldwin et al.*, 2001). Therefore the net momentum budget is decreased with the inclusion of the polar vortex, leading to a weaker QBO with longer periods.

The area-weighted zonal-mean 30-month mean residual vertical pressure velocity ($\bar{\omega^*} \times cos\phi$), that represents the Brewer-Dobson circulation, is shown in figure 4.12 with same figure setup as figure 3.6. The two levels are picked near the equatorial tropopause at 94 hPa and near the QBO domains at 27 hPa. The 30-month averaging

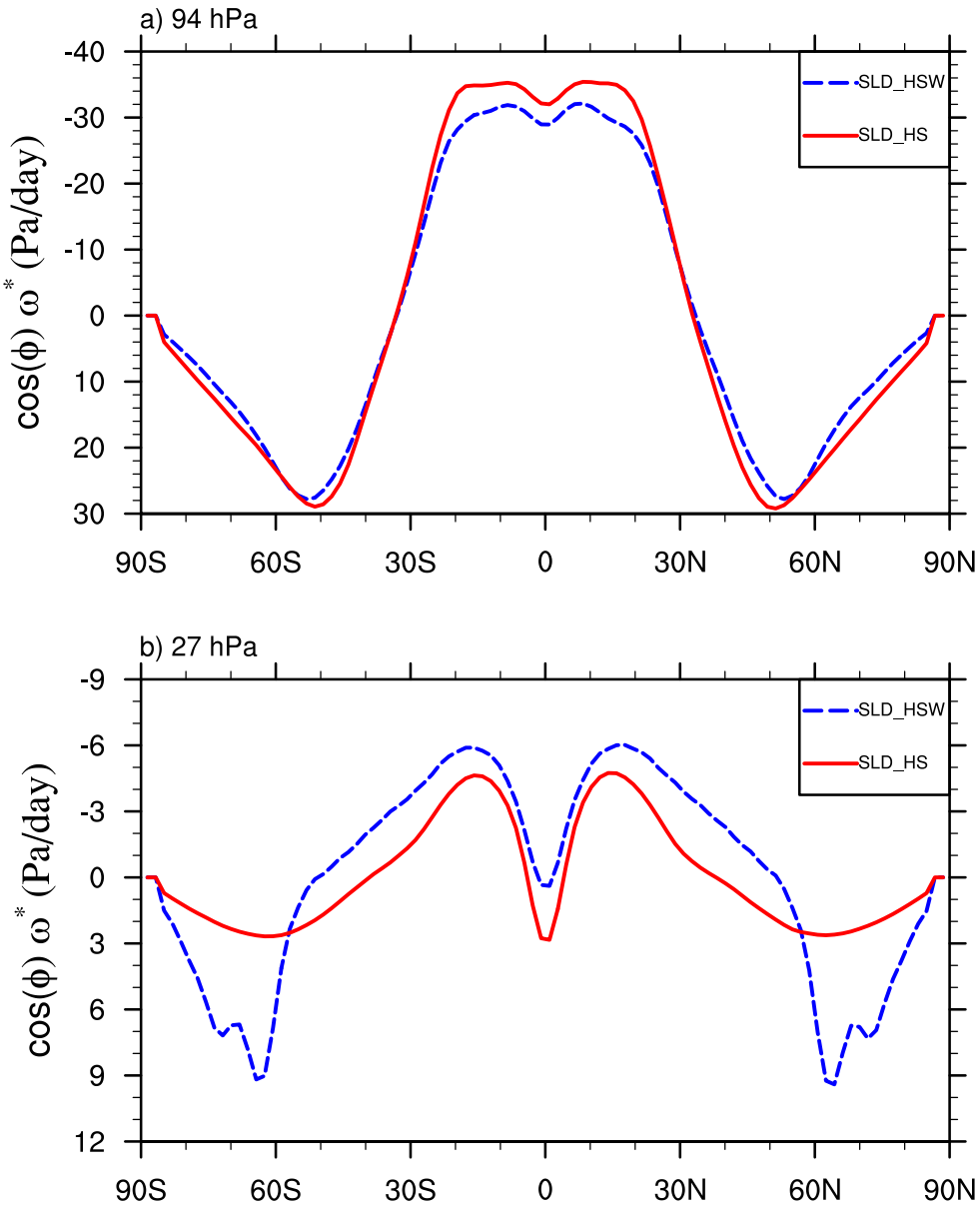

Figure 4.12: Latitudinal profiles of 30-month-mean, zonal-mean, area-weighted vertical pressure velocities $\overline{\omega}^* \times \cos\phi$ of the residual circulation for SLD simulation with HS and HSW forcing at (a) 94 hPa and (b) 27 hPa.

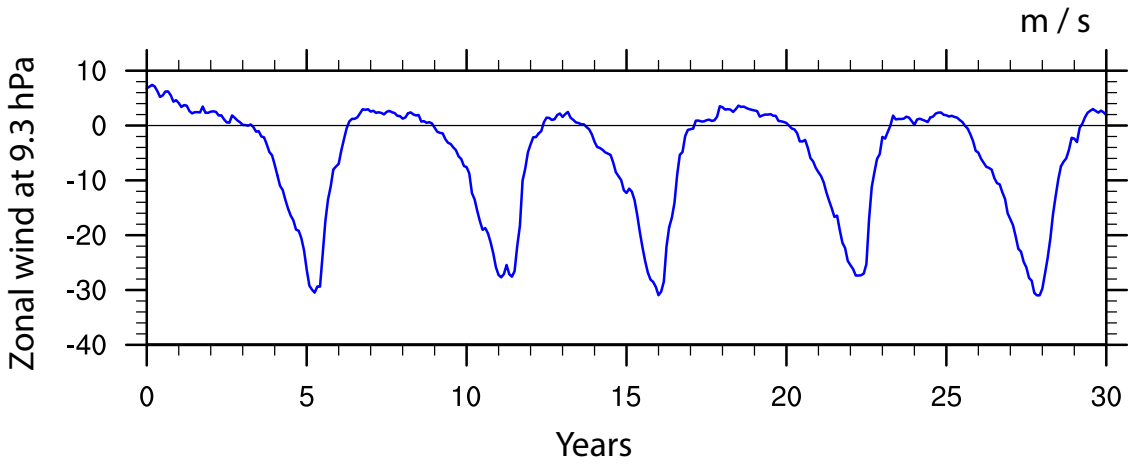

Figure 4.13: 30-year monthly-mean zonal-mean zonal wind at the equator from the SLD HSW simulation at 9.3 hPa

periods cover the years 7.1-9.6 (HS) and 2-4.5 (HSW). Similar to figure 4.12 at 94 hPa, the upwelling in the HS simulation is stronger than that in the HSW simulation in the tropics. The differences in the Brewer-Dobson circulation at 94 hPa are negligible outside the tropics. However, within the QBO domain at 27 hPa, the residual circulations in HS and HSW are quite different. The HS simulation is dominated by downwelling between $\pm$ 50°, whereas the HSW simulation is characterized by very weak downwelling directly at the equator and upwelling throughout the rest of the tropics. This upwelling is stronger in the HSW simulation that the upwelling in the subtropics and midlatitudes in HS. Polewards of about 50° N/S both simulations show downwelling again with stronger downwelling in the polar regions in HSW.

In order to examine the wave-mean flow interactions in different QBO phases, we use a 30-month composite from westerly and easterly QBO-phase data from the SLD simulation. The 9.3 hPa zonal-mean zonal wind is used as the QBO-phase criterion shown in figure 4.13. The data are selected from 5 complete QBO cycles, on average 6 months each cycle. The data around the QBO phase-transitioning stage are avoided. The phase composite wind profile is shown in figure 4.14, with the westerly (easterly)

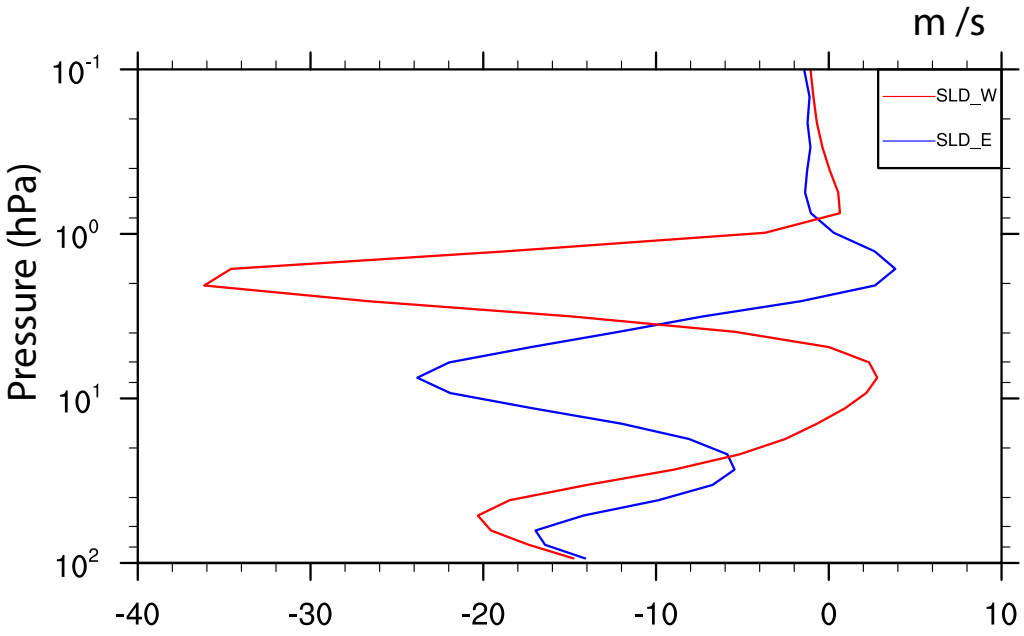

Figure 4.14: 30-month monthly-mean zonal-mean zonal wind composite at the equator from SLD, averaged between $\pm 2^{\circ}$, westerly phase composite is shown in red, easterly phase composite is shown in blue.

phase wind profile in red (blue). In this SLD simulation, the easterly wind amplitude is much stronger than the westerly wind amplitude.

An E-P vector analysis is shown in figure 4.15 with overlaid background zonal-mean zonal wind for the westerly and easterly QBO composites defined above. The E-P vectors are scaled using the same method described in Chapter 4.4. Figure 4.15a) and b) show the E-P vectors during the westerly and easterly phases. Upward and equatorward E-P vectors are observed in the subtropical troposphere below 200 hPa and similarly in the mid-latitudinal stratosphere.

Figure 4.15c) depicts the E-P vector difference using the westerly-phase E-P flux field minus the easterly-phase E-P flux field. The downward subtropical E-P vectors show more upward wave-mean flow interactions in the easterly phase than the westerly phase, which verifies the Holton-Tan relationship. In the tropical stratosphere, stacked easterly and westerly zonal wind differences are observed which are consistent with the analysis from observational data by *Naoe and Shibata* (2010). Equatorward E-P vectors are present in the tropics between 10-50 hPa, indicating more equatorward wave flux during the westerly QBO phase than the easterly phase. However the arrows are poleward above 10 hPa levels, since easterly jets are present above 10 hPa in the westerly phase plot.

4.6 Warm pole bias in SLD

In Figure 4.5, the SLD simulation shows a warm bias in the lower polar stratosphere between $100 - 3$ hPa, and a cold bias in the upper polar stratosphere from 3 hPa to the model top in comparison to the other three dynamical cores. In this section we assess this warm/cold pole bias.

Williamson et al. (1998) has documented a similar result as Figure 4.5. They observed a warm SLD bias in the lower stratosphere in full-physics simulations with a lower model top ($\sim$2 hPa). The cold bias in the upper stratosphere was not seen,

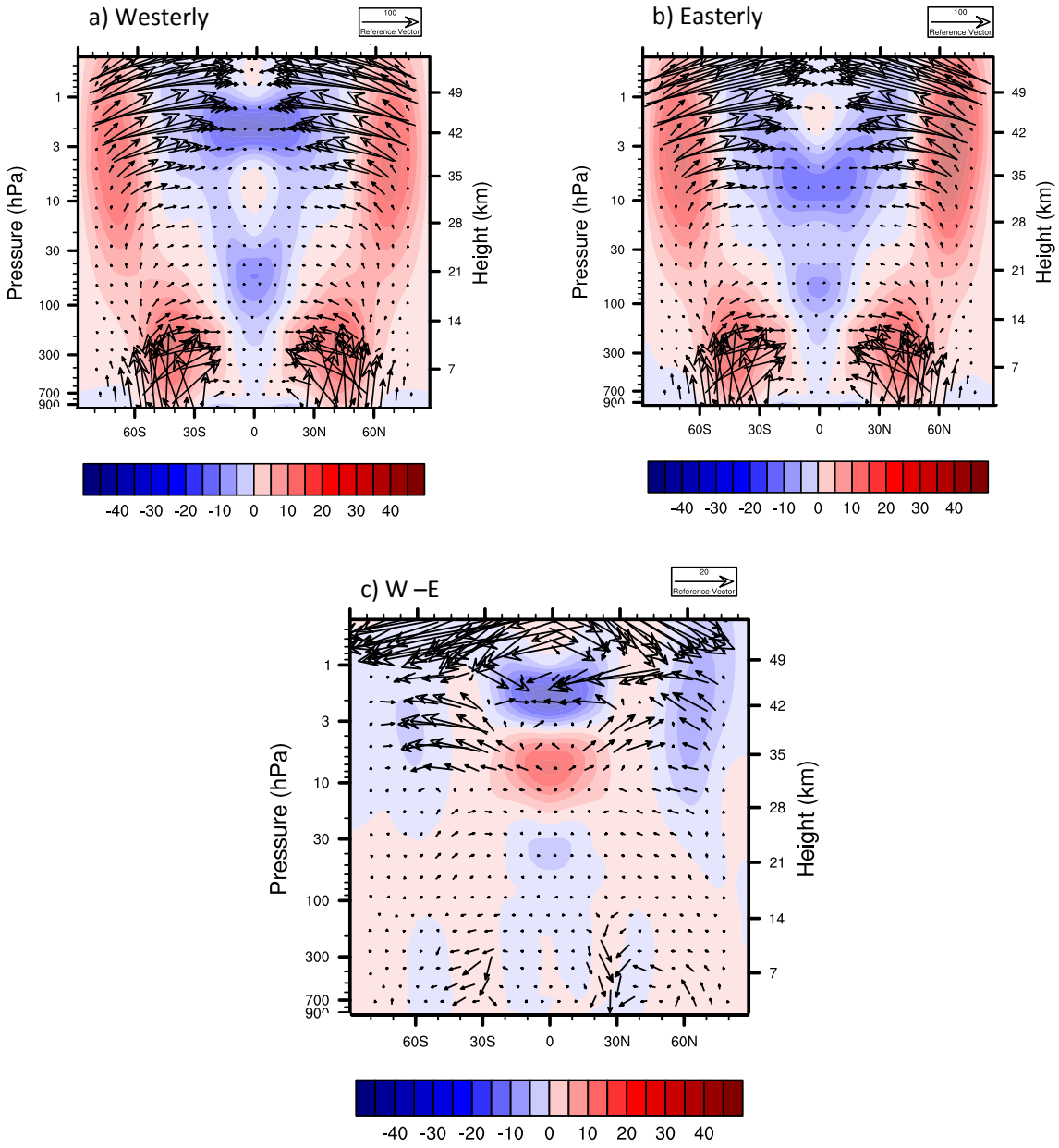

Figure 4.15: 30-month-mean zonal-mean E-P flux vectors for westerly and easterly phase composites, overlaid by the corresponding zonal-mean zonal wind in color (in m s^{-1}). a) westerly phase, b) easterly phase and c) differences (westerly - easterly). Vectors are scaled following the method in Chapter 4.4.

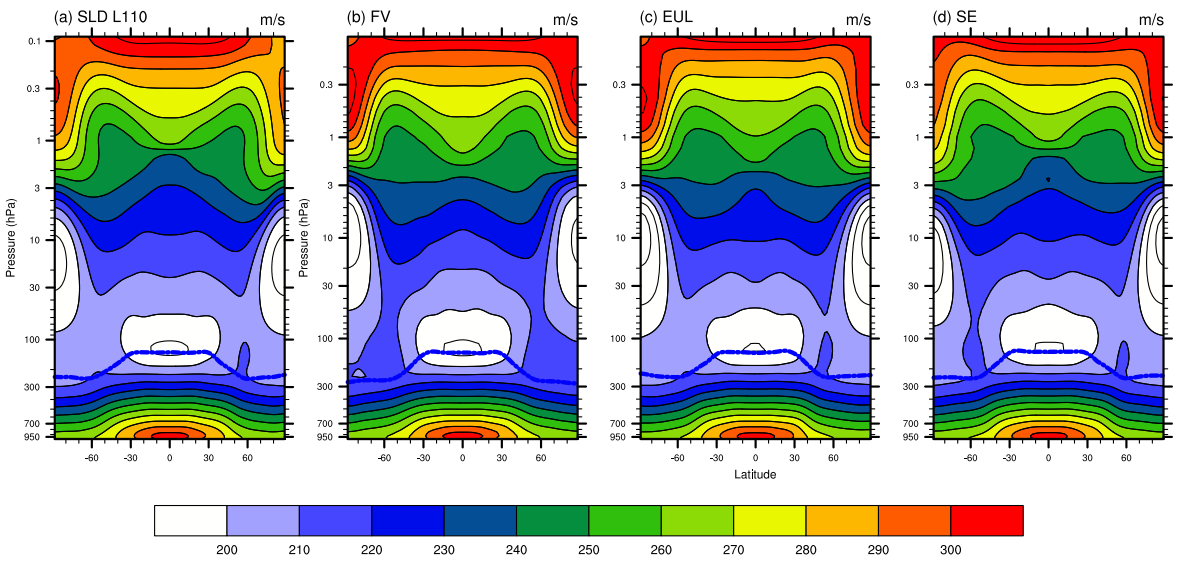

Figure 4.16: Monthly-mean zonal-mean zonal wind at the equator from different dynamical cores, averaged between $\pm 2°$, in m s^{-1}. a) SLD, b) FV, c) EUL and d) SE.

since their model configuration did not resolve the region above 3 hPa. *Williamson et al.* (1998) showed that an increase in the vertical resolution helps reduce the warm bias.

Inspired by *Williamson et al.* (1998), we doubled the vertical resolution in the SLD simulation (110 levels) and thereby halved the vertical grid spacing of our original 55-level setup. As shown in Figure 4.16, this lessens the warm bias problem in the lower stratosphere. However, the cold polar center still lies lower at about 20 hPa in SLD, compared to 10 hPa for the other three dynamical cores. The cold bias problem in the upper stratosphere above 3 hPa is also decreased, but it is still lower than the temperature in the other three dycores by about 10 K at the model top. The reason why SLD has such a temperature bias in the stratosphere is still unclear (*Williamson et al.*, 1998).

4.7 Conclusion

In this Chapter, we present a SSW simulation within an idealized framework with four different dynamical cores. The SSWs are simulated using the Held-Suarez-Williamson temperature forcing, without topography, moisture or seasonal cycles. The simulation results are different among the four dynamical cores despite the use of the identical idealized temperature forcing, vertical resolution and similar horizontal resolutions.

The SLD simulation shows more frequent SSW events than EUL, FV and SE. The SLD simulation also has a weaker latitudinal temperature gradient in the mid-latitudinal stratosphere. Furthermore, the polar jets in the SLD stratosphere are weaker than the simulations with the other three dynamical cores.

The wave-mean flow interaction is analyzed using the TEM analysis. The SLD simulation has much stronger westward wind acceleration in the stratosphere than the other three dynamical cores. This explains the relatively weak westerly polar jets in SLD. Wavenumber 1 and 2 analysis and the life cycle analysis of SSW events show relatively realistic simulations of the SSW events. Enhanced westward wavenumber 1 and 2 waves are observed before and during an SSW event, as well as an upward propagation of negative E-P flux divergence, indicating the deceleration of the westerly polar jets due to the breaking of westward waves.

The SSW interacts with both the troposphere and the stratospheric tropics. The SSW events influence the troposphere through the downward propagation of the negative NAM phase, after around 30-60 days of the SSW initiation. The polar vortices interact with the QBO as well. The inclusion of the polar vortices in the stratospheric simulation reduces the tropical downwelling of the Brewer-Dobson circulation seen in HS experiments, which slows down the QBO oscillations in HSW simulation. A TEM analysis verifies that more wave-mean flow interactions are observed in the westerly zonal wind regions.

The SLD simulation has a warm pole bias around the tropopause level and in the lower stratosphere, and a cold pole bias in the higher stratosphere around the position of the model top. This problem can be alleviated via an increase in the vertical resolution of the SLD simulation. However the exact reason why SLD has such a temperature bias, and thereby care different (weak) polar jets, remains unclear.

CHAPTER V

Idealized Quasi-Biennial Oscillations simulations with moisture and gravity wave drag

5.1 Introduction

The zonal wind variability in the equatorial lower stratosphere is dominated by a phenomenon called the Quasi-Biennial Oscillation (QBO) (*Baldwin et al.*, 2001). This phenomenon was first discovered by *Ebdon* (1960) and *Reed et al.* (1961) who observed that the equatorial zonal wind in the lower stratosphere alters periodically from westerlies to easterlies. The westerlies and easterlies propagate downward at about 1 km/month and are dissipated around the tropopause level (*Baldwin et al.*, 2001). *Lindzen and Holton* (1968) and *Holton and Lindzen* (1972) have proposed the physical mechanism for the QBO that is mainly generated and influenced by equatorial waves. More specifically, the equatorially-trapped Kelvin waves provide a westerly force and mixed-Rossby gravity waves (MRG) provide an easterly force. In addition, inertia-gravity waves and small-scale gravity waves are also important in the QBO mechanism (*Dunkerton*, 1997).

Gravity waves can be generated by a variety of processes, including flow over topography, jet streams, frontal systems and moist convection. In the Northern Hemisphere midlatitudes, flow over topography is considered the most important source

of gravity waves (*McFarlane*, 1987). In the tropical region, deep convection plays an important role in gravity wave generation (*Larsen et al.*, 1982; *Piani et al.*, 2000). Wave generation processes are often related to potential energy release. Compared to the midlatitudes, the tropical regions have less potential energy coming from meridional temperature gradients or land/sea contrasts. The latent heat released from the convection is the primary energy source in the tropics.

The downward propagating forcing that is required to sustain the QBO in nature is larger than the idealized estimates by *Lindzen and Holton* (1968) and *Holton and Lindzen* (1972), since the upwelling from the Brewer-Dobson circulation in the tropics counteracts the descent of the QBO. Therefore, the theory by *Lindzen and Holton* (1968) and *Holton and Lindzen* (1972) could not explain the complete wave forcing that is needed for the QBO mechanism (*Takahashi and Boville*, 1992). According to *Dunkerton* (1997) and *Piani et al.* (2000), a wide spectrum of waves are excited in the tropical troposphere. The horizontal scales of these waves vary from short (25 km), to large scales (10,000 - 40,000 km). The periods of these tropical waves also cover a wide rage, from short 1-3 days to long 7.4-32-day periods (*Dunkerton*, 1997). The vertically transported zonal momentum flux from short-period, short scale disturbances is comparable to long-period waves (*Maruyama*, 1994; *Lane and Moncrieff*, 2008). Overall, the small-scale gravity waves, which are mostly generated by deep convection, are very important in QBO simulations (*Piani et al.*, 2000).

QBO simulations with 3-dimensional GCMs are not straightforward. *Takahashi* (1996), *Takahashi* (1999), *Scaife et al.* (2000), *Scaife et al.* (2002), *Hamilton et al.* (2001) and *Giorgetta et al.* (2002, 2006) were among the first that successfully simulated QBO-like oscillations with GCMs. More recently *Kawatani et al.* (2010), *Orr et al.* (2010), *Xue et al.* (2012) and *Richter et al.* (2014a) also reported on QBO simulation using modern GCMs. In Chapter III we discuss 3-dimensional QBO-like simulations that only utilized the GCM dynamical cores and a very simple forcing

which consists of a temperature relaxation scheme and Rayleigh friction. This idealized physics setup by *Held and Suarez* (1994) replaces the complex physics packages that are typically used in GCMs. It lessens the uncertainty inherent in physics parameterizations and their interactions with the dynamical cores. We used this tool to analyze the influence of different numerical schemes on QBO-like simulations and more fundamentally to understand the resolved waves in the dynamical cores in Chapters II and III.

The main difficulty in simulating the QBO with GCMs is the representations of subgrid-scale processes, like moist convection, that act as wave triggers and thereby impact the wave-mean flow interactions. In current GCMs, the moist processes are represented by several different model components, including the moist turbulence boundary layer scheme, shallow and deep convection and cloud microphysics (*Neale et al.*, 2010). These complex parameterization schemes introduce large uncertainties in the simulation results, and it is therefore difficult to estimate their individual influences. In addition, gravity wave drag (GWD) schemes are often used in GCMs. They add the missing forcing of unresolved small-scale gravity waves that are e.g. triggered by topography or convection.

The scale of the gravity waves varies from 5 km to thousands of kilometers, and wavelengths that are shorter than 500 km cannot be explicitly captured by the typical 100-200 grid spacing in GCMs (*Kim et al.*, 2003). In current versions of the Whole-Atmosphere Community Climate Model (WACCM), the GWD parameterization is complex and depends on the background flow (*Beres et al.*, 2005; *Richter et al.*, 2010). The parameterized waves are generated by fronts, orography and latent heating. The latent heating is caused by moist processes and the GWD scheme specifically utilizes the heating from the deep convective parameterization (*Richter et al.*, 2010). The frontal and orographic GWD triggers are less important for QBO simulations. Therefore, we simplify this parameterization scheme and only keep the

crucial deep-convection component in some selected idealized QBO simulations.

In order to study the influence of moist processes and avoid complex full-physics parameterizations, we utilize a simplified physics parameterization following *Reed and Jablonowski* (2012) which includes key moist processes and was originally developed for short tropical cyclone simulations. We now pair this "simple-physics" package with a slightly modified HS (*Held and Suarez* (1994)) forcing to allow for long climate simulations. In addition, we also add a simple gravity wave drag parameterization to assess its influence on QBO simulations. This GWD scheme follows *Lindzen* (1981) and does not depend on the topography or the tropospheric flow. The purpose of this chapter is to provide a dynamical core QBO inter-comparison using the moist simple-physics parameterizations and dry simulations with the Lindzen GWD scheme, to study the responses of different dynamical cores to the physics forcings. In addition, we briefly discusses moist QBO simulations with the more complex flow-dependent GWD scheme by *Beres et al.* (2005) and *Richter et al.* (2010). This expands our previously dry dynamical core simulations. Our approach provides a tool to evaluate the individual influences of simple physical parameterizations.

The chapter is organized as follows. A short description of the models including the moist idealized physics and simple gravity wave drag scheme is provided in Chapter 5.2. The simulation results for moist idealized QBO simulations without GWD are discussed in Chapter 5.3. The GWD with prescribed spectrum for dry HS simulations are provided in Chapter 5.4. This is followed by a discussion of moist HS simulation with more complex (flow-dependent and prescribed) gravity wave spectra in Chapters 5.5 and 5.6. Conclusions are presented in Chapter 5.7.

5.2 Model descriptions and experimental design

5.2.1 Model setup and dynamical cores

In this study, we utilize the Community Atmosphere Model (CAM), version 5, which has been jointly developed by the National Center for Atmospheric Research (NCAR) and various U.S. Department of Energy Laboratories. CAM has four dynamical cores which are the spectral transform semi-Lagrangian (SLD), Finite-Volume (FV), spectral transform Eulerian (EUL) and Spectral Element (SE) model. A detailed description of the models and their numerical designs is provided by *Neale et al.* (2010) and in the Appendix A.

The models are run with 55 vertical levels with a model top at 0.1 hPa using a hybrid σ-p vertical coordinate. The vertical distances between the levels are Δz= 1.25 km in the stratosphere between 100-3 hPa, and we slowly stretch (5% per level) the spacing above 3 hPa to reach $\approx$ 2 km at the model top. The horizontal grid spacing for all simulations is about 2°×2° or 210–220 km in equatorial regions. That corresponds to the T63 triangular truncation in SLD and EUL, a 2°×2° latitude-longitude grid for FV and the "ne16np4" for SE which is approximately equivalent to 1.875°×1.875°. The physics time steps are 2700 s (SLD), 3600 s (FV), 720 s (EUL) and 2700s (SE). All dynamical cores are built upon a hydrostatic and shallow-atmosphere equation set. A more detailed model description of the different dynamical cores is also provided in Chapter III and will not be repeated here.

5.2.2 Moist processes with the simple-physics package

The idealized model configurations in Chapter 5.3 utilize the original *Held and Suarez* (1994) test in combination with the simple-physics parameterization package by *Reed and Jablonowski* (2012). The latter consists of three components including large-scale condensation, surface fluxes of horizontal momentum, evaporation and

sensible heat and boundary layers turbulence of horizontal momentum, temperature and specific humidity.

According to *Reed and Jablonowski* (2012) (from here on RJ12), moisture is removed from the atmosphere instantaneously when the atmosphere reaches saturation. No cloud stage is considered and there is no re-evaporation during the precipitation processes. These processes are described in Eqs. (1) through (14) in RJ12. The temperature and specific humidity changes due to condensation are

$$\frac{\partial T}{\partial t} = \frac{L}{c_p} C \tag{5.1}$$

$$\frac{\partial q}{\partial t} = -C \tag{5.2}$$

where T is temperature, t is time, q is specific humidity, C is the condensation rate, and L = 2.5×10^6 J kg^{-1} K^{-1} is the latent heat of evaporation at 273.16 K, and c_p= 1004.6 J kg^{-1} K^{-1} is the specific heat of dry air at constant pressure. The precipitation is the summation of condensed water over all vertical layers at each grid point.

The simple-physics package assumes a water-covered Earth with no topography. The surface temperature is set to T = 302.15 K. This SST acts as a lower-boundary forcing on the atmosphere which provides latent and sensible heat fluxes. The surface flux of temperature and specific humidity follows Eqs. (35) and (36) in RJ12. The RJ12 surface flux of momentum and the boundary layer mixing of momentum are is not used and substituted by the original low-level HS Rayleigh friction of the wind.

The radiation scheme follows the original HS temperature relaxation forcing to a prescribed radiative equilibrium temperature. The additional Rayleigh friction at the model top from 1hPa to 0.1 hPa is kept from Chapter III.

5.2.3 GWD Parameterization: Source spectrum

We also paired the original dry HS Model setup with a gravity wave drag parameterization scheme following *Beres et al.* (2005) and *Garcia et al.* (2007). The GWD parameterizes non-orographic gravity waves by launching a wave spectrum that does not depend on the flow. The source stress spectrum is specified as a Gaussian in phase speed c and follows

$$\tau_s(c) = \tau_0 \times \tau_b exp\left[-\left(\frac{c}{c_w}\right)^2 \right] \tag{5.3}$$

$$\tau_b = max(\tau_{min}, \frac{1}{2}\left[1 + tanh\Big(\frac{(\phi - \phi_0)}{\Delta\phi}\Big)\right] + \frac{1}{2}\left[1 - tanh\Big(\frac{(\phi + \phi_0)}{\Delta\phi}\Big)\right] \tag{5.4}$$

where the phase speed c_w is 30 m s^{-1}, ϕ_0 is 40°, and $\Delta\phi$ is 10°, τ_{min} is 0.2, and the maximum source stress is τ_0 is 6.4 $\times$ 10^{-3} Pa. The coefficient τ_b is a weighting function to the source stress which has a latitudinal distribution, shown in figure 5.1. This coefficient has a smaller value in the tropics and higher value towards the pole, which is an empirical distribution to achieve better simulation results (*Beres et al.*, 2005; *Garcia et al.*, 2007). The phase speed spectrum is centered at 0 m s^{-1}, and a range of phase speeds with specified widths and resolution is used

$$c \in [\pm\Delta c, \pm 2\Delta c, ... \pm c_{max}]. \tag{5.5}$$

In our simulation we use Δc= 2 m s^{-1}, and c_{max} = 64 m s^{-1} giving 64 phase speeds. These waves are launched at 100 hPa level. To account for unrepresented spatial and temporary intermittency in wave sources, the gravity wave drag is multiplied by an efficiency factor ϵ, and we used the same default value 1/64 as in *Beres et al.* (2005). The wave dissipation processes are parameterized following the saturation theory by *Lindzen* (1981).

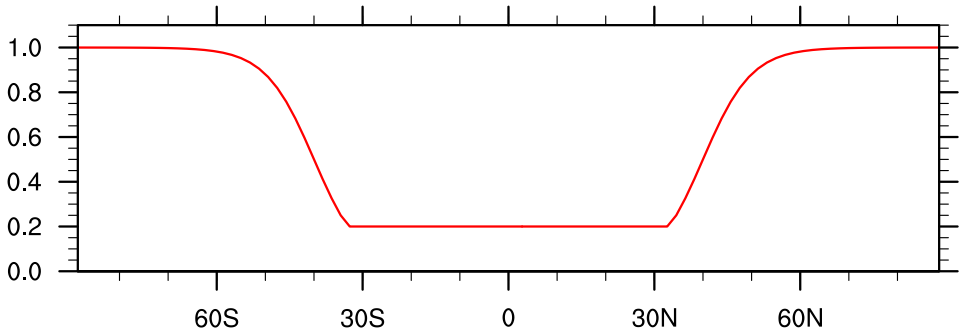

Figure 5.1: Latitudinal distribution of τ_b, following Eq. (5.4)

5.2.4 Flow-dependent source spectrum GWD

In order to improve the simulation, we also modified the simple physics package and the HS forcing. In particular, the Sea Surface Temperature (Sea Surface Temperature (SST)) distribution is modified to have a latitudinal dependence. This new SST profile, T_s, is defined by

$$T_s = \Delta T exp\Big(- \frac{\phi^2}{2(\Delta\phi)^2} \Big) + T_{min} \tag{5.6}$$

where Δ T = 29 K, T_{min} = 271 K is the sea surface temperature at the poles, ϕ is the latitude in radians and $\Delta\phi = 26\ \pi/180$.

The modified HS forcing has a slightly different equilibrium temperature profile, T_{eq}

$$T_{eq}(\phi, p) = max\Big\{200K, \big[294K - (\Delta T)_y sin^2\phi - (\Delta\theta)_z log\big(\frac{p}{p_0}\big) cos^2\phi\big]\big(\frac{p}{p_0}\big)^{\kappa}\Big\} \tag{5.7}$$

where $(\Delta T)_y$ = 65 K, $(\Delta\theta)_z$ = 10 K, p_0 = 1000 hPa is a reference pressure and $\kappa = R_d/c_p$. The two modifications with respect to the original HS are the constant 294 K (original 310 K) and the higher $(\Delta T)_y$ 65 K value (originalyl 60 K). This improvement shows a more realistic climatology (not shown) compared to the configuration in

Chapters 5.2.2 and 5.3 setup and an improved QBO-like oscillation compared to figure 5.2c.

In addition, a convection dependent GWD scheme following *Beres et al.* (2005) is implemented in this modified moist package. The moist heating term in the simple physics package (Eq. 5.1) is used for the launch of gravity waves instead of the convective heating which is suggested in the *Beres et al.* (2005) scheme. In addition several tuning parameters are modified to reach a more realistic QBO, including the efficiency factor $\epsilon = 0.25$ and the assumed convective fraction Convective Fraction (CF) = 20%. CF was originally 5% when paired with the *Zhang and McFarlane* (1995) convection scheme. In our simple moist package, the moist heating term is weaker than the convective heating term in realistic Whole Atmospheric Community Climate Model simulation results. Therefore, we increased the CF to trigger similar amount of waves in the GWD scheme, in order have a more realistic simulation.

5.3 Moist QBO simulation with 'simple-physics'

In this section, the moist simulations are compared with the dry HS simulations that are described in Chapter III.

5.3.1 QBO-like oscillation

This section discusses the QBO-like simulations with simple moist physics forcings (see Chapter 5.2.2) in three different CAM dynamical cores, SLD, FV and SE. Figure 5.2 shows the 12-year time series of the monthly-mean zonal-mean zonal winds which are averaged between $\pm 2^{\circ}$. The stratospheric circulations have very different characteristics despite the identical experimental setup. The moist simulation results are very different from the dry simulations showed in Chapter II and Chapter III.

Figure 5.2 a) shows that the SLD simulation has 9.5 QBO cycles in the 12-year simulation period. Therefore, the QBO-like oscillation has a period around 1.3 years,

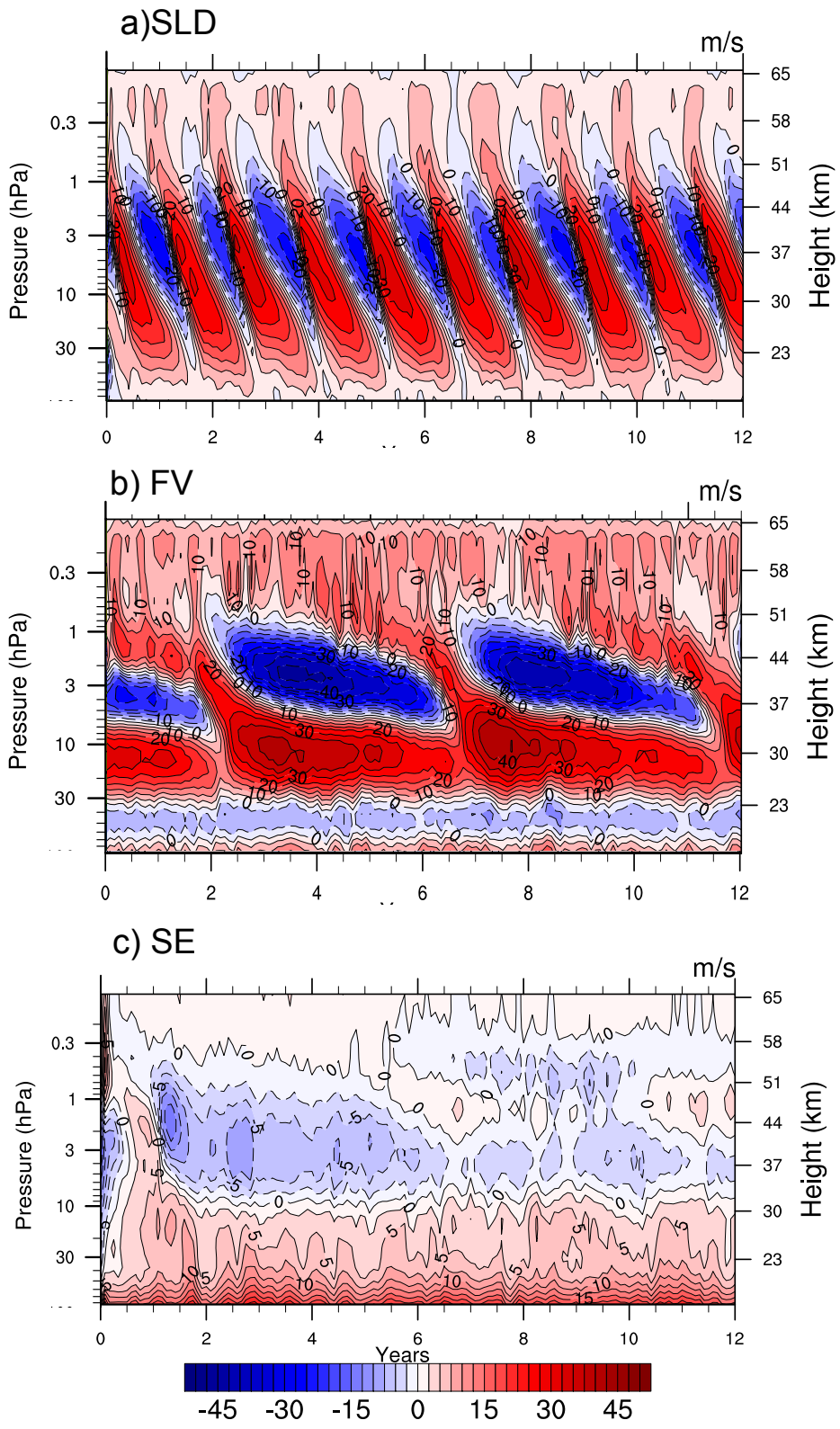

Figure 5.2: 12-year time series (x-axis) of the monthly-mean zonal-mean zonal wind at the equator. QBO-like simulation with simple moist physics simulation in different dynamical cores a) SLD, b) FV, c) SE.

which is much shorter than the 3.6-year period in the dry SLD simulation (figure 3.1a). The QBO also propagates deeper into the lower stratosphere to around 100 hPa. The wind amplitude range is expanded and now spans -25 to 40 m s^{-1}. The westerly wind amplitude has increased greatly from 15 m s^{-1} to 40 m s^{-1}, however the easterly wind amplitude has decreased from -35 m s^{-1} to -25 m s^{-1}, indicating a possible increase of westerly waves.

The moist FV simulation is now able to generate a QBO-like oscillation as seen in figure 5.2 b), which was not possible in the dry FV run (figure 3.1b). The oscillation period is about 5 years, however the 12-year simulation is too short to determine the QBO period with certainty. This QBO-like oscillation has an amplitude of -45 m s^{-1} to 40 m s^{-1}. The FV oscillation lies higher than the SLD simulation which extends from 0.3 to 30 hPa. The westerly wind regime slowly travels downward from 0.3hPa to about 2 hPa, then "quickly" descends to around 10 hPa and then slowly travels to 30 hPa. The 10 hPa to 30 hPa domain is occupied by slowly downward traveling westerly jets. The easterly jet slowly propagates downward from 1 to 10 hPa, and is not able to break through the westerly jets and penetrate down to the lower stratosphere.

The SE simulation, show in Fig. 5.2 c), is also very different from the dry SE simulation (figure 3.1d) . The most dominant feature is that the oscillating amplitude has decreased to -10 m s^{-1} to 5 m s^{-1}. For consistency we used the same color scheme as used for the SLD and FV results. The oscillating period for the SE simulation is decreased to around 6 years. Moreover, the lower domain between 30 to 100 hPa was occupied by easterly jets in the dry simulation, and is now dominated by a westerly jet, shown in red on this plot.

In general, the inclusion of moist processes has shortened the QBO-like oscillation in all three dynamical cores. It is interesting that the QBO-like oscillation now appears in the moist FV simulation. This indicates that the simple moist physics

package provides wave triggering mechanisms that can greatly impact the QBO wave-mean flow interactions. A wave analysis is provided to verify this hypothesis.

5.3.2 Wave analysis

As mentioned before, the QBO is mainly generated and influenced by waves. In order to understand the wave forcing mechanisms, we utilize a Transformed Eulerian (TEM) analysis. This TEM analysis decomposes the zonal wind acceleration into four components, the wave-mean flow interaction, vertical advection, horizontal advection and a residual X. The expressions are explained in *Andrews et al.* (1983) and Chapter III. In our previous work, we show that the resolved wave-mean flow interaction expressed by the divergence of the Eliassen-Palm flux plays the most important role in the wind acceleration, as seen in Chapters II to IV.

Figure 5.3 shows the TEM analysis for 20 months using 6-hourly instantaneous data for dry and moist SLD simulations. The divergence of the Eliassen-Palm flux and the zonal-mean zonal wind acceleration versus time is presented at 9.3 hPa. Although there is a time phase shift, the divergence of the E-P flux is the component that mainly influence the wind acceleration. The peak value for the divergence of the E-P flux is -0.5 to 1.3 m s^{-1} day^{-1}, which is about three times as big as the corresponding dry value. This indicates that the wave-mean flow interaction is much stronger than it is in the dry SLD simulation.

Figure 5.4 shows a wave-number frequency analysis of the zonal wind in the dry and moist SLD simulation following *Wheeler and Kiladis* (1999). The analysis utilizes 20-month 6-hourly instantaneous zonal wind data at 18 hPa. The overlaid curves are dispersion curves as described in *Wheeler and Kiladis* (1999) for Equatorial Rossby waves (ER), Mixed-Rossby Gravity waves (MRG), Equatorial Inertia-Gravity waves (EIG) and Kelvin waves. The dashed curves are Doppler shifted dispersion curves as described in *Yang et al.* (2011) and Chapters II and III with background wind speed

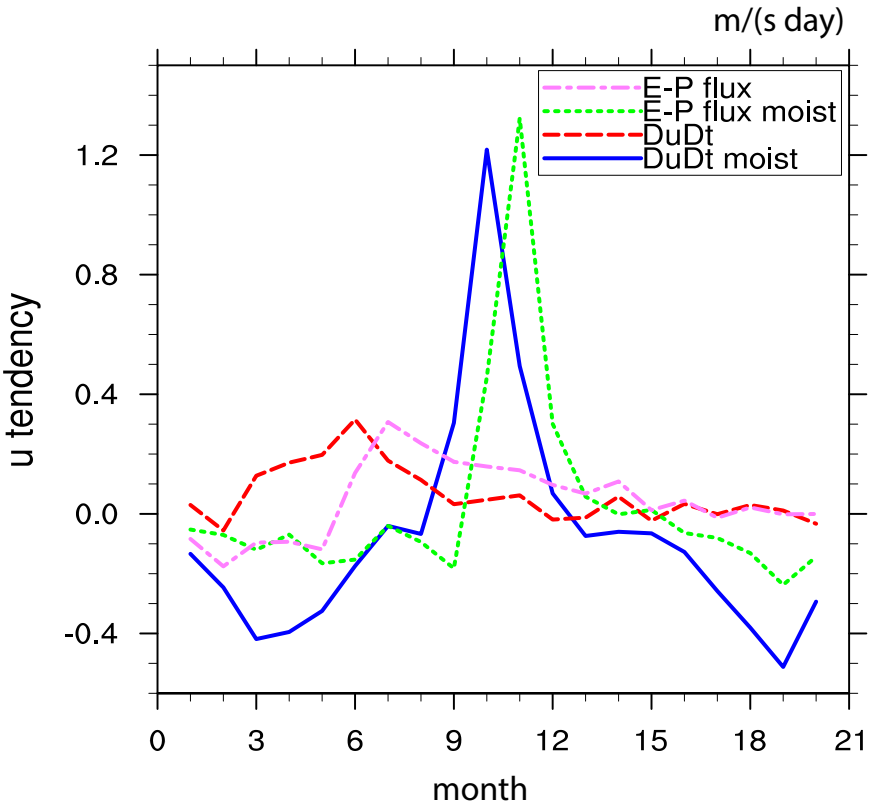

Figure 5.3: Transformed Eulerian Mean analysis for SLD moist and SLD dry simulations. 20-month instantaneous data at 6-hourly frequency is used for this analysis. Total zonal-mean zonal wind acceleration Du/Dt is and the wave-mean flow forcing (divergence of Eliassen-Palm flux) versus time at 9.3 hPa are plotted for both moist and dry simulations, in m s^{-1} day^{-1}.

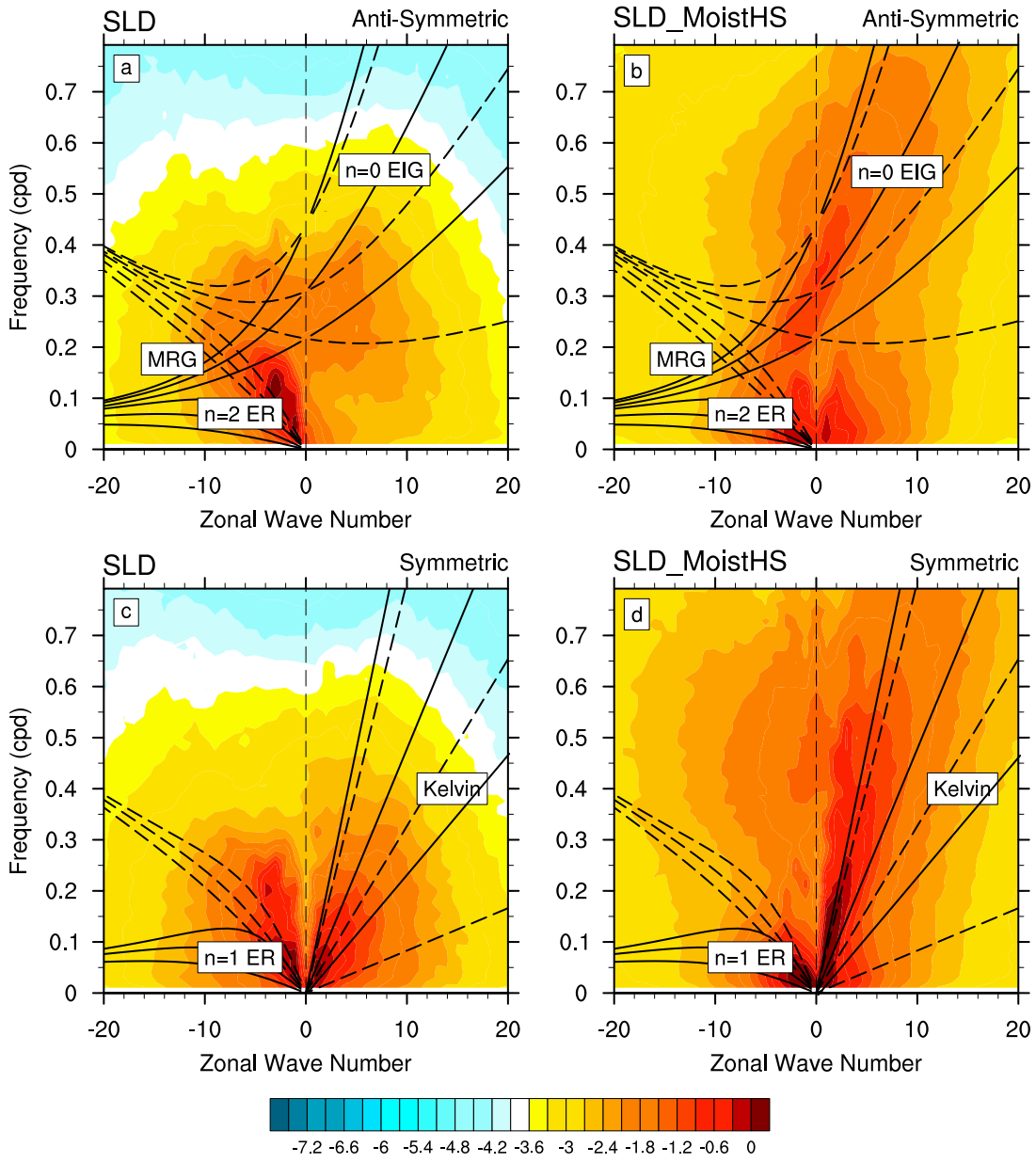

Figure 5.4: Wavenumber frequency analysis comparison for the SLD zonal wind at 18 hPa 15°S-15°N: raw power spectra (logarithmic scale in $\log_{10}$(m s^{-1})), with (top) and without (bottom) moisture. First row shows the anti-symmetric component of dry (left column) and moist (right column) SLD simulation, second row depicts the symmetric component, plus overlaid dispersion curves with (solid) and without (dashed) Doppler shift with background wind speed $\bar{u}$ = -7 m s^{-1}. The dispersion curves are for equivalent depth h of 12, 50 and 200 m (increasing towards higher cpd).

$\bar{u}$ = -7 m s^{-1} The dispersion curves are for equivalent depth h of 12, 50 and 200 m which correspond to zonal wave speeds of 11, 22, and 44 m s^{-1}. This figure shows the $\log_{10}$ of the raw power without removing the background spectrum, in order to observe the overall resolved wave activity.

The anti-symmetric plot for the SLD dry simulation shows spectral peaks for n=2 ER. The spectral peaks for ER are detected between wave numbers -1−-5 with frequencies $\leq$ 0.2 cycles per day (cpd). The spectral peaks for MRG and EIG are detected as well, but they are not as strong as ER. In the anti-symmetric plot for the moist SLD simulation, we observe more wave activity over the whole spectral domain, especially for low wave numbers (from -10 to 10). In particular, MRG and n=0 EIG with wave numbers -4−4, period 2-5 days are detected. The n=2 ER with wave number 4−6 are decreased in the SLD moist simulation.

In the symmetric plot for the SLD dry simulation, spectral peaks for n=1 ER between wave number -1−-5 are detected with frequency $\leq$ 0.3 cpd. Kelvin waves are observed at wavenumber 0.4 with frequency $\leq$ 0.2 cpd. Similarly as the anti-symmetric plot, we observe more wave activity over the whole spectral domain, especially between wavenumbers -10−10. Increased Kelvin wave activity is observed at this level with low wavenumber but broader frequency range up to 0.6 cpd. The n=1 ER waves with wavenumbers 4−6 are decreased in the SLD moist simulation.

Note that the decrease in certain waves and the low wavenumber increase which are observed in moist simulations are also a consequence of the wave filtering effect of the QBO, as mentioned in Chapters II and III. We observed similar phenomena in the dry runs. In a moist simulation with shorter QBO period and larger oscillation magnitude compared to the dry simulation, we expect the wave filtering mechanism to be stronger.

We also provide a relative power spectrum following *Wheeler and Kiladis* (1999) in figure 5.5. The relative plot divides the Raw Power by the background in order

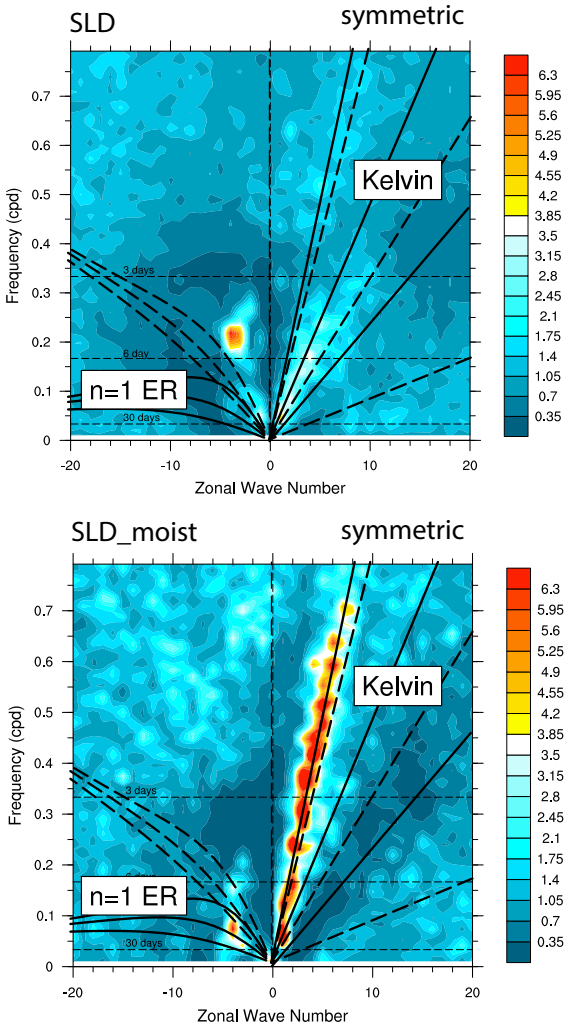

Figure 5.5: Wave-number frequency analysis comparison for the SLD zonal wind at 18 hPa 15°S-15°N: raw power / background (logarithmic scale in $\log_{10}(\text{m s}^{-1})$), with and without moisture, symmetric component. overlaid by dispersion curves with (solid) and without (dashed) Doppler shift with background wind speed $\bar{u}$ = -7 m s^{-1}. The dispersion curves are for equivalent depth h of 12, 50 and 200 m (increasing towards higher cpd)

to remove the background red noise. This plot also uses the zonal wind field at 18 hPa between 15°S-15°N. A spectral peak at wave number -4 and 5-day period (cpd = 0.2) is observed in the dry plot. This spectral peak shifted downward in the moist plot, which suggests that the wave period becomes longer (around 10 days) and is therefore slower. The spectral peaks for Kelvin waves are weak in the dry plot, but very strong in the moist simulation (wave number 1-4 and frequency from 0.03 to 0.6 cpd). The wave speeds for Kelvin waves are faster in the moist simulation than the dry simulation. This is because of the Doppler-shift effect, the background wind speed at 18 hPa is faster than that in dry simulations. Although *Kiladis et al.* (2009) argues that moist convectively coupled gravity waves are slower than their dry counterparts the influence of the background wind field seems to be the most dominant factor.

Similar analysis is conducted using the FV dry and moist data in figure 5.6 using the temperature field at 22hPa between 15°S-15°N. The raw power is plotted with logarithmic scale in $\log_{10}$(K). The resolved dry waves in FV are less strong than the resolved dry waves in SLD as we argued in Chapter III in the both symmetric and anti-symmetric plots. The spectral peaks for the dry FV simulation are wavenumber -1 to -8 n=2 ER waves with frequency $\leq$ 0.25 cpd, wavenumber -6 to 6 MRG and EIG waves with frequencies of around 0.3 cpd in the anti-symmetric field, and low wavenumber n=1 ER and Kelvin waves in the symmetric plot.

The power spectra for the moist FV simulations are stronger in comparison to the dry FV simulation, especially with wavenumbers -10−10, which is consistent with the SLD dry/moist simulation. The waves are slower for westward propagating waves including n=1,2 ER and MRG and faster for Kelvin waves and EIG. The Kelvin waves are greatly enhanced in the FV moist simulations.

Overall, the inclusion of moist processes has greatly enhanced the wave-mean flow interaction and the wave generating processes in SLD and FV. The increased power of Kelvin waves in moist simulations are observed in both SLD and FV. The waves

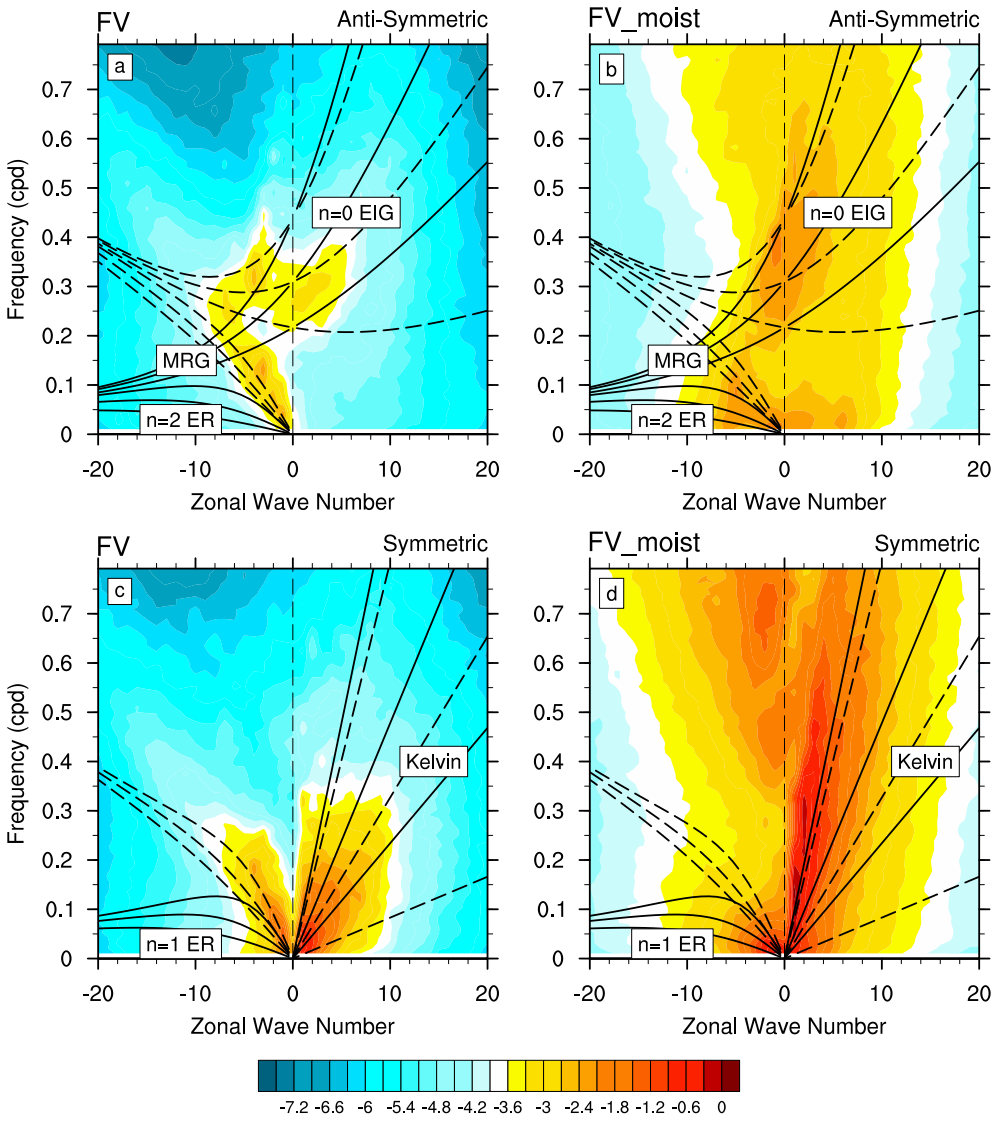

Figure 5.6: Wave-number frequency analysis comparison for the FV temperature field at 22 hPa 15°S-15°N: raw power spectra (logarithmic scale in $\log_{10}$(K)), with and without moisture. First row are the anti-symmetric component of dry (left column) and moist (right column) FV simulation, second row are the symmetric component, overlaid by dispersion curves with (solid) and without (dashed) Doppler shift with background wind speed $\bar{u}$ = -7 m s^{-1}. The dispersion curves are for equivalent depth h of 12, 50 and 200 m.

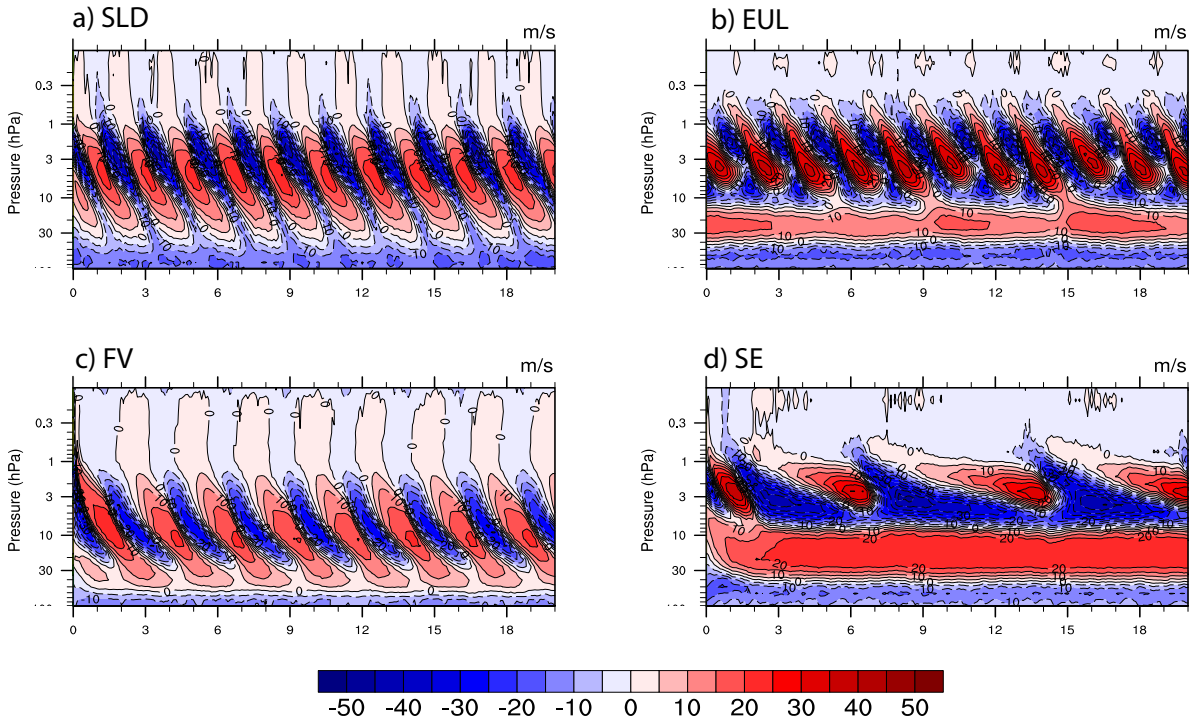

Figure 5.7: Monthly-mean zonal-mean zonal wind at the equator for four dynamical cores, 20 year simulation. Simulation with GWD efficiency factor 1/64

are also greatly influenced by the background wind field through the Doppler effect. The westward waves are slower and eastward waves are faster in moist simulations.

5.4 Dry QBO simulation with a prescribed GWD source spectrum

In this section, dry QBO simulations with GWD are presented, using exactly the same GWD scheme with prescribed source spectra (chapter 5.2.3) and the same efficiency factor $\epsilon = 1/64$ for all dynamical cores. The TEM analysis is used to quantify the relative role of the wave-mean flow interaction and the GWD forcing.

5.4.1 QBO-like oscillation

Figure 5.7 shows the 20-year time series of the monthly-mean zonal-mean zonal wind in all four dynamical cores which are averaged between ± 2° N/S. The QBO-like oscillations are more regular than their dry counterparts (figure 3.1) without GWD which are shown in Chapter III. Figure 5.7a depicts the QBO behavior with GWD in the SLD dynamical core. The QBO period in SLD with GWD has a period of around 1.7 years which is much shorter than the QBO simulation without GWD (3.6 years). The peak wind amplitude is around -30 to 20 m s^{-1}. The QBO domain extends further downward to around 70 hPa.

Figure 5.7b depicts the EUL simulation with the same GWD scheme. The QBO-like oscillation exhibits a period of about 2 years, which is also significantly shorter than the EUL simulation without GWD (13-16 years, figure 3.1c). The westerly wind amplitude is stronger than the original EUL simulation and also the SLD simulation with GWD, around -30 to 35 m s^{-1}. The QBO domain sits higher than the SLD simulation but remains approximately the same as the original EUL simulation. A westerly jet with approximately 10 m s^{-1} between 10 to 30 hPa is visible in the whole 20-year simulation, with small amplitude fluctuations. The descending domain with a fast westerly wind in the original EUL between 3 to 10 hPa no longer exists. The vertical downward propagating speed for both the westerly and easterly jets are steady in the EUL GWD simulation.

Figure 5.7c shows the FV GWD simulation. The FV GWD simulation is very similar to the SLD GWD simulation, with a slightly reduced vertical extent. The QBO period is around 2.5 years, and the wind amplitude varies between -20 to 15 m s^{-1}. The oscillation is regular. The application of the GWD parameterization in FV greatly improves the QBO-like simulation. Recall that the FV simulation without GWD does not generate a QBO-like oscillation, but rather steady jets in the stratosphere (figure 3.1b).

Figure 5.7d shows the SE GWD simulation. The QBO behaves very differently from the original SE simulation. The period is shortened, around 3.5 cycles are completed in the 20-year simulation period, but we cannot provide a specific period with certainty. The zonal wind magnitude range is increased with -40 to 25 m s^{-1}. A steady westerly jet occupies the levels between 7 to 50 hPa at 20 m s^{-1}. The fast descending branches between 3-10 hPa in figure 3.1d also disappeared. Overall, the SE GWD simulation shows some similarities to the EUL GWD simulation, but with longer period and higher wind amplitude. These similarities are also observed in QBO-like simulation without GWD as described in Chapter III.

In summary, the QBO simulations have been improved when adding a GWD scheme. The QBO periods are shortened and the wind amplitudes are increased. This indicates that the GWD scheme plays an important role in driving the QBO in our simulations.

5.4.2 Wave analysis

In order to quantify the relative role of the QBO driving mechanisms, we utilize the TEM analysis and the wind acceleration due to the GWD scheme. We then compare the wind acceleration from different sources in the SLD GWD simulation. 6-hourly instantaneous data from the SLD GWD simulation for 30 months are used in this analysis, as shown in figure 5.8.

Figure 5.8 depicts the time-pressure cross section of a) the zonal wind acceleration, b) mean vertical advection, c) E-P flux divergence which represents the resolved wave forcing, d) the GWD parameterization forcing and e) the residual X. This 30-month period covers more than one cycle of the QBO SLD simulation. The mean meridional advection is not shown because of its small magnitudes between $\pm$ 0.03 m s^{-1} day^{-1}. All of these panels are overlaid by contours of the monthly-mean zonal-mean zonal wind (in white) with enhanced zero wind line.

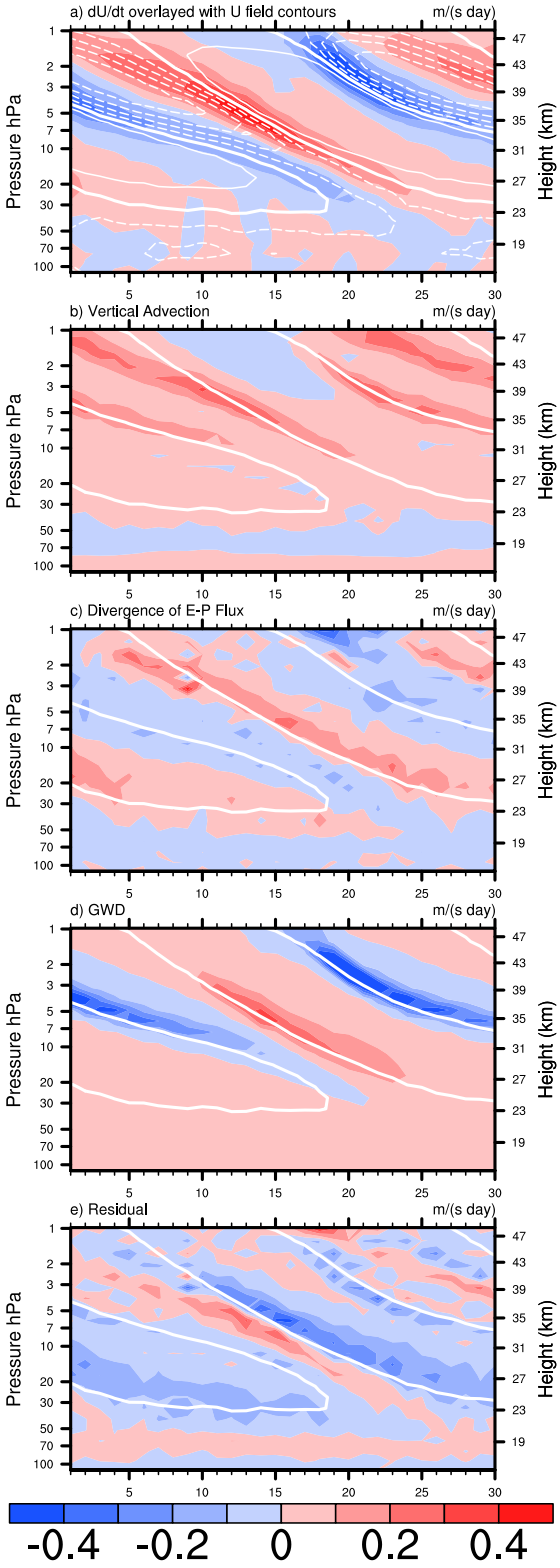

Figure 5.8: TEM analysis of 6 hourly instantaneous data from the SLD GWD simulation for 30 months (continued caption next page).

Figure 5.8: Monthly-mean zonal-mean time-pressure cross sections of the TEM components, averaged between ±2°. a) Zonal wind acceleration, b) acceleration from vertical advection c) E-P flux divergence and d) acceleration from GWD parameterization e) residual X. White contours are overlaid to show zonal-mean zonal wind at 8 m s^{-1} spacing, in b)-d) only zero wind contour is shown.

The vertical advection provides most of the westerly acceleration during the easterly phase, the divergence of E-P flux and GWD provides most of westerly acceleration during the westerly phase. The easterly acceleration is provided mainly by the divergence of E-P flux and the GWD. The residual term X mostly counteracts the divergence of the E-P flux. Moreover, the westerly acceleration for the vertical advection, divergence of the E-P flux and the GWD are around 0.3 m s^{-1} day^{-1}, and have similar contribution. The easterly acceleration for vertical advection is about 0.1 m s^{-1} day^{-1} and 0.2 m s^{-1} day^{-1} for the divergence of the E-P flux, but around 0.4 m s^{-1} day^{-1} for GWD. This explains the increasing easterly wind amplitude of the QBO in the SLD GWD simulation. The source of the residual term X is mostly coming from explicit and implicit numerical diffusion and the thermal temperature relaxation as explained in Chapters II and III.

5.5 Moist QBO simulations with a flow-dependent GWD source spectrum

In order to improve the SE simulation, the simple physics package and HS forcing are modified which is described in Chapter 5.2.4. The moist simulation with the SE dynamical core is shown in figure 5.9a. 10-year records of monthly-mean zonal-mean zonal winds with the SE dynamical core are provided. The QBO-like oscillation has a period around 5 years and a wind amplitude of around 40 m s^{-1} and - 30 m s^{-1}.

The simulation using this modified simple-physics and flow-dependent GWD is shown in figure 5.9b. The QBO period is shortened to ∼2.5 years. The westerly wind amplitude remains the same ∼40 m s^{-1} as the modified moist simulation in figure

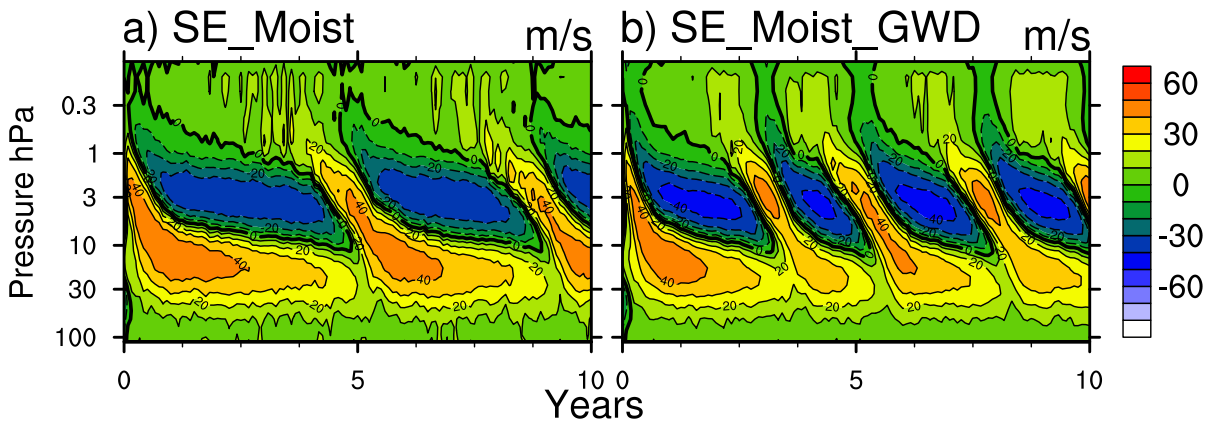

Figure 5.9: Monthly-mean zonal-mean zonal wind at the equator from SE dynamical cores with a) moist process, b) moist process and GWD.

5.9b. The easterly wind amplitude increased to $\sim$ - 40 m s^{-1}. This result is consistent with Chapter 5.4. In particular, an enhanced westward wind acceleration is observed in the GWD simulations. The possible reason for this is that westerly waves are mostly observed in lower levels and only easterly waves are able to propagate into the QBO region. This QBO-oscillation has much stronger wind amplitudes than other more realistic QBO simulations in CAM as shown in *Richter et al.* (2014b).

5.6 Sensitivity test of the moist QBO simulations with a prescribed GWD source spectrum

In this section we utilize the prescribed GWD source spectrum paired with the moist HS physics package (Chapter 5.2.4) to conduct a simple sensitivity test of the QBO simulations. The prescribed GWD source spectrum is the same as described in Chapter 5.3.2. To observe the wave evolution and dissipation processes, the source stress (τ_s in equation 5.3) is analyzed.

5.6.1 Prescribed GWD launched at $\sim$ 100 hPa

This experiment uses the launch level of100 hPa (same as in Chapter 5.4) and the updated moist HS physics package (Chapter 5.5) with the SE dynamical core. The 2400-day record of monthly-mean zonal-mean zonal wind is shown in figure 5.10. The simulation cannot complete a cycle within this 2400-day simulation period. An easterly jet appears at $\sim$ 10 to 1 hPa and a westerly jet occupies the domain between 100 to 10 hPa. This is curious since the simulation with only prescribed GWD in Chapter 5.4 and the simulations with only moist HS in Chapter 5.5 show faster QBO signals than this combination of the prescribed GWD and moist HS.

The time-averaged source stress τ_s with different phase speeds is then analyzed at different levels in figure 5.11. At 94 hPa (figure 5.11a) which is closes to the 100 hPa launch level, the source stress is all 0. The level above it shows a nearly perfect Gaussian shape as shown in equation 5.3. Waves with westerly (positive) phase speed start to dissipate at 63 hPa in figure 5.11c, which is consistent with the background wind speed. Note that the majority of the dissipation is observed at low phase speeds at this level, since the background wind speed is low around 5 to 10 m s^{-1}. More high phase speed waves are dissipated in higher levels as seen in figure 5.11d. And in levels above 10 hPa figure 5.11e and 5.11f, we can observe the dissipation of easterly phase speed waves. It is possible that the westerly phase source stress is too strong and therefore sustains a very steady high-speed jet at lower levels. In addition, the easterly phase source stress is not strong enough to propagate downward and break through the westerly jet.

5.6.2 Prescribed GWD launched at $\sim$ 200 hPa

Another 2400-day simulation is conducted with a prescribed GWD launch level $\sim$ 200 hPa which is paired with same moist HS physics. The monthly-mean zonal-mean zonal wind is shown in figure 5.12. The QBO period is around 2 years. The

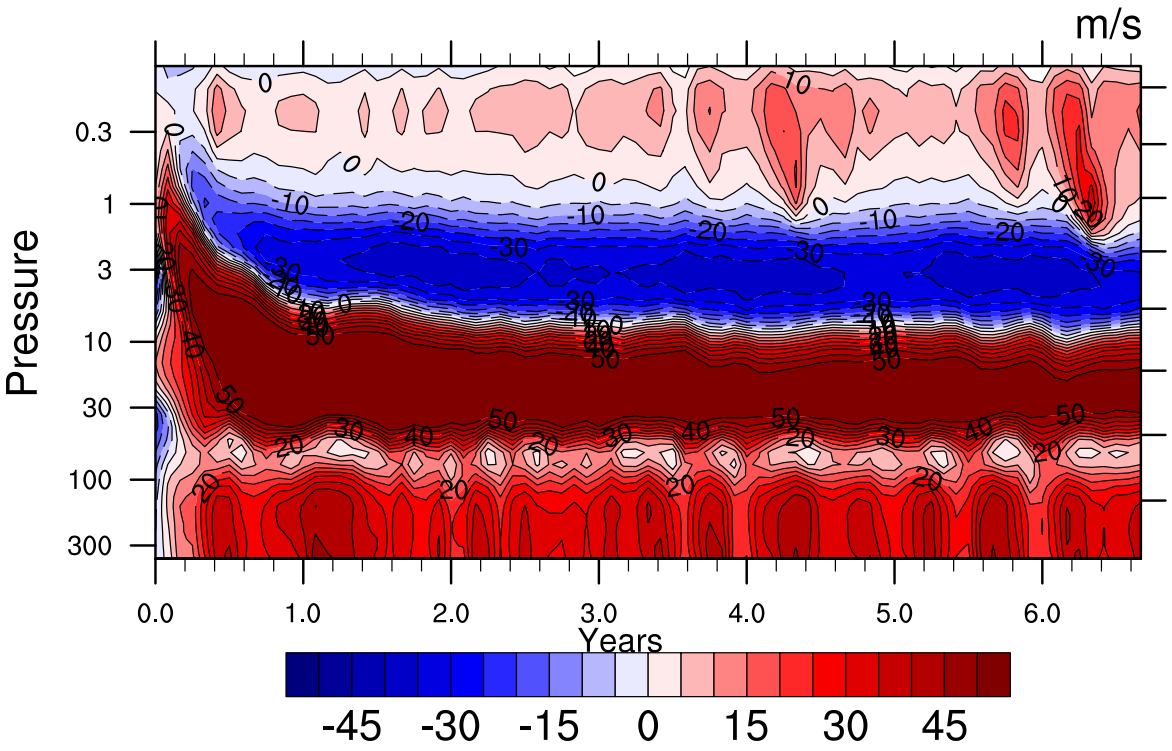

Figure 5.10: Monthly-mean zonal-mean zonal wind at the equator from SE dynamical cores with a prescribed GWD source spectrum launched <100 hPa.

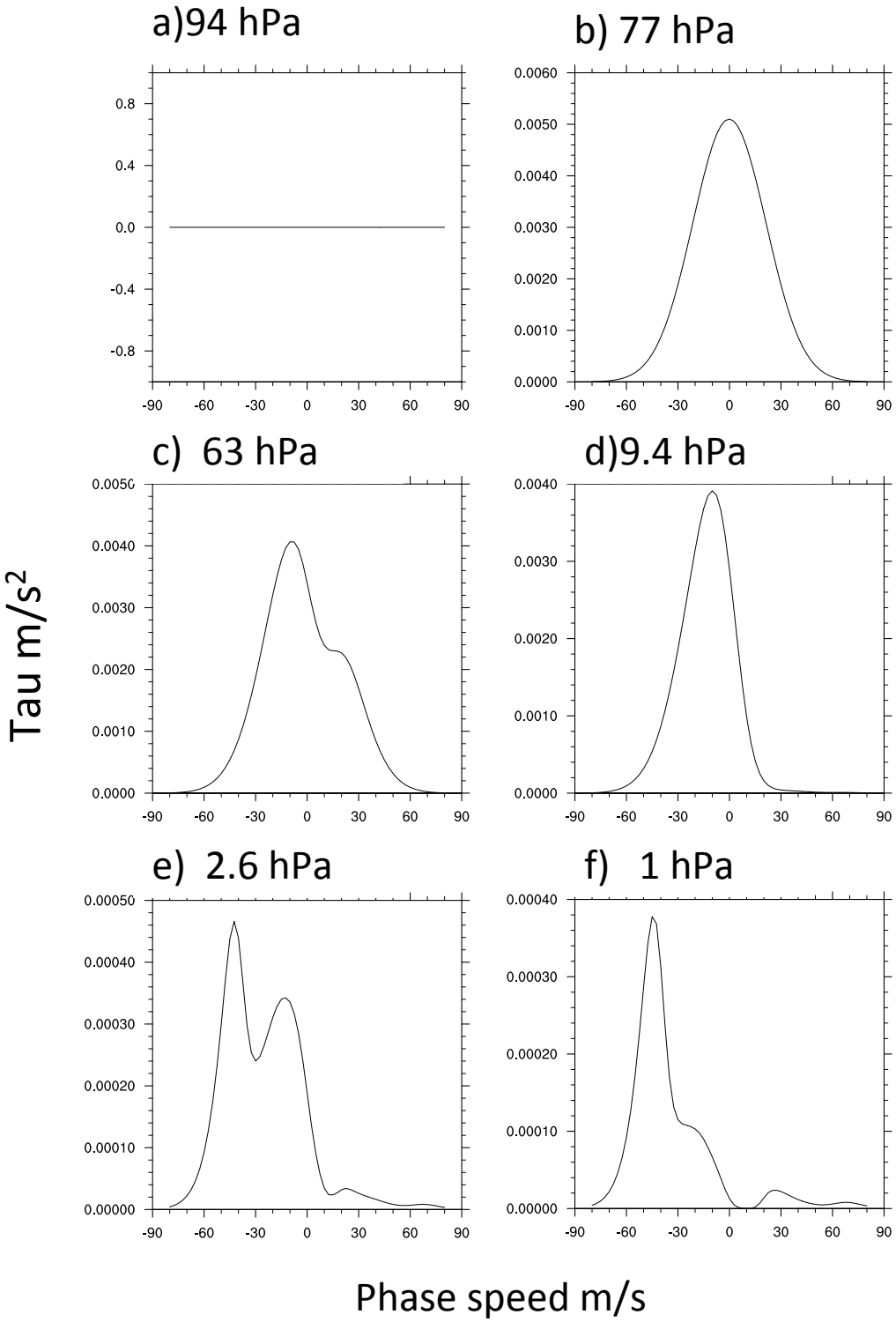

Figure 5.11: Averaged source stress τ_s with different wave phase speeds at different levels a) 94 hPa, b) 77 hPa, c) 63 hPa, d) 9.4 hPa, 3) 2.6 hPa, e) 1 hPa

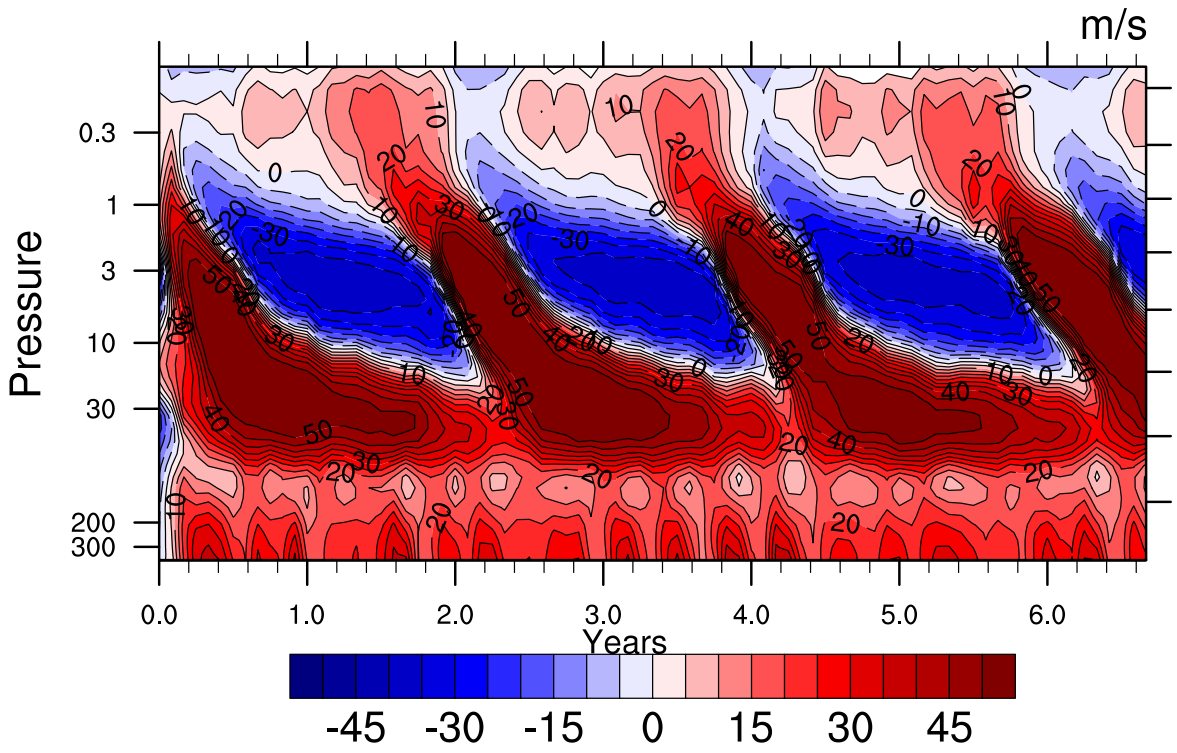

Figure 5.12: Monthly-mean zonal-mean zonal wind at the equator from SE dynamical cores with a prescribed GWD source spectrum launched at 200 hPa.

oscillation amplitude is high, about -30 to 50 m s^{-1}. The steady westerly jet at lower QBO domain in the dry prescribed GWD simulation in figure 5.7 is disappeared. However, the westerly phase at around 30 hPa is still strong and long-lasting.

Figure 5.13 shows a source stress analysis similar to figure 5.11. Figure 5.13a shows the source stress at 180 hPa. The source stress for all phase speeds is 0 m s^{-2}. At 156 hPa in figure 5.13b, the source stress shows a Gaussian shape. At 112 hPa in figure 5.13c, low phase speed westerly waves started to be dissipated. Low westerly phase speed waves continue to dissipate when traveling upward as shown in figure5.13d. At 9.4 hPa, the source stress is about 0.002 m s^{-2} compared to 0.004 m s^{-2} at 77 hPa. This indicates that easterly phase waves have already started to dissipate and deposit momentum to the background flow. This is expected since easterly jets exist in the QBO domain at 10 hPa. The easterly waves continue to be dissipated at a higher level (1hPa in figure 5.13).

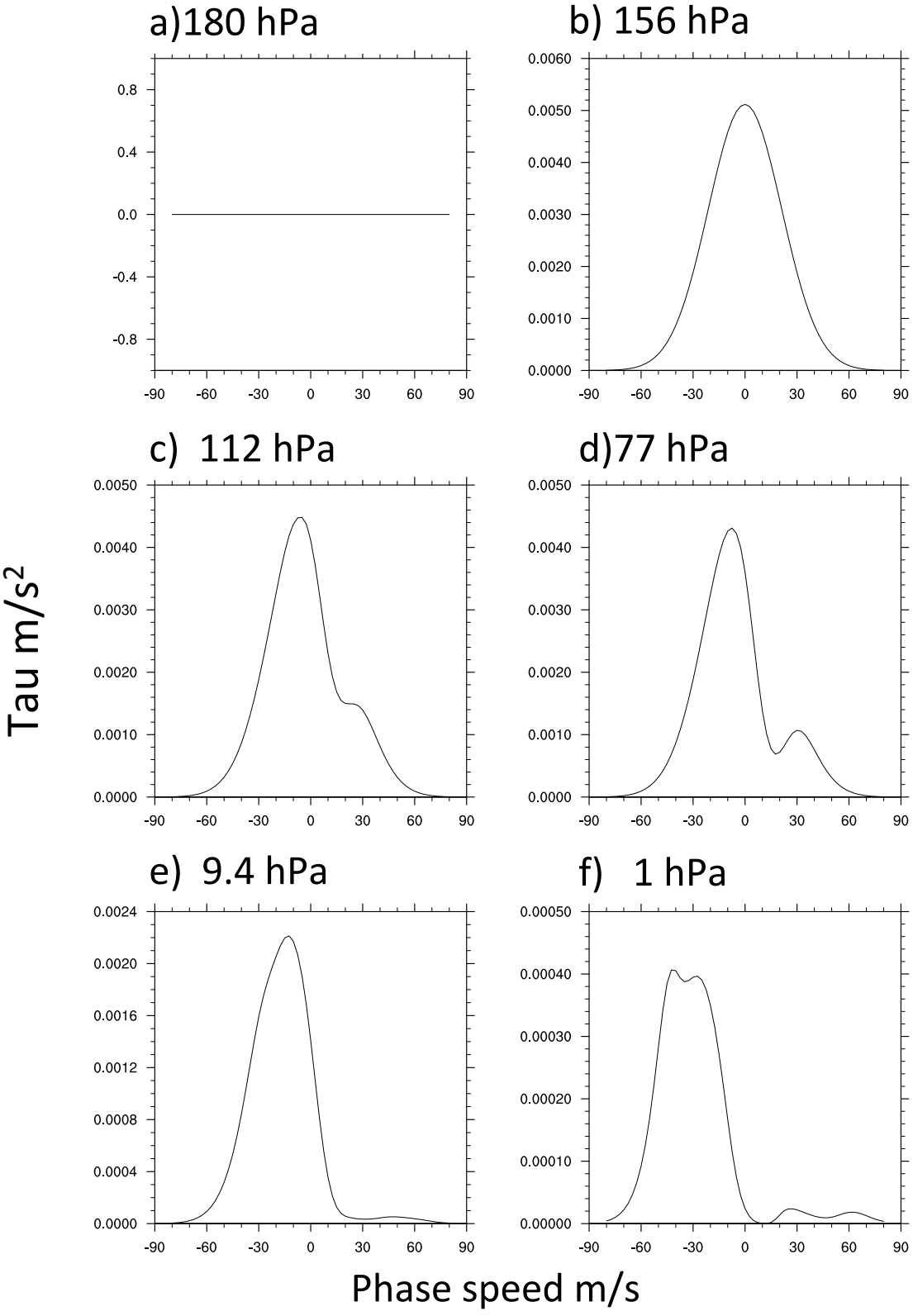

Figure 5.13: Averaged source stress τ_s with different wave phase speeds at different levels a) 180 hPa, b) 156 hPa, c) 112 hPa, d) 77 hPa, 3) 9.4 hPa, e) 1 hPa.

There are two possible reasons why this 200 hPa launch level simulation can produce a QBO-like oscillation. First, even though the source stress shows a similar magnitude of the wind acceleration, the air density at 200 hPa level is much denser than the 100 hPa. Therefore, the influence of this acceleration to the upper atmosphere is stronger. Secondly, the wind speed at the lower levels (between 200 and 100 hPa) is positive (eastward, westerly). Therefore additional westerly phase speed waves are absorbed at lower levels between 200 and 100 hPa, thereby reducing the imbalance of the westerly/easterly forcing in the upper level atmosphere.

5.6.3 Prescribed GWD launched at $\sim$ 500 hPa

A 2400-day simulation is conducted with prescribed GWD launching level at $\sim$ 500 hPa paired with same moist HS physics. As shown in figure 5.14. The QBO period is around 2.5 years. The oscillation amplitude is lower than the $<$ 200 hPa simulation, about -40 to 45 m s^{-1}. The strong and long-lasting westerly jet in the lower QBO domain around 30 hPa still exists, but is weaker and shorter (narrower). This simulation shows a slightly better westerly/easterly phase balance compared to the $<$ 200 hPa simulation.

Another source stress versus phase speed analysis is shown in figure 5.15. At 495 hPa in figure 5.15, no source stress is applied. At 413 hPa in figure 5.15b, we can already observe some slow phase speed wave that are dissipated in both the westerly and easterly domain. At the 181 hPa and 51 hPa levels, more westerly phase waves are dissipated (figure 5.15c and 5.15e). Similarly, at 2.6 hPa and 1hPa, more easterly phase waves are dissipated (figure 5.15e and 5.15f).

Overall, the $<$ 500 hPa simulation is very similar to the $<$ 200 hPa one. The major differences are that waves start to be dissipated at a lower level. This may be the reason why this $<$ 500 hPa simulation has a more balanced wave forcing and longer QBO-like period.

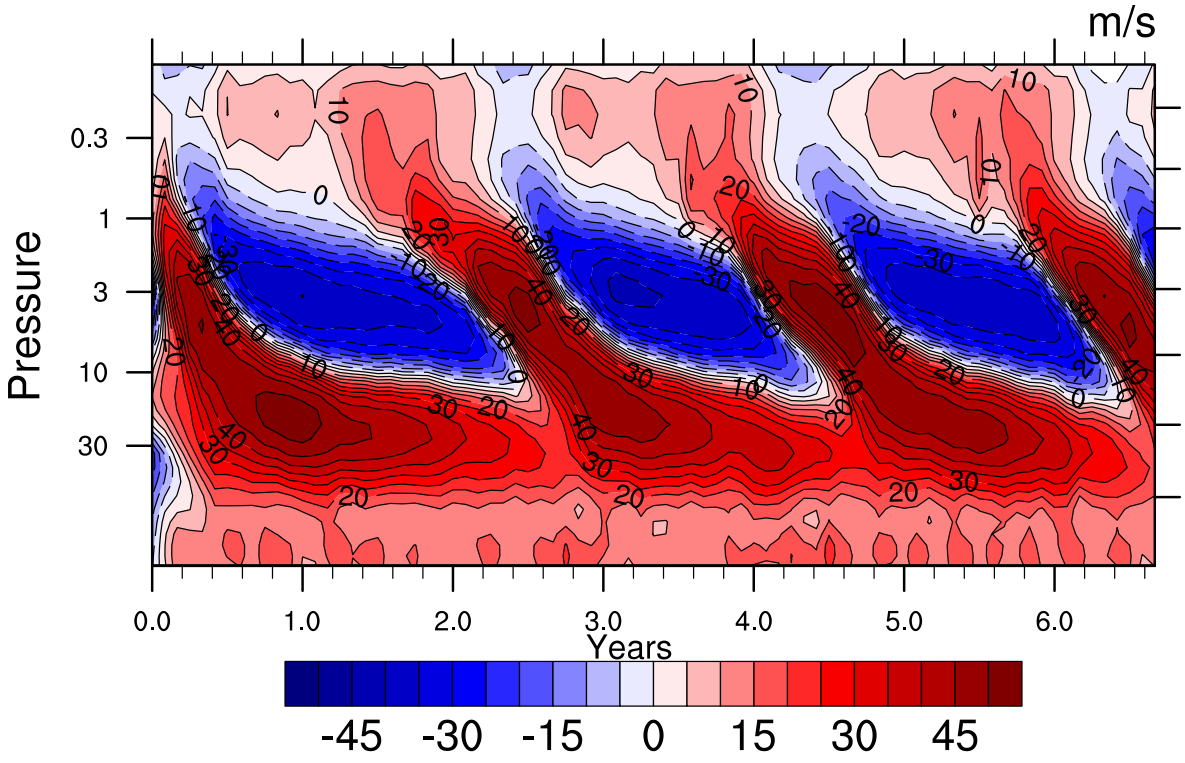

Figure 5.14: Monthly-mean zonal-mean zonal wind at the equator from SE dynamical cores with a prescribed GWD source spectrum launched at 500 hPa.

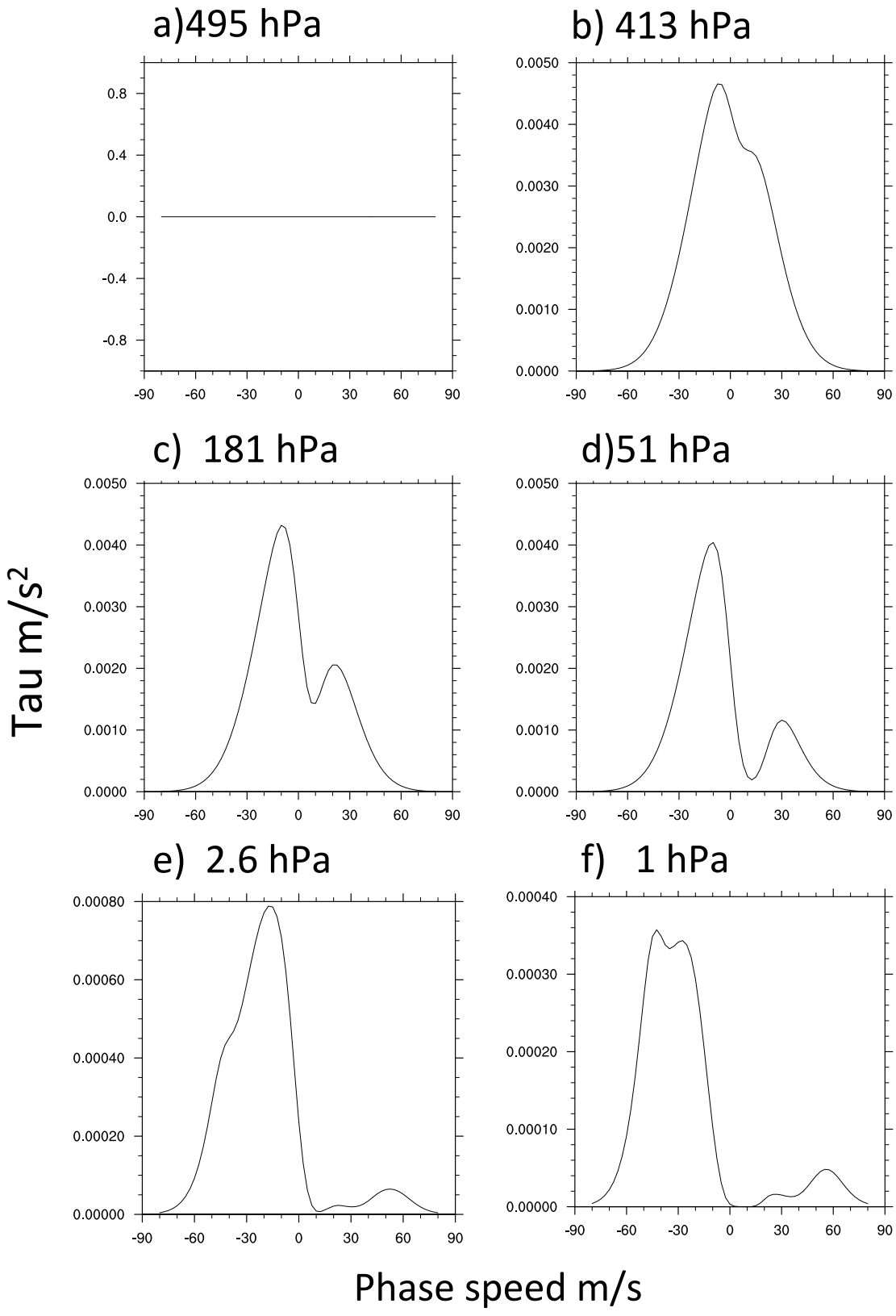

Figure 5.15: Averaged source stress τ_s with different wave phase speeds at different levels a) 495 hPa, b) 413 hPa, c) 181 hPa, d) 51 hPa, 3) 2.6 hPa, e) 1 hPa

5.7 Conclusion

In this portion of the thesis, we study two possible ways of improving the QBO simulation using an idealized framework. One is by including moist processes into the idealized model. The other one is by utilizing a simple GWD scheme.

The inclusion of moist processes shortens the QBO period in the SLD and SE simulations and enable a QBO oscillation in the FV simulation. The TEM analysis shows that the wave-mean flow interactions are enhanced in the moist SLD simulations. Moreover, the wavenumber frequency analysis reveals enhanced wave activities in both SLD and FV. Especially Kelvin waves are much more active in moist simulations. All equatorial waves are influenced by the Doppler shift due to the higher eastward background wind. This is consistent with observed higher Kelvin wave activities. The enhanced Kelvin waves provide more eastward acceleration and thereby modify the background flow.

The inclusion of GWD also shortens the QBO period and strengthens the QBO amplitudes in all four dynamical cores. In addition, the oscillations become more regular. However, westerly jets below the QBO oscillation domain still exist in the EUL and SE simulations. A TEM analysis is shown in order to evaluate the relative importance of different driving mechanisms in SLD. The GWD plays the most dominant role for the westward wind acceleration. Therefore enhanced easterly phases are observed in the SLD simulation.

Although both methods, moisture and GWD, can enhance the QBO simulations, their mechanisms and acceleration domains are different. We therefore combined both moist processes and GWD to include the two most important mechanisms in a single QBO-like simulation. The SE simulation with the modified moisture package has stronger zonal winds and a shorter QBO period. However, the period is still longer than the period in observations. The simulation with both moisture and GWD can be tuned to have a realistic QBO period. However, the QBO characteristics in

this simulation are still different from observations. More experiments with different tuning parameters or wave spectra are envisioned for future studies.

CHAPTER VI

Conclusions

The interactions of different model components in GCMs, including the dynamical cores and the full physics package, make it difficult to decide which phenomena are caused by which model component. In this study, we are mostly concerned about the role of the dynamical cores which are at the core of GCMs. Held-Suarez type idealized simulations, which consist of a temperature relaxation scheme and a Rayleigh friction for lower level winds, have been widely used to evaluate dry GCMs, especially the dynamical cores. The HS forcing simplifies the non-linear interaction between the dynamical cores and the physics package, therefore providing a more efficient way to compare the numerical methods used in GCMs. Such dry dynamical core tests also give valuable information about the diffusive behavior and the uncertainties in the numerical solutions. However, previous tests mostly focused on the troposphere. A modified version of the Held-Suarez test which was developed by *Williamson et al.* (1998) includes a stratospheric extension and has become a very useful tool for dynamical core inter-comparison with higher model tops and finer vertical level models.

This thesis provides idealized simulations of QBO-like oscillations and SSWs with different numerical methods. The QBO and SSWs are spontaneously generated by waves even without traditional wave triggering mechanisms, such as convection and topography. The waves that contribute to the QBO forcing have a wide range of

wavelengths. The simulation of the QBO requires the westerly and easterly wave forcing to have a matching magnitude in the QBO region. Therefore, the ability of a GCM to simulate a QBO is considered an important criterion which sheds light on the resolved wave activity in GCMs. Before this thesis, QBO-like oscillations have never been successfully simulated in dry idealized simulations. Therefore, this thesis provides a unique look at the processes in the dynamical cores and their dependence on the numerical design choices.

SSWs are the most important mode of variability in the polar stratosphere which are also forced by planetary waves. In nature, the planetary waves are also mostly generated by topography in the Northern Hemisphere. In nature SSWs are influenced by a variety of phenomena, including the solar cycle, ENSO, etc. The idealized SSW simulations in this thesis eliminate such influences and isolate the wave influence.

6.1 Summary

This thesis utilizes the NCAR Community Atmosphere Model CAM to simulate QBO-like oscillations and SSWs. Four dynamical cores are used to compare different numerical methods using the Held-Suarez and Held-Suarez-Williamson idealized physics packages. Additionally, we also employ a simple-physics package and GWD parameterization to assess their impact on the QBO simulations.

In Chapter II we present a QBO-like oscillation in the dry CAM SLD dynamical core that was driven by the Held-Suarez forcing with additional Rayleigh friction near the model top. The QBO-like signal has an average period of 43.5 months between 50 and 1 hPa. A wave-number frequency analysis is utilized to show that Doppler-shifted Kelvin, MRG, ER and EIR waves are resolved in the model without typical wave triggering mechanisms like cumulus convection. The TEM analysis show that the resolved wave forcing and vertical advection are the most important drivers of the QBO-like oscillation. The residual term in the TEM analysis counteracts the effects

of the resolved waves. Further analysis suggests that the residual term resembles the effects of momentum diffusion in the form of a fourth-order horizontal hyper-diffusion. This also indicates that the implicit numerical diffusion from the semi-Lagrangian scheme contributes considerably to the QBO-like oscillation.

A study of the QBO-like oscillations in the four GCM dynamical cores is shown in Chapter III. The CAM SLD, EUL, FV and SE dynamical cores are driven by the Held-Suarez forcing and additional Rayleigh friction as in Chap. II. This study shows that three (SLD, EUL and SE) out of the four CAM dynamical cores developed spontaneous QBO-like oscillations in the upper equatorial stratosphere, with varying QBO periods. The EUL and SE simulations closely resemble each other, but differ greatly from SLD. Their QBO-like periods are over 13 years long and the oscillation occupies the narrow band between 1-30 hPa. The initial wind shear is dissipated within the first six years of the FV simulation, and does not sustain the oscillation. A TEM analysis shows that resolved wave forcing is the dominant driver of the QBO. Implicit numerical or explicitly-added diffusion dominates the residual term in the TEM analysis and counteracts the resolved wave forcing. The analysis of the Brewer-Dobson circulation showed that the downward propagation of SLD's QBO is sped up by a mean desent in the QBO domain due to a strong secondary meridional circulation, whereas EUL's and SE's QBOs are slowed down by a mean ascent in the tropical stratosphere. A wavenumber-frequency analysis reveals relatively low wave activities in the FV simulation compared to the other three dynamical cores. We examined dynamical instability indicators as a potential wave triggering mechanism in the troposphere and wave dissipation mechanism in the stratosphere. Increased occurrences of strongly negative instability indicators in SLD, EUL and SE are related to their more vigorous wave activities and higher magnitudes of the resolved wave forcing in comparison to FV.

In Chap. IV we present SSW simulations with four different dynamical cores

in idealized simulations utilizing the Held-Suarez Williamson forcing and additional Rayleigh friction near the model top. The SLD simulation shows more frequent SSW events than the EUL, FV and SE simulations. The SLD simulation has a weaker latitudinal temperature gradient in the mid-latitude stratosphere than the other three dynamical cores. The polar jets in the SLD stratosphere are also weaker than the simulations with the other three dynamical cores. The TEM analysis shows stronger westward wind acceleration in the SLD simulation than the other three dynamical cores. Enhanced westward wavenumber 1 and 2 waves are observed before and during an SSW event. The interaction between SSW and the troposphere and stratospheric tropics are observed in this idealized simulation in SLD dynamical core. The SSW events influence the troposphere through the downward propagation of the negative NAM phase after around 30-60 days of the SSW initiation. In addition, a warm pole temperature bias is identified in the SLD simulation around the tropopause and lower stratosphere. The problem can be partially alleviated by increasing the vertical resolution of the SLD simulation.

Chapter V shows two possible ways of improving the idealized QBO simulation, including moist processes and using a simple GWD scheme. A simple physics package is used to include some key moist processes like large-scale condensation. The QBO periods are shortened and wave activities are enhanced. The Kelvin wave activities are greatly increased which provides more eastward acceleration to the background flow. A simple GWD scheme is utilized in the simulation with an prescribed wave spectrum. This shortens the QBO periods. A TEM analysis shows that the GWD forcing dominates the westward acceleration, therefore enhanced easterly phases are observed. In addition, an improved moist physics package with flow dependent GWD is discussed for the SE simulation. The QBO period is considerably improved.

6.2 Accomplishments and highlights of the research project

6.2.1 Significance

This work showcases successful QBO-like and SSW-like simulations with only the dynamical core and idealized Held-Suarez type physics. This shows that with a proper vertical and horizontal resolution and diffusion mechanisms, QBO-like oscillations can be simulated in a dry idealized experiments. The chapters give a thorough description and analysis of the QBO and SSW phenomena, as well as the general circulation. The insights from this thesis have the potential to influence the stratospheric research community and to enhance the overall predictability of QBOs and SSWs in climate models.

6.2.2 Relevance and future potential

Our idealized simulations eliminate numerous factors that can influence QBO simulations, such as the interaction between the physics package and the dynamical core, the seasonal cycle, the 11-year solar cycle and ENSO. Therefore, the idealized studies with spontaneous QBOs and SSWs might become a tool for other research areas, such as the Holton-Tan effect, the SSW initiation, or the testing of numerical methods, etc. The inclusion of moist processes and GWD provides extensions that allow an even more flexible assessment of idealized QBO simulations. The GWD can be tuned to have a more realistic QBO period. Therefore, it can provide a powerful tool for QBO related research.

6.2.3 Collaboration

This research project has established a collaboration between the University of Michigan (UM) and the National Center for Atmospheric Research (NCAR). The science team supporting this research was composed of Christiane Jablonowski (UM),

Jadwiga H. (Beres) Richter (NCAR) and Julio Bacmeister (NCAR).

6.3 Future work

With the foundation of this work, many questions remain and many more experiments have already been tested. Future work will include continued assessment of the sensitivity of different model parameters in the QBO simulations, model simulation with both moist processes and GWD, and further investigations of idealized SSW simulations with the inclusion of idealized topography.

The sensitivity test includes the influence of the vertical resolution on QBO simulations. Many previous studies have shown that an increase in vertical resolution helps resolve vertically propagating waves and can improve QBO simulation. However, in one of our tests with increasing vertical resolution in the SLD dynamical core, the QBO-like signal disappeared. The QBO can then be brought back with different explicitly-applied diffusion schemes. The QBO signal is also very sensitive to the horizontal resolution, sponge layer position and strength, diffusion mechanisms and their coefficients, and the temperature relaxation time scale. For example, modifying the sponge layer which lies higher than the QBO domain changes the QBO behavior. The underlying mechanisms for these phenomena have not been closely analyzed yet and a lot of questions remain to be answered.

The QBO simulation is also very sensitive to the temperature profile we use in the temperature relaxation scheme. As seen in Chapter IV the QBO slows down when including a polar vortex in the model. We have also observed a slow down of the QBO-like signal when including only a vertical temperature gradient in the stratosphere in addition to the Held-Suarez temperature profile. These simulation results have not been analyzed yet to identify the main factors influencing the QBO period and strength. Such simulations can also become model tools when testing different hypothesis for the QBO theory, and many more different temperature profiles

are worth trying.

The simulations with both moist processes and GWD scheme are another route that leads to interesting results. We paired a simple moist Held-Suarez package with a current GWD scheme in CAM which depends on the background flow. The heating term from large-scale condensation is used to launch gravity waves in this GWD scheme. However, there are several tuning parameters in the GWD scheme that have not been tested yet and the QBO behavior is still different from observations.

Many additional research tasks related to the SSW simulations are planned. For example, the influence of topography can be tested within this framework. In addition, the influence of topography on the NAM behavior can be analyzed. Furthermore, the influence of a seasonal cycle or ENSO can be tested by adding a time dependent term to the temperature profile. The coupling between SSWs and the troposphere is very strong in the winter time. Therefore, such simulation can also be used to study the influence of SSWs on surface weather and climate.

APPENDICES

APPENDIX A

Description of the Community Atmosphere Model (CAM 5)

The National Center for Atmospheric Research (NCAR) Community Atmosphere Model version 5 (CAM 5) represents the atmosphere component of the Community Earth System Mode, version 1 (CESM1). CAM is documented in detail in *Neale et al.* (2010). In this appendix, a brief overview of the model components is provided. The key features of the models which are related to this QBO and SSW study, including the dynamical cores and the numerical diffusion mechanisms are documented. Additional information about CAM's diffusive mechanisms are also provided in *Jablonowski and Williamson* (2011).

CAM5 model consists of two major parts, the dynamical core and the physics parameterization suite. The dynamical cores solves the fluid momentum and thermodynamics equation set. The physics are characterized by diabatic, subgrid-scale processes. The dynamical core and physical parameterizations interact each other in a non-linear fashion. The interaction in a full GCM makes it difficult to understand the main drivers of atmospheric phenomena. The difficulty can be alleviated when isolating the dynamical core and the physics parameterization via idealized model configurations.

A.1 CAM 5 dynamical cores

A.1.1 Semi-Lagrangian dynamical core (SLD)

The semi-Lagrangian dynamical core is a two-time-level semi-implicit semi-Lagrangian spectral transform dynamical core detailed in *Williamson and Olson* (1994). The SLD dynamical core uses a hybrid vertical coordinate (η) defined by

$$p(\eta, p_s) = A(\eta)p_0 + B(\eta)p_s \tag{A.1}$$

where p is pressure, p_s is surface pressure and $p_0 = 10^5$ Pa is a specified constant reference pressure. The coefficients A and B are defied at discrete model levels. This hybrid coordinate is terrain following at the Earth's surface but reduces to a pressure coordinate at some point above.

The governing equations are solved using a finite difference technique in the vertical and spectral method in the horizontal. The spectral transform method represents the prognostic variables in terms of coefficients of a truncated series of spherical harmonic functions. Horizontal derivatives and linear operations are performed in spectral space, whereas physical parameterizations and nonlinear operations are solved in grid point space.

The standard semi-implicit semi-Lagrangian method calculates departure points of Lagrangian particles which will be advected forevery the time step. The momentum and density equations are then solved along the trajectory of the particles (*Cotter et al.*, 2007). We do not apply explicit diffusion in the SLD dynamical core. The implicit numerical diffusion mostly triggered by the semi-Lagrangian interpolations provides diffusion that mimics 4th-order horizontal hyper diffusion (*McCalpin*, 1988). The SLD simulation uses a Gaussian grid in horizontal domain.

A.1.2 Eulerian dynamical core (EUL)

The EUL dynamical core is a three-time-level, semi-implicit Eulerian spectral transform model in vorticity-divergence form. It uses the same vertical coordinate and discretization as in the SLD dynamical core.

CAM 5.0 EUL contains a horizontal diffusion term for temperature T, vorticity ζ, and divergence δ to prevent spectral blocking and to provide reasonable kinetic energy spectra. The horizontal diffusion is a linear ∇^2 form on η surface in the top three levels of the model, with diffusion coefficient $K_2 = 2.5 \times 10^5$ m^2 s^{-1}. The ∇^2 diffusion near the model top absorbs vertically propagating wave energy and also influences the stratospheric jets.

The ∇^2 form of the horizontal diffusion is given by

$$F_\zeta = K_2[\nabla^2(\zeta + f) + 2(\zeta + f)/a^2] \tag{A.2}$$

$$F_\delta = K_2[\nabla^2\delta + 2(\delta/a^2)] \tag{A.3}$$

$$F_T = K_2\nabla^2 T \tag{A.4}$$

where a is the earth's radius. The bi-harmonic ∇^4 form of the diffusion operator is applied to all other levels in a similar fashion. In this particular study, the K_4 coefficient we use is $K_4 = 5 \times 10^{15}$ m^4 s^{-1} and

$$F_\zeta = -K_4[\nabla^4(\zeta + f) + (\zeta + f)(2/a^2)^2] \tag{A.5}$$

$$F_\delta = -K_4[\nabla^4\delta + \delta(2/a^2)^2] \tag{A.6}$$

$$F_T = -K_4\big[\nabla^4 T - \pi\frac{\partial T}{\partial p}\frac{\partial p}{\partial \pi}\nabla^4\Pi\big] \tag{A.7}$$

where p is pressure and is a function of π in the hybrid coordinate system, $\Pi = \ln\pi$. The EUL dynamical core uses a Gaussian grid same as the SLD.

A.1.3 Finite Volume dynamical core (FV)

The finite-volume discretization is based on a conservative "flux-form semi-Lagrangian" scheme described by *Lin and Rood* (1996) and *Lin and Rood* (1997). The vertical discretization is based on a floating Lagrangian coordinate that is remapped to an Eulerian reference grid after several subcycled dynamical time steps. The FV dynamics and physics are "time split". This means that all the prognostic variables are updated sequentially by the dynamical core and then the physics parameterizations.

The FV dynamical core utilizes a regular latitude-longitude grid with constant angle spacing. This leads to singularities at each geographic Pole, thereby inducing severe limitations on the stale time steps in the Polar region. Therefore a polar Fourier filter is applied poleward of the midlatitudes at approximately 36° - 40° N/S to lengthen the time step (*Whitehead et al.*, 2011) .

The FV's numerical diffusion mechanisms are implicit numerical diffusion via limiters and explicitly-applied 2nd-order horizontal divergence damping. The form of the second-order divergence damping is given by

$$\frac{\partial u}{\partial t} = ... + \frac{1}{acos\phi}\frac{\partial}{\partial \lambda}(\nu_2 D) \tag{A.8}$$

$$\frac{\partial v}{\partial t} = ... + \frac{1}{a}\frac{\partial}{\partial \phi}(\nu_2 D) \tag{A.9}$$

where u and v are the zonal and meridional components of velocity, ϕ is the latitude and λ is longitude. The horizontal divergence D is given by

$$D = \frac{1}{acos\phi}\Big[\frac{\partial u}{\partial \lambda} + \frac{\partial (vcos\phi)}{\partial \phi}\Big] \tag{A.10}$$

We then evolve

$$\frac{\partial D}{\partial t} = ... + \nabla^2(\nu_2 D) \tag{A.11}$$

This Laplacian-type (∇^2) diffusion of the divergence damps all scales, but with more

damping at higher wavenumbers (*Whitehead et al.*, 2011).

A.1.4 Spectral Element dynamical core (SE)

The SE dynamical core is based on a continuous Galerkin spectral finite element method and has been designed for fully unstructured quadrilateral meshes. It uses a cubed-sphere grid and explicit Runge-Kutta time stepping scheme.

A horizontal hyper-viscosity operator is applied to the momentum and temperature equations in a similar form of the EUL with same coefficient (K_4).

BIBLIOGRAPHY

BIBLIOGRAPHY

Alexander, M. J., et al. (2010), Recent developments in gravity-wave effects in climate models and the global distribution of gravity-wave momentum flux from observations and models, *Quart. J. Roy. Meteor. Soc.*, *136*, 1103–1124.

Andrews, D. G. (1987), On the interpretation of the Eliassen-Palm flux divergence, *Quart. J. Roy. Meteor. Soc.*, *113*, 323–338.

Andrews, D. G., J. D. Mahlman, and R. W. Sinclair (1983), Eliassen-Palm diagnostics of wave-mean flow interaction in the GFDL "SKYHI" general circulation model, *J. Atmos. Sci.*, *40*, 2768–2784.

Andrews, D. G., J. R. Holton, and C. B. Leovoy (1987), *Middle Atmosphere Dynamics*, *International Geophysics Series*, vol. 40, 489 pp., Academic Press.

Baldwin, M. P. (2003), Comment on "Tropospheric response to stratospheric perturbations in a relatively simple general circulation model" by Lorenzo M. Polvani and Paul J. Kushner, *Geophys. Res. Let.*, *30*, 1812, doi:10.1029/2003GL017793.

Baldwin, M. P., and T. J. Dunkerton (2001), Stratospheric Harbingers of Anomalous Weather Regimes, *Science*, *294*, 581–584, doi:10.1126/science.1063315.

Baldwin, M. P., et al. (2001), The Quasi-Biennial Oscillation, *Rev. Geophysics*, *39*(2), 179–229.

Beres, J. H., R. R. Garcia, B. A. Boville, and F. Sassi (2005), Implementation of a gravity wave source spectrum parameterization dependent on the properties of convection in the Whole Atmosphere Community Climate model (WACCM), *J. Geophys. Res.*, *110*, d10108,doi:10,1029/2004JD005504.

Boville, B. (1995), Middle atmosphere version of CCM2 (MACCM2): Annual cycle and interannual variability, *Journal of Geophysical Research: Atmospheres (1984–2012)*, *100*(D5), 9017–9039.

Boville, B. A. (1986), Wave-mean flow interactions in a general circulation model of the troposphere and stratosphere, *J. Atmos. Sci.*, *43*, 1711–1725.

Boville, B. A. (1991), Sensitivity of simulated climate to model resolution, *J. Climate*, *4*, 469–485.

Charlton, A. J., and L. M. Polvani (2007), A new look at stratospheric sudden warmings. Part I: Climatology and modeling benchmarks., *Journal of Climate*, *20*(3).

Charlton, A. J., L. M. Polvani, J. Perlwitz, F. Sassi, E. Manzini, K. Shibata, S. Pawson, J. E. Nielsen, and D. Rind (2007), A new look at stratospheric sudden warmings. Part II: Evaluation of numerical model simulations, *Journal of Climate*, *20*(3), 470–488.

Charney, J. G., and M. E. Stern (1962), On the stability of internal baroclinic jets in a rotating atmosphere, *J. Atmos. Sci.*, *19*, 159–172.

Choi, W., H. Lee, W. B. Grant, J. H. Park, J. R. Holton, K.-M. Lee, and B. Naujokat (2002), On the secondary meridional circulation associated with the quasi-biennial oscillation, *Tellus Series B*, *54*, 395–406, doi:10.1034/j.1600-0889.2002.201286.x.

Chshyolkova, T., A. H. Manson, C. E. Meek, S. K. Avery, D. Thorsen, J. W. MacDougall, W. Hocking, Y. Murayama, and K. Igarashi (2005), Planetary wave coupling in the middle atmosphere (20-90km): A CUJO study involving TOMS, MetO and MF radar data, *Annales Geophysicae*, *23*, 1103–1121, doi:10.5194/angeo-23-1103-2005.

Cotter, C., J. Frank, and S. Reich (2007), The remapped particle-mesh semi-lagrangian advection scheme, *Quarterly Journal of the Royal Meteorological Society*, *133*(622), 251–260.

Dennis, J., J. Edwards, K. J. Evans, O. N. Guba, P. H. Lauritzen, A. A. Mirin, A. St-Cyr, M. A. Taylor, and P. H. Worley (2012), CAM-SE: A scalable spectral element dynamical core for the Community Atmosphere Model, *Int. J. High Perf. Comput. Appl.*, *26*, 74–89, doi:10.1177/1094342011428142.

Dunkerton, T. J. (1981), On the inertial stability of the equatorial middle atmosphere., *Journal of Atmospheric Sciences*, *38*, 2354–2364.

Dunkerton, T. J. (1989), Theory of internal gravity wave saturation, in *Middle Atmosphere*, pp. 373–397, Springer.

Dunkerton, T. J. (1997), The role of gravity waves in the quasi-biennial oscillation, *Journal of Geophysical Research*, *102*, 26,053–26,076, doi:10.1029/96JD02999.

Dunkerton, T. J. (2000), Inferences about QBO Dynamics from the Atmospheric 'Tape Recorder' Effect., *J. Atmos. Sci.*, *57*, 230–246, doi:10.1175/1520-0469(2000)057<0230:IAQDFT>2.0.CO;2.

Dunkerton, T. J., and N. Butchart (1984), Propagation and selective transmission of internal gravity waves in a sudden warming, *Journal of the atmospheric sciences*, *41*(8), 1443–1460.

Ebdon, R. (1960), Notes on the wind flow at 50 mb in tropical and sub-tropical regions in january 1957 and january 1958, *Quarterly Journal of the Royal Meteorological Society*, *86*(370), 540–542.

Edmon, H. J., Jr., B. J. Hoskins, and M. E. McIntyre (1980), Eliassen-Palm Cross Sections for the Troposphere., *Journal of Atmospheric Sciences*, *37*, 2600–2616, doi:10.1175/1520-0469(1980)037<2600:EPCSFT>2.0.CO;2.

Erlebach, P., U. Langematz, and S. Pawson (1996), Simulations of stratospheric sudden warmings in the berlin troposphere-stratosphere-mesosphere gcm, in *Annales Geophysicae*, vol. 14, pp. 443–463, Springer.

Ern, M., and P. Preusse (2009), Quantification of the contribution of equatorial Kelvin waves to the QBO wind reversal in the stratosphere, *Geophys. Res. Lett.*, *36*, 21,801.

Ern, M., F. Ploeger, P. Preusse, J. C. Gille, L. J. Gray, S. Kalisch, M. G. Mlynczak, J. M. Russell, and M. Riese (2014), Interaction of gravity waves with the QBO: A satellite perspective, *J. Geophys. Res. (Atmospheres)*, *119*, 2329–2355, doi: 10.1002/2013JD020731.

Evan, S., M. J. Alexander, and J. Dudhia (2012), WRF simulations of convectively generated gravity waves in opposite QBO phases, *J. Geophys. Res. (Atmospheres)*, *117*(D16), D12,117, doi:10.1029/2011JD017302.

Flury, T., D. L. Wu, and W. G. Read (2013), Variability in the speed of the Brewer-Dobson circulation as observed by Aura/MLS, *Atmospheric Chemistry and Physics*, *13*, 4563–4575, doi:10.5194/acp-13-4563-2013.

Fritts, D. C. (1982), Shear excitation of atmospheric gravity waves, *J. Atmos. Sci.*, *39*(9), 1936–1952.

Fritts, D. C. (1984), Shear excitation of atmospheric gravity waves. Part II: Nonlinear radiation from a free shear layer, *J. Atmos. Sci.*, *41*(4), 524–537.

Fritts, D. C., and M. J. Alexander (2003), Gravity wave dynamics and effects in the middle atmosphere, *Reviews of Geophysics*, *41*, 1003, doi:10.1029/2001RG000106.

Fritts, D. C., and P. K. Rastogi (1985), Convective and dynamical instabilities due to gravity wave motions in the lower and middle atmosphere: Theory and observations, *Radio Science*, *20*(6), 1247–1277.

Garcia, R. R., T. J. Dunkerton, R. S. Lieberman, and R. A. Vincent (1997), Climatology of the semiannual oscillation of the tropical middle atmosphere, *Journal of Geophysical Research: Atmospheres (1984–2012)*, *102*(D22), 26,019–26,032.

Garcia, R. R., D. R. Marsh, D. E. Kinnison, B. A. Boville, and F. Sassi (2007), Simulation of secular trends in the middle atmosphere, 1950-2003, *Journal of Geophysical Research (Atmospheres)*, *112*, D09301, doi:10.1029/2006JD007485.

Garfinkel, C. I., and D. L. Hartmann (2011a), The Influence of the Quasi-Biennial Oscillation on the Troposphere in Winter in a Hierarchy of Models. Part I: Simplified Dry GCMs, *Journal of Atmospheric Sciences*, *68*, 1273–1289, doi: 10.1175/2011JAS3665.1.

Garfinkel, C. I., and D. L. Hartmann (2011b), The influence of the quasi-biennial oscillation on the troposphere in winter in a hierarchy of models. part ii: Perpetual winter WACCM runs, *Journal of the Atmospheric Sciences*, *68*(9), 2026–2041, doi: 10.1175/2011JAS3702.1.

Garfinkel, C. I., T. A. Shaw, D. L. Hartmann, and D. W. Waugh (2012), Does the Holton-Tan Mechanism Explain How the Quasi-Biennial Oscillation Modulates the Arctic Polar Vortex?, *Journal of Atmospheric Sciences*, *69*, 1713–1733, doi: 10.1175/JAS-D-11-0209.1.

Gerber, E. P., and L. M. Polvani (2009), Stratosphere-Troposphere Coupling in a Relatively Simple AGCM: The Importance of Stratospheric Variability, *Journal of Climate*, *22*, 1920, doi:10.1175/2008JCLI2548.1.

Giorgetta, M. A., E. Manzini, and E. Roeckner (2002), Forcing of the quasi-biennial oscillation from a broad spectrum of atmospheric waves, *Geophys. Res. Let.*, *29*(8), doi:10.1029/2002GL014,756.

Giorgetta, M. A., E. Manzini, E. Roeckner, M. Esch, and L. Bengtsson (2006), Climatology and forcing of the Quasi-Biennial Oscillation in the MAECHAM5 model, *J. Climate*, *19*, 3882–3901.

Grose, W. L., and K. V. Haggard (1981), Numerical simulation of a sudden stratospheric warming with a three-dimensional, spectral, quasi-geostrophic model, *Journal of the Atmospheric Sciences*, *38*(7), 1480–1497, doi:10.1175/1520 − 0469(1981)038 < 1480 : $NSOASS > 2.0.CO; 2$.

Hamilton, K. (1984), Mean Wind Evolution through the Quasi-Biennial Cycle in the Tropical Lower Stratosphere., *Journal of Atmospheric Sciences*, *41*, 2113–2125, doi:10.1175/1520-0469(1984)041<2113:MWETTQ>2.0.CO;2.

Hamilton, K., R. J. Wilson, and R. S. Hemler (2001), Spontaneous Stratospheric QBO-like Oscillations Simulated by the GFDL SKYHI General Circulation Model, *J. Atmos. Sci.*, *58*, 3271–3292.

Hayashi, H., M. Shiotani, and J. C. Gille (2002), Horizontal wind disturbances induced by inertial instability in the equatorial middle atmosphere as seen in rocketsonde observations, *Journal of Geophysical Research: Atmospheres*, *107*(D14), ACL 18–1–ACL 18–12, doi:10.1029/2001JD000922.

Haynes, P. H. (1998), The latitudinal structure of the quasi-biennial oscillation, *Quart. J. Roy. Meteor. Soc.*, *124*, 2645–2670, doi:10.1002/qj.49712455206.

Held, I. M., and M. J. Suarez (1994), A proposal for the intercomparison of the dynamical cores of atmospheric general circulation models, *Bull. Amer. Meteor. Soc.*, *75*(10), 1825–1830.

Hitchcock, P., and I. R. Simpson (2014), The Downward Influence of Stratospheric Sudden Warmings, *Journal of the Atmospheric Sciences*, *71*(10), 3856–3876, doi: 10.1175/JAS-D-14-0012.1.

Hitchman, M. H., C. B. Leovy, J. C. Gille, and P. L. Bailey (1987), Quasi-Stationary Zonally Asymmetric Circulations in the Equatorial Lower Mesosphere, *J. Atmos. Sci.*, *44*, 2219–2236, doi:10.1175/1520-0469(1987)044<2219:QSZACI>2.0.CO;2.

Holton, J. R. (1976), A semi-spectral numerical model for wave-mean flow interactions in the stratosphere - Application to sudden stratospheric warmings, *Journal of Atmospheric Sciences*, *33*, 1639–1649, doi:10.1175/1520-0469(1976)033<1639:ASSNMF>2.0.CO;2.

Holton, J. R. (1984), The generation of mesospheric planetary waves by zonally asymmetric gravity wave breaking, *Journal of the atmospheric sciences*, *41*(23), 3427–3430.

Holton, J. R. (2004), *An Introduction to Dynamic Meteorology*, Fourth ed., Academic Press, Inc., 535 pp.

Holton, J. R., and R. S. Lindzen (1972), An Updated Theory for the Quasi-Biennial Cycle of the Tropical Stratosphere, *J. Atmos. Sci.*, *29*, 1076–1080, doi: 10.1175/1520-0469(1972)029<1076:AUTFTQ>2.0.CO;2.

Holton, J. R., and H.-C. Tan (1980), The Influence of the Equatorial Quasi-Biennial Oscillation on the Global Circulation at 50 mb., *Journal of Atmospheric Sciences*, *37*, 2200–2208, doi:10.1175/1520-0469(1980)037<2200:TIOTEQ>2.0.CO;2.

Horinouchi, T., and S. Yoden (1998), Wave-mean flow interaction associated with a QBO-like oscillation simulated in a simplified GCM, *J. Atmos. Sci.*, *55*, 502–526.

Hsu, C.-P. F. (1981), A Numerical Study of the Role of Wave-Wave Interactions during Sudden Stratospheric Warmings., *Journal of Atmospheric Sciences*, *38*, 189–214, doi:10.1175/1520-0469(1981)038<0189:ANSOTR>2.0.CO;2.

Jablonowski, C., and D. L. Williamson (2011), The pros and cons of diffusion, filters, and fixers in atmospheric general circulation models, in *Numerical Techniques for Global Atmospheric Models*, *Lecture Notes in Science and Engineering*, vol. 80, edited by P. H. Lauritzen, C. Jablonowski, M. A. Taylor, and R. D. Nair, pp. 381–493, Springer.

Jucker, M., S. Fueglistaler, and G. Vallis (2013), Maintenance of the stratospheric structure in an idealized general circulation model, *Journal of the Atmospheric Sciences*, *70*(11), 3341–3358.

Jucker, M., S. Fueglistaler, and G. K. Vallis (2014), Stratospheric sudden warmings in an idealized gcm, *Journal of Geophysical Research: Atmospheres*, *119*(19), 11,054–11,064, doi:10.1002/2014JD022170.

Kawatani, Y., S. Watanabe, K. Sato, T. J. Dunkerton, S. Miyahara, and M. Takahashi (2010), The Roles of Equatorial Trapped Waves and Internal Inertia-Gravity Waves in Driving the Quasi-Biennial Oscillation. Part I: Zonal Mean Wave Forcing, *Journal of Atmospheric Sciences*, *67*, 963–980, doi:10.1175/2009JAS3222.1.

Kawatani, Y., K. Hamilton, and S. Watanabe (2011), The Quasi-Biennial Oscillation in a Double CO2 Climate, *Journal of Atmospheric Sciences*, *68*, 265–283, doi:10.1175/2010JAS3623.1.

Kawatani, Y., K. Hamilton, and A. Noda (2012), The Effects of Changes in Sea Surface Temperature and CO_2 Concentration on the Quasi-Biennial Oscillation, *J. Atmos. Sci.*, *69*, 1734–1749.

Kiladis, G. N., M. C. Wheeler, P. T. Haertel, K. H. Straub, and P. E. Roundy (2009), Convectively coupled equatorial waves, *Reviews of Geophysics*, *47*(2), doi:10.1029/2008RG000266.

Kim, Y., S. Eckermann, and H. Chun (2003), An overview of the past, present and future of gravity-wave drag parametrization for numerical climate and weather prediction models - Survey article, *ATMOSPHERE-OCEAN*, *41*(1), 65–98.

Kim, Y.-H., A. C. Bushell, D. R. Jackson, and H.-Y. Chun (2013), Impacts of introducing a convective gravity-wave parameterization upon the QBO in the Met Office Unified Model, *Geophys. Res. Lett.*, *40*, 1873–1877, doi:10.1002/grl.50353.

Krismer, T. R. (2014), Wave-mean flow interactions driving the quasi-biennial oscillation in echam6, *Reports on Earth System Science 149*, Max Planck Institute for Meteorology, Hamburg, Germany, available from http://www.mpimet.mpg.de/en/wissenschaft/publikationen/berichte-erdsystemforschung.html.

Krismer, T. R., and M. A. Giorgetta (2014), Wave Forcing of the Quasi-Biennial Oscillation in the Max Planck Institute Earth System Model, *J. Atmos. Sci.*, *71*, 1985–2006.

Krüger, K., B. Naujokat, and K. Labitzke (2005), The unusual midwinter warming in the southern hemisphere stratosphere 2002: A comparison to northern hemisphere phenomena, *Journal of the Atmospheric Sciences*, *62*(3), 603–613.

Kushner, P. J., and L. M. Polvani (2004), Stratosphere-troposphere coupling in a relatively simple agcm: The role of eddies, *Journal of climate*, *17*(3), 629–639.

Labitzke, K. (1965), On the mutual relation between stratosphere and troposphere during periods of stratospheric warmings in winter, *J. Appl. Meteorology*, *4*, 91–99.

Lane, T. P., and M. W. Moncrieff (2008), Stratospheric gravity waves generated by multiscale tropical convection, *Journal of the Atmospheric Sciences*, *65*(8), 2598–2614.

Larsen, M., W. Swartz, and R. Woodman (1982), Gravity-wave generation by thunderstorms observed with a vertically-pointing 430 mhz radar, *Geophysical Research Letters*, *9*(5), 571–574.

Lauritzen, P. H., C. Jablonowski, M. Taylor, and R. Nair (2011), *Numerical techniques for global atmospheric models*, vol. 80, Springer.

Lieberman, R. S., D. M. Riggin, and D. E. Siskind (2013), Stationary waves in the wintertime mesosphere: Evidence for gravity wave filtering by stratospheric planetary waves, *Journal of Geophysical Research: Atmospheres*, *118*(8), 3139–3149, doi:10.1002/jgrd.50319.

Limpasuvan, V., D. W. J. Thompson, and D. L. Hartmann (2004), The Life Cycle of the Northern Hemisphere Sudden Stratospheric Warmings., *Journal of Climate*, *17*, 2584–2597, doi:10.1175/1520-0442(2004)017<2584:TLCOTN>2.0.CO;2.

Lin, S.-J. (2004), A "vertically Lagrangian" finite-volume dynamical core for global models, *Mon. Wea. Rev.*, *132*, 2293–2307.

Lin, S.-J., and R. B. Rood (1996), Multidimensional flux-form semi-Lagrangian transport scheme, *Mon. Wea. Rev.*, *124*, 2046–2070.

Lin, S.-J., and R. B. Rood (1997), An explicit flux-form semi-Lagrangian shallow water model on the sphere, *Quart. J. Roy. Meteor. Soc.*, *123*, 2477–2498.

Lindzen, R. S. (1981), Turbulence and stress owing to gravity wave and tidal breakdown, *J. Geophy. Res.*, *86*, 9707–9714, doi:10.1029/JC086iC10p09707.

Lindzen, R. S., and J. R. Holton (1968), A Theory of the Quasi-Biennial Oscillation., *Journal of Atmospheric Sciences*, *25*, 1095–1107, doi:10.1175/1520-0469(1968)025<1095:ATOTQB>2.0.CO;2.

Lott, F., and L. Guez (2013), A stochastic parameterization of the gravity waves due to convection and its impact on the equatorial stratosphere, *J. Geophys. Res. (Atmospheres)*, *118*, 8897–8909, doi:10.1002/jgrd.50705.

Magaña, V., and M. Yanai (1995), Mixed Rossby-Gravity Waves Triggered by Lateral Forcing, *J. Atmos. Sci.*, *52*, 1473–1486, doi:$10.1175/1520-0469(1995)052<1473:MRWTBL>2.0.CO;2$.

Manney, G. L., J. L. Sabutis, D. R. Allen, W. A. Lahoz, A. A. Scaife, C. E. Randall, S. Pawson, B. Naujokat, and R. Swinbank (2005), Simulations of Dynamics and Transport during the September 2002 Antarctic Major Warming., *Journal of Atmospheric Sciences*, *62*, 690–707, doi:10.1175/JAS-3313.1.

Manzini, E., and L. Bengtsson (1996), Stratospheric climate and variability from a general circulation model and observations, *Climate dynamics*, *12*(9), 615–639.

Martius, O., L. M. Polvani, and H. C. Davies (2009), Blocking precursors to stratospheric sudden warming events, *Geophys. Res. Lett.*, *36*, L14,806.

Maruyama, T. (1994), Upward transport of westerly momentum due to disturbances of the equatorial lower stratosphere in the period range about 2 days.-a singapore data analysis for 1983-1993., *J. Meteor. Soc. Japan*, *72*, 423–431.

Matsuno, T. (1971), A dynamical model of the stratospheric sudden warming, *Journal of the Atmospheric Sciences*, *28*(8), 1479–1494.

McCalpin, J. D. (1988), A Quantitative Analysis of the Dissipation Inherent in Semi-Lagrangian Advection, *Mon. Wea. Rev.*, *116*, 2330–2336.

McFarlane, N. (1987), The effect of orographically excited gravity wave drag on the general circulation of the lower stratosphere and troposphere, *Journal of the atmospheric sciences*, *44*(14), 1775–1800.

Naito, Y., and S. Yoden (2006), Behavior of Planetary Waves before and after Stratospheric Sudden Warming Events in Several Phases of the Equatorial QBO., *Journal of Atmospheric Sciences*, *63*, 1637–1649, doi:10.1175/JAS3702.1.

Naito, Y., M. Taguchi, and S. Yoden (2003), A parameter sweep experiment on the effects of the equatorial QBO on stratospheric sudden warming events., *Journal of the atmospheric sciences*, *60*(11).

Naoe, H., and K. Shibata (2010), Equatorial quasi-biennial oscillation influence on northern winter extratropical circulation, *Journal of Geophysical Research (Atmospheres)*, *115*, D19102, doi:10.1029/2009JD012952.

Naujokat, B. (1986), An Update of the Observed Quasi-Biennial Oscillation of the Stratospheric Winds over the Tropics, *J. Atmos. Sci.*, *43*, 1873–1880, doi:10.1175/1520-0469(1986)043<1873:AUOTOQ>2.0.CO;2.

Naujokat, B., K. Krüger, K. Matthes, J. Hoffmann, M. Kunze, and K. Labitzke (2002), The early major warming in December 2001–exceptional?, *Geophysical research letters*, *29*(21), 19–1.

Neale, R. B., et al. (2010), Description of the NCAR Community Atmosphere Model (CAM 5.0), *NCAR Tech. Note NCAR/TN-486+STR*, National Center for Atmospheric Research, Boulder, Colorado, 282 pp.

Nissen, K. M., P. Braesicke, and U. Langematz (2000), QBO, SAO, and tropical waves in the Berlin TSM GCM: Sensitivity to radiation, vertical resolution, and convection, *J. Geophys. Res.*, *105*, 24,771–24,790, doi:10.1029/2000JD900270.

O'Neill, A. (1980), The dynamics of stratospheric warmings generated by a general circulation model of the troposphere and stratosphere, *Quarterly Journal of the Royal Meteorological Society*, *106*(450), 659–690, doi:10.1002/qj.49710645002.

Orr, A., P. Bechthold, J. Scinocca, M. Ern, and M. Janiskova (2010), Improved middle atmosphere climate and forecasts in the ECMWF model through a non-orographic gravity wave drag parameterization, *J. Climate*, *23*, 5905–5926.

Osprey, S. M., L. J. Gray, S. C. Hardiman, N. Butchart, and T. J. Hinton (2013), Stratospheric Variability in Twentieth-Century CMIP5 Simulations of the Met Office Climate Model: High Top versus Low Top, *J. Climate*, *26*, 1595–1606, doi: 10.1175/JCLI-D-12-00147.1.

O'Sullivan, D., and P. Chen (1996), Modeling the quasi biennial oscillation's influence on isentropic tracer transport in the subtropics, *Journal of Geophysical Research: Atmospheres (1984–2012)*, *101*(D3), 6811–6821.

O'Sullivan, D. J., and M. H. Hitchman (1992), Inertial instability and Rossby wave breaking in a numerical model, *J. Atmos. Sci.*, *49*, 991–1002.

Pascoe, C. L., L. J. Gray, S. A. Crooks, M. N. Juckes, and M. P. Baldwin (2005), The quasi-biennial oscillation: Analysis using ERA–40 data, *J. Geophys. Res.*, *110*, D08,105.

Pawson, S., and M. Fiorino (1998), A comparison of reanalyses in the tropical stratosphere. Part 2: the quasi-biennial oscillation, *Climate Dynamics*, *14*, 645–658.

Peña-Ortiz, C., P. Ribera, R. Garcia, R. R.a-Herrera, M. A. Giorgetta, and R. R. Garcia, R. R.a (2008), Forcing mechanism of the seasonally asymmetric Quasi-Biennial Oscillation secondary circulation in ERA-40 and MAECHAM5, *Journal of Geophysical Research: Atmospheres*, *113*(D16), doi:10.1029/2007JD009288.

Piani, C., D. Durran, M. Alexander, and J. Holton (2000), A numerical study of three-dimensional gravity waves triggered by deep tropical convection and their role in the dynamics of the QBO, *Journal of the Atmospheric Sciences*, *57*(22), 3689–3702.

Plougonven, R., H. Teitelbaum, and V. Zeitlin (2003), Inertia gravity wave generation by the tropospheric midlatitude jet as given by the Fronts and Atlantic Storm-Track Experiment radio soundings, *Journal of Geophysical Research (Atmospheres)*, *108*, 4686, doi:10.1029/2003JD003535.

Plumb, A. R., and R. C. Bell (1982), A model of the quasi-biennial oscillation on an equatorial beta-plane, *Quart. J. Roy. Meteor. Soc.*, *108*, 335–352, doi: 10.1002/qj.49710845604.

Plumb, R. A. (1977), The Interaction of Two Internal Waves with the Mean Flow: Implications for the Theory of the Quasi-Biennial Oscillation., *Journal of Atmospheric Sciences*, *34*, 1847–1858, doi:10.1175/1520-0469(1977)034<1847:TIOTIW>2.0.CO;2.

Polvani, L. M., and P. J. Kushner (2002), Tropospheric response to stratospheric perturbations in a relatively simple general circulation model, *Geophys. Res. Let.*, *29*(7), 070,000–1.

Reed, K. A., and C. Jablonowski (2012), Idealized tropical cyclone simulations of intermediate complexity: A test case for AGCMs, *J. Adv. Model. Earth Syst.*, *4*, M04,001, doi:10.1029/2011MS000099.

Reed, R. J., W. J. Campbell, L. A. Rasmussen, and D. G. Rogers (1961), Evidence of a downward-propagating, annual wind reversal in the equatorial stratosphere, *Journal of Geophysical Research*, *66*(3), 813–818.

Richter, J. H., F. Sassi, and R. R. Garcia (2010), Toward a physically based gravity wave source parameterization in a general circulation model, *Journal of the Atmospheric Sciences*, *67*(1), 136–156.

Richter, J. H., A. Solomon, and J. Bacmeister (2014a), On the simulation of the Quasi-Biennial Oscillation in the Community Atmosphere Model, version 5, *J. Geophys. Res.*, *119*, 3045–3062.

Richter, J. H., A. Solomon, and J. Bacmeister (2014b), Effects of vertical resolution and non-orographic gravity wave drag on the simulated climate in the Community Atmosphere Model, version 5, *Journal of Advances in Modeling Earth Systems*, *06*, 27 pp., doi:10.1002/2013MS000303.

Rosenlof, K. H. (1995), Seasonal cycle of the residual mean meridional circulation in the stratosphere, *Journal of Geophysical Research*, *100*, 5173–5191, doi: 10.1029/94JD03122.

Scaife, A. A., N. Butchart, C. D. Warner, D. Stainforth, W. A. Norton, and J. Austin (2000), Realistic Quasi-Biennial Oscillations in a Simulation of the Global Climate, *Geophys. Res. Let.*, *27*(21), 3481–3484.

Scaife, A. A., N. Butchart, C. D. Warner, and R. Swinbank (2002), Impact of a Spectral Gravity Wave Parameterization on the Stratosphere in the Met Office Unified Model, *J. Atmos. Sci.*, *59*, 1473–1489.

Schirber, S., E. Manzini, and M. J. Alexander (2014), A convection-based gravity wave parameterization in a general circulation model: Implementation and improvements on the QBO, *Journal of Advances in Modeling Earth Systems*, *6*, 264–279, doi: 10.1002/2013MS000286.

Schoeberl, M. R. (1978), Stratospheric warmings: Observations and theory, *Reviews of Geophysics*, *16*(4), 521–538.

Schoeberl, M. R., A. R. Douglass, R. S. Stolarski, S. Pawson, S. E. Strahan, and W. Read (2008), Comparison of lower stratospheric tropical mean vertical velocities, *J. Geophys. Res. (Atmospheres)*, *113*(D12), D24109, doi: 10.1029/2008JD010221.

Scinocca, J. F., N. A. McFarlane, M. Lazare, J. Li, and D. Plummer (2008), Technical Note: The CCCma third generation AGCM and its extension into the middle atmosphere, *Atmospheric Chemistry & Physics*, *8*, 7055–7074.

Seviour, W. J. M., N. Butchart, and S. C. Hardiman (2012), The Brewer-Dobson circulation inferred from ERA-Interim, *Quart. J. Roy. Meteorol. Soc.*, *138*, 878–888, doi:10.1002/qj.966.

Shiotani, M., K. Kuroi, and I. Hirota (1990), Eastward travelling waves in the southern hemisphere stratosphere during the spring of 1983, *Quarterly Journal of the Royal Meteorological Society*, *116*(494), 913–927, doi:10.1002/qj.49711649406.

Shuckburgh, E., W. Norton, A. Iwi, and P. Haynes (2001), Influence of the quasi-biennial oscillation on isentropic transport and mixing in the tropics and subtropics, *jgr*, *106*, 14,327, doi:10.1029/2000JD900664.

Simmons, A. J., and R. Strüfing (1983), Numerical forecasts of stratospheric warming events using a model with a hybrid vertical coordinate, *Quarterly Journal of the Royal Meteorological Society*, *109*(459), 81–111, doi:10.1002/qj.49710945905.

Straub, K. H., and G. N. Kiladis (2003), Extratropical Forcing of Convectively Coupled Kelvin Waves during Austral Winter, *J. Atmos. Sci.*, *60*, 526–543, doi: 10.1175/1520-0469(2003)060<0526:EFOCCK>2.0.CO;2.

Sun, L., W. A. Robinson, and G. Chen (2011), The role of planetary waves in the downward influence of stratospheric final warming events, *Journal of the Atmospheric Sciences*, *68*(12), 2826–2843.

Sun, L., W. A. Robinson, and G. Chen (2012), The Predictability of Stratospheric Warming Events: More from the Troposphere or the Stratosphere?, *Journal of Atmospheric Sciences*, *69*, 768–783, doi:10.1175/JAS-D-11-0144.1.

Taguchi, M., and D. L. Hartmann (2006), Increased occurrence of stratospheric sudden warmings during el nino as simulated by waccm, *Journal of climate*, *19*(3), 324–332.

Takahashi, M. (1996), Simulation of the stratospheric quasi-biennial oscillation using a general circulation model, *Geophys. Res. Let.*, *23*(6), 661–664.

Takahashi, M. (1999), Simulation of the quasi-biennial oscillation in a general circulation model, *Geophys. Res. Let.*, *26*(9), 1307–1310.

Takahashi, M., and B. A. Boville (1992), A Three-Dimensional Simulation of the Equatorial Quasi-biennial Oscillation., *Journal of Atmospheric Sciences*, *49*, 1020–1035, doi:10.1175/1520-0469(1992)049<1020:ATDSOT>2.0.CO;2.

Taylor, M. A., and A. Fournier (2010), A compatible and conservative spectral element method on unstructured grids, *J. Comput. Phys.*, *229*, 5879–5895.

Thompson, D. W., and S. Solomon (2002), Interpretation of recent southern hemisphere climate change, *Science*, *296*(5569), 895–899.

Thompson, D. W., M. P. Baldwin, and J. M. Wallace (2002), Stratospheric connection to northern hemisphere wintertime weather: Implications for prediction, *Journal of Climate*, *15*(12), 1421–1428.

Tindall, J. C., J. Thuburn, and E. J. Highwood (2006), Equatorial waves in the lower stratosphere. I: A novel detection method, *Quart. J. Roy. Meteor. Soc.*, *132*, 177–194.

Vial, J., T. J. Osborn, and F. Lott (2013), Sudden stratospheric warmings and tropospheric blockings in a multi-century simulation of the IPSL-CM5A coupled climate model, *Climate Dynamics*, *40*, 2401–2414.

Wang, L., and M. J. Alexander (2009), Gravity wave activity during stratospheric sudden warmings in the 2007-2008 Northern Hemisphere winter, *Journal of Geophysical Research (Atmospheres)*, *114*, D18108, doi:10.1029/2009JD011867.

Watson, P. A., and L. J. Gray (2014), How does the Quasi-Biennial Oscillation affect the stratospheric polar vortex?, *Journal of the Atmospheric Sciences*, *71*(1), 391–409.

Wei, K., W. Chen, and R. Huang (2007), Association of tropical Pacific sea surface temperatures with the stratospheric Holton-Tan Oscillation in the Northern Hemisphere winter, *GRL*, *34*, L16814, doi:10.1029/2007GL030478.

Wheeler, M., and G. N. Kiladis (1999), Convectively coupled equatorial waves: Analysis of clouds and temperature in the wavenumber-frequency domain, *J. Atmos. Sci.*, *56*, 374–399.

Whitehead, J. P., C. Jablonowski, R. B. Rood, and P. H. Lauritzen (2011), A Stability Analysis of Divergence Damping on a Latitude-Longitude Grid, *Monthly Weather Review*, *139*, 2976–2993, doi:10.1175/2011MWR3607.1.

Williamson, D. L. (2007), The evolution of dynamical cores for global atmospheric models, *J. Meteorol. Soc. Japan*, *85B*, 241–269.

Williamson, D. L., and J. Olson (1994), Climate simulations with a semi-Lagrangian version of the NCAR Community Climate Model, *Mon. Wea. Rev.*, *122*(7), 1594–1610.

Williamson, D. L., J. G. Olson, and B. A. Boville (1998), A comparison of semi-Lagrangian and Eulerian tropical climate simulations, *Mon. Wea. Rev.*, *126*, 1001–1012.

Woollings, T., A. Charlton-Perez, S. Ineson, A. G. Marshall, and G. Masato (2010), Associations between stratospheric variability and tropospheric blocking, *J. Geophys. Res. (Atmospheres)*, *115*, D06,108.

Xue, X., H. Liu, and Dou,X. (2012), Parameterization of the Inertial Gravity Waves and Generation of the Quasi-Biennial Oscillation, *Journal of Geophysical Research (Atmospheres)*, doi:10.1029/2011JD016778.

Yang, G.-Y., B. Hoskins, and J. Slingo (2007), Convectively Coupled Equatorial Waves. Part III: Synthesis Structures and Their Forcing and Evolution, *Journal of Atmospheric Sciences*, *64*, 3438, doi:10.1175/JAS4019.1.

Yang, G. Y., B. J. Hoskins, and J. M. Slingo (2011), Equatorial waves in opposite qbo phases, *Journal of the Atmospheric Sciences*, *68*(4), 839–862.

Yang, G.-Y., B. Hoskins, and L. Gray (2012), The Influence of the QBO on the Propagation of Equatorial Waves into the Stratosphere, *J. Atmos. Sci.*, *69*, 2959–2982, doi:10.1175/JAS-D-11-0342.1.

Yao, W., and C. Jablonowski (2013), Spontaneous QBO-like oscillations in an atmospheric model dynamical core, *Geophysical Research Letters*, *40*, 3772–3776, doi:10.1002/grl.50723.

Yao, W., and C. Jablonowski (2014), Idealized simulations of the Quasi-Biennial Oscillation in an ensemble of dry GCM dynamical cores, *J. Atmos. Sci.*, *in review*.

Yuan, W., M. A. Geller, and P. T. Love (2013), Enso influence on qbo modulations of the tropical tropopause, *Quarterly Journal of the Royal Meteorological Society*.

Zhang, G. J., and N. A. McFarlane (1995), Sensitivity of climate simulations to the parameterization of cumulus convection in the canadian climate centre general circulation model, *Atmosphere-Ocean*, *33*(3), 407–446.